NTNU
Norwegian University of
Science and Technology

Proximity effect in ballistic superconductor-ferromagnet structures with spin-orbit coupling

Haakon Thømt Simensen

Master of Science in Physics and Mathematics
Submission date: June 2017
Supervisor: Jacob Rune Wüsthoff Linder, IFY

Norwegian University of Science and Technology
Department of Physics

Abstract

The Bogoliubov-de Gennes equations have been solved numerically for a number of two-dimensional ballistic proximity structures comprised of superconductors, normal metals and ferromagnets, with both interfacial and in-plane spin-orbit coupling. These results have been compared to results obtained for similar structures in the absence of spin-orbit coupling. The results show that spin-orbit coupling in general enhances superconductivity in ferromagnet-superconductor-structures, and causes the critical temperature, as well as singlet and triplet amplitudes, to become dependent upon the orientation of the magnetic field. The protective effect of spin-orbit coupling on the superconducting state grows stronger the closer the magnetic field comes to being perpendicular to the effective fields induced by spin-orbit coupling. Both interfacial and in-plane spin-orbit coupling have these effects in common, but the effect is most prominent for the in-plane spin-orbit coupling. The observed effects can be explained by projecting the Cooper pair states onto the eigenbasis of the system, which reveals that the singlet state adapts a long-ranged pseudotriplet component in the presence of spin-orbit coupling. Spin-orbit coupling thus serves as an alternative to inhomogeneously magnetized structures, as it enables control of the critical temperature, as well as both singlet and triplet amplitudes, by adjusting macroscopic parameters. Additionally, the protective effect spin-orbit coupling introduces on the superconducting state allows for such structures to be made smaller than in its absence.

Sammendrag

Bogoliubov-de Gennes-likningene har blitt løst numerisk for todimensjonelle ballistiske systemer satt sammen av superledere, normalmetaller og ferromagneter, med spinn-bane-kobling både i grensesjiktet og i planet. Disse resultatene har blitt sammenliknet med resultater av liknende systemer uten spinn-bane-kobling. Resultatene viser at spinn-bane-kobling generelt sett styrker superledning i ferromagnet-superleder-systemer, og gjør både kritisk temperatur, singlett- og triplettamplituder avhengige av orienteringen til det magnetiske feltet. Den beskyttende effekten spinn-bane-kobling påfører den superledende tilstanden øker jo nærmere det magnetiske feltet kommer å være normalt på de magnetiske feltene indusert av spinn-bane-kobling. Begge typer spinn-bane-kobling har dette til felles, men effekten er tydeligst for spinn-bane-kobling i planet. Den observerte effekten kan forklares ved å projisere Cooper-parene på egenbasisen til systemet, hvilket viser at singlettilstanden får en komponent av en langtrekkende pseudotriplett når spinn-bane-kobling er tilstede. Spinn-bane-kobling kan derfor fungere som et alternativ til inhomogent magnetiserte systemer, da det åpner opp for kontroll av kritisk temperatur, samt singlett- og triplettamplituder, ved å justere makroskopiske parametre. Den beskyttende effekten spinn-bane-kobling har på den superledende tilstanden gjør i tillegg at slike systemer kan lages mindre enn i fraværet av spinn-bane-kobling.

Preface

This document was submitted as a 30 ECTS-credits master's thesis in theoretical condensed matter physics at the Norwegian University of Technology and Science (NTNU) in June 2017. It has more or less been a continuation of a 15 ECTS-credits specialization project from the fall semester of 2016. Both the specialization project and the master's work have been under supervision of Prof. Jacob Linder. During the specialization project, a numerical method for solving the Bogoliubov-de Gennes equations for superconductor-ferromagnet-structures was developed, which was used to reproduce results from a selection of published papers. During the work with the master's thesis, spin-orbit coupling was added to the numerical solver. The code was also further developed in order to be able to calculate new physical quantities. This work included many hours of programming, debugging and testing, eventually resulting in a framework in which all results in this thesis have been produced. Parallel to this work, a main focus has been to try out different system configurations, and to see what effects might be obtained by adjusting the different macroscopic parameters of the system. Eventually, significant effort has been put into developing an analytical explanation for the results.

The work has been challenging, as there exist few references to which the results may directly be compared. I am yet very grateful to my supervisor, Jacob Linder, who let me commit to this project. The originality of the project is just what has made it interesting, and I have had the feeling of being close to the frontier in this field of research. I also want to thank him for the many long-lasting discussion in his office, giving me time to present and discuss ideas for how the results could be explained.

All the results presented in this thesis are products of extensive numerical calculations. Due to the considerable requirements for computational power, both when it comes to RAM and CPU, the programs have been executed on *Vilje*, the high-performance computer (HPC) at NTNU.

Haakon Thømt Simensen
Trondheim, Norway
June 2017

Contents

1 Introduction

1.1 Background and motivation

Superconductivity is one of the largest research fields in condensed matter physics, the latter being the largest research branch in physics. Its most well known property is giving zero electrical resistance, thus enabling electrons to move frictionlessly inside a superconductor. An obvious application is therefore using it simply as an electrical conductor, resulting in no energy dissipation. This would lead to less power consumption and less heat production, which are both attractive properties for all types of wires and electrical circuits. Taking it a step further, the properties of superconductors make them potentially useful as building blocks for logic circuits in spintronics.[1] Hence, we need methods of controlling superconductivity with macroscopic parameters, which is the main motivation behind this thesis.

When the superconducting state arises, the conduction electrons condense into a condensate of Cooper pairs. These Cooper pairs are pairs of electrons, which in the simplest *s*-wave superconductors consist of electrons of opposite spin and momenta, $\psi_s \sim |\mathbf{k},\uparrow\rangle|-\mathbf{k},\downarrow\rangle - |\mathbf{k},\downarrow\rangle|-\mathbf{k},\uparrow\rangle$, which are called singlet pairs. Under normal circumstances, electrons repel each other due to Coulomb repulsion, and will thus not pair up. In superconductors however, forming Cooper pairs may under certain circumstances be energetically favoured, and this is indeed what makes superconductors superconducting. When Cooper pairs are formed, an energy gap in the dispersion relation of the single-particle states appears. This implies that the electrons in the Cooper pair cannot scatter into other nearby single-particle states, and hence they move frictionlessly through the superconductor. However, a superconductor is not superconducting under all circumstances. Firstly, if the thermal energy becomes sufficiently high, the Cooper pairs will be ripped apart, and superconductivity breaks down. Secondly, when the superconductor is subject to a magnetic field, surface currents appears. When the energy associated with these currents exceeds the energy the electrons gain by paring into Cooper pairs, Cooper pairs will no longer be the preferred stable state. Thus, for sufficiently strong magnetic fields, superconductivity breaks down.

As a matter of fact, one of the very defining properties of singlet *s*-wave superconductivity is its incompatibility with ferromagnetism. Interestingly though, this antagonistic relation is also what makes for some of the most interesting properties from a technological point of view. Cooper pairs consisting of electrons with oppositely aligned spins will gain different momenta when subject to a magnetic field. This causes a relative phase between $|\mathbf{k},\uparrow\rangle|-\mathbf{k},\downarrow\rangle$ and $|\mathbf{k},\downarrow\rangle|-\mathbf{k},\uparrow\rangle$ as they gain a non-zero center-of-mass momentum,[2] causing leakage of singlet pairs, which effectively breaks down superconductivity. The leakage of Cooper pairs gives rise to a new type of Cooper pairs, namely triplet pairs. A single, homogeneous magnetic field will

produce triplet pairs of the type $\psi_t \sim |\mathbf{k},\uparrow\rangle|-\mathbf{k},\downarrow\rangle + |\mathbf{k},\downarrow\rangle|-\mathbf{k},\uparrow\rangle$. If we introduce a magnetic inhomogeneity, such as a domain walls,[3,4] or a second magnetic field pointing in another direction,[5,6] these triplets will be "rotated" into another kind of triplet pairs,[7,8] namely $\psi_t^{\pm} \sim |\mathbf{k},\uparrow\rangle|-\mathbf{k},\uparrow\rangle \pm |\mathbf{k},\downarrow\rangle|-\mathbf{k},\downarrow\rangle$. These different types of triplets are all channels which cause leakage of singlets from the superconductor. If this leakage is sufficiently large, superconductivity breaks down. By controlling the magnetic field configuration, we may control these channels, and may therefore control superconductivity.

An interesting property about the triplets is that they have a non-zero total spin, that is a dimensionless spin of $|\mathbf{S}| = 1$. As spin is of binary nature, superconductors are therefore promising building blocks for logic circuits. Instead of transporting information by using voltage, as in electronics, we may use the electron spin as information carrier, giving rise to the field of spintronics.[9] However, as implied by quantum mechanics, the spin-projection of a spin-1 state may evaluate to either 0 or ± 1. Both the singlet state and the triplet state produced by a homogeneously magnetized, z-aligned ferromagnet always carry a spin $s_z = 0$, and thus cannot single-handedly transport binary information. The spin-polarized triplets however, containing terms as $|\uparrow\rangle|\uparrow\rangle$ and $|\downarrow\rangle|\downarrow\rangle$, have a non-zero s_z, and may thus be used to carry information. Another interesting property about triplets is that they may be long-ranged inside magnetic fields. The singlet state and the first triplet, both consisting of terms $\sim |\uparrow\rangle|\downarrow\rangle$, will be torn apart by magnetic fields parallel to the axis of quantization because they both acquire a non-zero center-of-mass momentum. These pairs are thus ripped apart by the magnetic field, and are due to this called "short-ranged" Cooper pairs. The triplets $\psi_t^{\pm}$ will however have no center-of-mass momentum inside a magnetic field parallel to the axis of quantization, and they are thus called "long-ranged" inside this magnetic field. The long-ranged triplets reach much further into ferromagnets than their short-ranged relatives,[10–13] which is potentially useful for technological purposes.

Instead of inhomogeneously magnetized ferromagnetic regions, the inclusion of spin-orbit coupling (SOC) in ferromagnet-superconductor-structures may serve as an alternative way of controlling critical temperature and triplet production.[14] Additionally, it has earlier been proposed that SOC combined with an s-wave superconductor mimics p-wave topological superconductivity,[15–17] which may further realize Majorana fermions.[18–20] An experiment performed in 2014 provided strong evidence for just this effect.[21] Exploring how SOC interacts with superconductivity is therefore of interest from a technological as well as a phenomenological point of view.

1.2 Scope and structure

The search for system configurations in which macroscopic parameters may be used to control both the singlet and triplet amplitudes are of particular interest in this field of research. A vast amount of possible configurations using ferromagnets and superconductors are already explored in previous literature. The scope of this thesis is therefore to instead study how SOC may be used together with magnetic fields in order to control superconducting properties of a system. As will be evident later in this thesis, SOC shows promising properties for this purpose. Both adjusting the strength of SOC

and rotating a magnetic field relative to the SOC-region affect the critical temperature, and can thus be used as control parameters for superconductivity.

In Chapter 2, we will analyze the effect of SOC from a mathematical point of view, as well as go through some theoretical groundwork necessary for developing the numerical methods used in later chapters. These numerical methods will be explained in detail in Chapter 3. In Chapter 4, we will use these methods to calculate pair amplitudes, local density of states and critical temperatures for systems built up by superconductors, normal metals and ferromagnets. These systems have been explored earlier, and this chapter therefore contains few new results. The main motivation behind including this chapter is to make the thesis complete, as well as to make certain that the method is capable of reproducing well known results. Additionally, most calculations in this thesis are performed in two dimensions, while these systems earlier have mostly been explored in three dimensions. Chapter 4 therefore serves as reference for the results obtained in Chapter 5, where SOC is included. The main new results in this thesis are presented in Chapter 5. We will explore SOC both in the interface between two materials, as well as in-plane SOC inside a ferromagnetic region. All results in this thesis are obtained in the ballistic limit. This is the limit where the system under consideration is much shorter than the expected mean-free-path of the electrons, enabling us to neglect any scattering events. All results have been calculated numerically by using a full quantum mechanical approach.

2 Fundamental concepts

2.1 Superconductivity

2.1.1 The BCS theory

The BCS theory[22] was the first full quantum theory which managed to explain superconductivity. It is still used as the standard theory, and is based upon the following mean-field Hamiltonian:[23]

$$H = \sum_{\sigma} \int d\mathbf{r} \hat{\psi}^{\dagger}(\mathbf{r},\sigma) H_e \hat{\psi}(\mathbf{r},\sigma) + \int d\mathbf{r} \Big\{ \Delta^{*}(\mathbf{r}) \hat{\psi}(\mathbf{r},\downarrow)\hat{\psi}(\mathbf{r},\uparrow) + \Delta(\mathbf{r})\hat{\psi}^{\dagger}(\mathbf{r},\uparrow)\hat{\psi}^{\dagger}(\mathbf{r},\downarrow) \Big\}, \tag{2.1}$$

where $\hat{\psi}(\mathbf{r},\sigma)$ is an electron field operator, and where $\mathbf{r}$ is position and σ denotes spin. This Hamiltonian includes, in addition to the kinetic term, H_e, an attraction term between electrons with opposite spin and anti-parallel momentum. The magnitude of the attraction is determined by $\Delta(\mathbf{r})$, which is called the superconducting gap parameter. This attraction is the origin of superconductivity, and for the singlet *s*-wave superconductivity, it is defined as

$$\Delta(\mathbf{r}) = V \left\langle \hat{\psi}(\mathbf{r},\uparrow)\hat{\psi}(\mathbf{r},\downarrow) \right\rangle, \tag{2.2}$$

where V is a coupling strength, being non-zero only inside a superconductor for electrons within a certain energy interval.[24] We will come back to the superconducting gap parameter in section 2.1.3, where we will also define *s*-wave superconductivity properly.

2.1.2 Diagonalizing the BCS Hamiltonian

The BCS Hamiltonian given in Eq. (2.1) is not diagonal in the operators, and one cannot immediately read out the eigenstates. If we manage to diagonalize H however, we can read off both the eigenstates and the energies of the system. We will do so by a purely mathematical method using only linear algebra, and eventually generalize this into a Bogoliubov transformation.

We start out by expressing the Hamiltonian with momentum operators instead of fields operators, as we expect the energy eigenstates to have well defined momentum $\mathbf{p} = \hbar\mathbf{k}$. We transform Eq. (2.1) into

$$H = \sum_{\mathbf{k},\sigma} \epsilon_{\mathbf{k}} c^{\dagger}_{\mathbf{k},\sigma} c_{\mathbf{k},\sigma} + \sum_{\mathbf{k}} \left\{ \Delta^{*}_{\mathbf{k}} c_{-\mathbf{k},\downarrow} c_{\mathbf{k},\uparrow} + \Delta_{\mathbf{k}} c^{\dagger}_{\mathbf{k},\uparrow} c^{\dagger}_{-\mathbf{k},\downarrow} \right\}. \tag{2.3}$$

where $\epsilon_{\mathbf{k}} = \frac{\hbar^2\mathbf{k}^2}{2m_e}$ is the dispersion relation of free electrons, $\Delta_{\mathbf{k}}$ is the coupling strength between electrons with wave vectors $\mathbf{k}$ and $-\mathbf{k}$, and $c_{\mathbf{k},\sigma}$ and $c^\dagger_{\mathbf{k},\sigma}$ are the annihilation and creation operators of an electron in the state $(\mathbf{k}, \sigma)$, respectively. In order to make this Hamiltonian diagonal in the operators, we clearly need to do an operator transformation. With matrix notation, the Hamiltonian in Eq. (2.3) may be rewritten into matrix form,

$$H = \frac{1}{2}\sum_{\mathbf{k}} \mathbf{c}^\dagger_{\mathbf{k}} \mathbf{T}_{\mathbf{k}} \mathbf{c}_{\mathbf{k}}, \tag{2.4}$$

where $\mathbf{T}_{\mathbf{k}}$ and $\mathbf{c}_{\mathbf{k}}$ are defined as

$$\mathbf{c}_{\mathbf{k}} = \begin{pmatrix} c_{\mathbf{k},\uparrow} \\ c_{\mathbf{k},\downarrow} \\ c^\dagger_{-\mathbf{k},\uparrow} \\ c^\dagger_{-\mathbf{k},\downarrow} \end{pmatrix}, \quad \mathbf{T}_{\mathbf{k}} = \begin{pmatrix} \epsilon_{\mathbf{k}} & 0 & 0 & \Delta_{\mathbf{k}} \\ 0 & \epsilon_{\mathbf{k}} & -\Delta_{\mathbf{k}} & 0 \\ 0 & -\Delta^*_{\mathbf{k}} & -\epsilon_{\mathbf{k}} & 0 \\ \Delta^*_{\mathbf{k}} & 0 & 0 & -\epsilon_{\mathbf{k}} \end{pmatrix}. \tag{2.5}$$

For notational simplicity, the $\mathbf{k}$-index on the matrices is being suppressed from now on. The standard diagonalization procedure from linear algebra involves defining a unitary matrix $\mathbf{P}$ which diagonalizes $\mathbf{T}$,

$$\mathbf{P}\mathbf{T}\mathbf{P}^\dagger = \mathbf{D}, \tag{2.6}$$

where $\mathbf{D}$ is a diagonal matrix. The elements of $\mathbf{D}$ are the eigenvalues of $\mathbf{T}$, and the columns of the diagonalization matrix $\mathbf{P}$ are the eigenvectors of $\mathbf{T}$. If we utilize the unitarity of $\mathbf{P}$, that is $\mathbf{P}\mathbf{P}^\dagger = \mathbb{I}$, we may write

$$H = \frac{1}{2}\sum_{\mathbf{k}} \mathbf{c}^\dagger_{\mathbf{k}} (\mathbf{P}^\dagger\mathbf{P})\mathbf{T}(\mathbf{P}^\dagger\mathbf{P})\mathbf{c}_{\mathbf{k}} = \frac{1}{2}\sum_{\mathbf{k}} \gamma^\dagger_{\mathbf{k}} \mathbf{D} \gamma_{\mathbf{k}}. \tag{2.7}$$

In the second equality we implicitly defined $\gamma_{\mathbf{k}} = \mathbf{P}\mathbf{c}_{\mathbf{k}}$ for a new set of operators $\gamma_{\mathbf{k}} = [\gamma_{\mathbf{k},\uparrow}, \gamma_{\mathbf{k},\downarrow}, \gamma^\dagger_{\mathbf{k},\uparrow}, \gamma^\dagger_{\mathbf{k},\downarrow}]^{\mathrm{T}}$. These new operators are thus linear transformations of the old operators. We may also refer to them as rotated operators, as one can picture the new states as rotated versions of the old ones. Equivalently, we have to perform the operator transformation $\mathbf{c}_{\mathbf{k}} = \mathbf{P}^\dagger\gamma_{\mathbf{k}}$ when rotating the new operators into the old ones. In order to diagonalize H, we now need to find the eigenvalues of $\mathbf{T}$. This is a straightforward procedure, resulting in

$$E^{\pm}_{\mathbf{k}} = \pm\sqrt{\epsilon^2_{\mathbf{k}} + |\Delta_{\mathbf{k}}|^2} \equiv \pm E_{\mathbf{k}}, \tag{2.8}$$

which gives the following operator transformation matrix:

$$\mathbf{P} = \frac{A_{\mathbf{k}}}{2}\begin{pmatrix} E_{\mathbf{k}} + \epsilon_{\mathbf{k}} & 0 & E_{\mathbf{k}} - \epsilon_{\mathbf{k}} & 0 \\ 0 & -E_{\mathbf{k}} + \epsilon_{\mathbf{k}} & 0 & -E_{\mathbf{k}} - \epsilon_{\mathbf{k}} \\ 0 & \Delta^*_{\mathbf{k}} & 0 & \Delta^*_{\mathbf{k}} \\ \Delta^*_{\mathbf{k}} & 0 & \Delta^*_{\mathbf{k}} & 0 \end{pmatrix}. \tag{2.9}$$

This matrix is however not unique, as the eigenvectors are only determined up to a normalization constant $A_{\mathbf{k}}$. A natural choice of $A_{\mathbf{k}}$ is such that the transformation is unitary. If we insert (2.8) and (2.9) into the Hamiltonian, we get

$$H = \sum_{\mathbf{k}} \left(E_{\mathbf{k}} \gamma^{\dagger}_{\mathbf{k},\uparrow} \gamma_{\mathbf{k},\uparrow} + E_{\mathbf{k}} \gamma^{\dagger}_{\mathbf{k},\downarrow} \gamma_{\mathbf{k},\downarrow} \right). \tag{2.10}$$

which reveals the eigenstates as the states created and annihilated by the $\gamma_{\mathbf{k},\sigma}$-operators. We refer to these states as quasiparticles, and we observe that their dispersion relation is $E_{\mathbf{k}}$. The quasiparticles can be regarded as rotated electron-/hole-states. That is, the new states span the same Hilbert space of states as the old states, as linear combinations of the old ones. To check that we have a consistent result, we observe what happens when $\Delta_{\mathbf{k}} = 0$, that is when superconductivity is absent. The dispersion relation becomes simply $E_{\mathbf{k}} = \epsilon_{\mathbf{k}}$, equal to the one of electrons. Furthermore, $\mathbf{P}$ simplifies such that $c_{\mathbf{k},\sigma} = A_{\mathbf{k}} E_{\mathbf{k}} \gamma_{\mathbf{k},\sigma}$. In other words, with a proper choice of $A_{\mathbf{k}}$, the eigenstates simplify to electrons. When superconductivity is absent, we are thus back to where we started, which is a consistent result.

This was an example of a very specific operator transformation. It works adequately, but the procedure is a bit time consuming. Especially working out the $\mathbf{P}$-matrix demands a fair amount of calculations. A natural generalization of this transformation is a so-called Bogoliubov transformation, where we start out by expressing the old operators as a linear combinations of the new ones[25,26]

$$\begin{aligned} c_{\mathbf{k},\uparrow} &= \sum_{\sigma'} \left[u_{\mathbf{k},\uparrow,\sigma'} \gamma_{\mathbf{k},\sigma'} - v^{*}_{\mathbf{k},\uparrow,\sigma'} \gamma^{\dagger}_{\mathbf{k},\sigma'} \right], \\ c_{-\mathbf{k},\downarrow} &= \sum_{\sigma'} \left[u_{\mathbf{k},\downarrow,\sigma'} \gamma_{\mathbf{k},\sigma'} + v^{*}_{\mathbf{k},\downarrow,\sigma'} \gamma^{\dagger}_{\mathbf{k},\sigma'} \right]. \end{aligned} \tag{2.11}$$

We have written the old operators in terms of the amplitudes $u_{\mathbf{k},\sigma,\sigma'}$ and $v_{\mathbf{k},\sigma,\sigma'}$, which are to be interpreted as wave functions in momentum space. Note the minus sign used in the definition of $c_{\mathbf{k},\uparrow}$, which is introduced only due to convention. These amplitudes must be chosen such that the Hamiltonian becomes diagonal in the new operators, that is on the form

$$H = \sum_{\mathbf{k},\sigma} E_{\mathbf{k},\sigma} \gamma^{\dagger}_{\mathbf{k},\sigma} \gamma_{\mathbf{k},\sigma}. \tag{2.12}$$

In addition to requiring all non-diagonal terms in H to disappear, we want the transformation to be unitary. We thus require $\sum_{\sigma'} \left(\left| u_{\mathbf{k},\sigma,\sigma'} \right|^2 + \left| v_{\mathbf{k},\sigma,\sigma'} \right|^2 \right) = 1$. These constraints combined determine the set of $u_{\mathbf{k},\sigma,\sigma'}$'s and $v_{\mathbf{k},\sigma,\sigma'}$'s, and define both the operator transformation $\gamma_{\mathbf{k}} = \mathbf{P} \mathbf{c}_{\mathbf{k}}$ as well as the new (spin-dependent) dispersion relation $E_{\mathbf{k},\sigma}$. If we use this formalism on the system defined by the Hamiltonian in Eq. (2.3), we get the exact same result as was obtained by the linear algebra approach in Eqs. (2.8) and (2.9). This method is however more general, and is more suited for a self-consistent numerical approach, which will be addressed later in this thesis.

Eventually, we want to go back to our field operator formalism, which enables us to work in the position space. Following the textbook definition of field operators, this is a straightforward procedure, resulting in[27]

$$\hat{\psi}(\mathbf{r},\uparrow) = \sum_{\mathbf{k},\sigma}\Big[u_{\mathbf{k},\uparrow,\sigma}(\mathbf{r})\gamma_{\mathbf{k},\sigma} - v^{*}_{\mathbf{k},\uparrow,\sigma}(\mathbf{r})\gamma^{\dagger}_{\mathbf{k},\sigma}\Big],$$
$$\hat{\psi}(\mathbf{r},\downarrow) = \sum_{\mathbf{k},\sigma}\Big[u_{\mathbf{k},\downarrow,\sigma}(\mathbf{r})\gamma_{\mathbf{k},\sigma} + v^{*}_{\mathbf{k},\downarrow,\sigma}(\mathbf{r})\gamma^{\dagger}_{\mathbf{k},\sigma}\Big]. \tag{2.13}$$

The amplitudes $u_{\mathbf{k},\sigma',\sigma}(\mathbf{r})$ and $u_{\mathbf{k},\sigma',\sigma}(\mathbf{r})$ are to be considered as real space wave functions of electrons or holes in the state $(\mathbf{k},\sigma',\sigma)$. One may check that a proper choice of these amplitudes indeed diagonalizes the real space Hamiltonian in Eq. (2.1).

2.1.3 The superconducting gap

The singlet superconducting gap parameter for *s*-wave superconductivity was defined in section 2.1.1. To include all forms of superconductivity, we have to be a bit more general. We include the time-coordinate in the field operators, and define the superconducting gap parameter more generally as

$$\Delta_{\sigma\sigma'}(\mathbf{r},t;\mathbf{r}',t') = V_{\sigma\sigma'}\left\langle\hat{\psi}(\mathbf{r},t,\sigma)\hat{\psi}(\mathbf{r}',t',\sigma')\right\rangle. \tag{2.14}$$

The different forms of superconductivity are related to how electrons with different quantum numbers form Cooper pairs. The only constraint on this pairing is that the Cooper pair state must obey the Pauli principle, thus it must be overall antisymmetric. We relate three quantum numbers to every electron, namely spin, position and time. Fully equivalently, we may use momentum and frequency instead of position and time, which are merely Fourier transforms of the corresponding quantum numbers, and thus span the same subspace of the Hilbert space of states as their counterparts. An odd state requires either being odd in one and even in two quantum numbers, or being odd in all of the three quantum numbers. *s*-wave superconductivity is spherically symmetric, that is we may set $\mathbf{r} = \mathbf{r}'$, and must hence be antisymmetric in either relative time, $\tau = t - t'$, or in spin. Forms of superconductivity which is not a result of *s*-wave singlet pairing is referred to as *unconventional* superconductivity. An example of such is if the superconducting gap parameter is antisymmetric in momentum, and symmetric in time and spin, which is called *p*-wave superconductivity.

In this thesis we will focus on *s*-wave superconductivity, which is what is predicted by the BCS theory, and we therefore only use the coordinates $(\mathbf{r},\tau)$ from now on. Whenever we refer to singlets or triplets from now on, we implicitly refer to the *s*-wave versions of these. We observe that $\Delta_{\sigma\sigma'}(\mathbf{r},\tau)$ is proportional to an expectation value of two electron annihilation field operators. Its interpretation should be that if $\Delta_{\sigma\sigma'}(\mathbf{r},\tau) \neq 0$, there is both an attraction mechanism and a correlation between two electrons with spin σ and σ' at position $\mathbf{r}$ and with relative time τ. Two electrons which are correlated can be said to form a pair, and such electron pairs are the origin of superconductivity, commonly referred to as Cooper pairs.

The singlet superconducting gap can be written as

$$\Delta_{\mathrm{s}}(\mathbf{r}) = \frac{1}{2}\Big(\Delta_{\uparrow\downarrow}(\mathbf{r}) - \Delta_{\downarrow\uparrow}(\mathbf{r})\Big), \tag{2.15}$$

which simplifies to Eq. (2.2) if we use the anticommutation relations of fermionic operators. In the BCS theory, these Cooper pairs are the source of superconductivity. We can see this from the Hamiltonian in Eq. (2.1), as the only intrinsic pairing mechanism is between electrons of opposite spin, and at equal space and time coordinates. The singlet superconducting gap was written with an s-index in Eq. (2.15). From here on, when $\Delta(\mathbf{r})$ is given without any indices, as well is without the τ-coordinate, we implicitly refer to the singlet gap. The other possible s-wave channels are so-called odd-frequency Cooper pairs.[28] These require $\tau \neq 0$ to be finite due to the Pauli principle, and are called triplets, as they have a dimensionless spin of $|\mathbf{S}| = 1$. The odd-frequency ($s_z = 0$)-triplet gap is defined as

$$\Delta_{\text{of},1}(\mathbf{r}, \tau) = \frac{1}{2}\Big(\Delta_{\uparrow\downarrow}(\mathbf{r}, \tau) + \Delta_{\downarrow\uparrow}(\mathbf{r}, \tau)\Big), \tag{2.16}$$

while the corresponding spin polarized triplet gaps with ($s_z = \pm 1$) are given as

$$\Delta_{\text{of},2}(\mathbf{r}, \tau) = \frac{1}{2}\Big(\Delta_{\uparrow\uparrow}(\mathbf{r}, \tau) - \Delta_{\downarrow\downarrow}(\mathbf{r}, \tau)\Big), \tag{2.17}$$

$$\Delta_{\text{of},3}(\mathbf{r}, \tau) = \frac{1}{2}\Big(\Delta_{\uparrow\uparrow}(\mathbf{r}, \tau) + \Delta_{\downarrow\downarrow}(\mathbf{r}, \tau)\Big). \tag{2.18}$$

Note that none of these ($s_z = \pm 1$)-triplets are σ_z-eigenstates, which their name might suggest. However, the $\pm$ signifies that they are linear combinations of pairs with $s_z = 1$ and $s_z = -1$, and this convention will be used throughout the thesis. Odd-frequency superconductivity does not occur naturally in clean s-wave BCS superconductors. s-wave odd-frequency superconductivity is therefore also referred to as a kind of unconventional superconductivity, as it is not of singlet nature. Odd-frequency superconductivity is for instance believed to exist in Sr_2RuO_4.[29–31] Although a clean s-wave BCS superconductor does not form odd-frequency Cooper pairs, this does not exclude the possibility of these pairs ever being formed in a hybrid system. We therefore define the pair amplitude

$$f_{\sigma\sigma'}(\mathbf{r}, \tau) = \left\langle \hat{\psi}(\mathbf{r}, \tau, \sigma)\hat{\psi}(\mathbf{r}, 0, \sigma') \right\rangle, \tag{2.19}$$

which is equivalent to $\Delta_{\sigma\sigma'}/V_{\sigma\sigma'}$. The $f_{\sigma\sigma'}$-amplitudes capture the correlation between electrons with spin σ and σ', and are not constrained to zero if an explicit interaction is not present, that is if $V_{\sigma\sigma'}$ is zero. Of particular interest is the pair amplitude indicating normal singlet Cooper pairs, as well as the odd-frequency triplet pairs. We therefore define

$$f_0(\mathbf{r}) = \frac{1}{2}\Big(f_{\uparrow\downarrow}(\mathbf{r}) - f_{\downarrow\uparrow}(\mathbf{r})\Big), \tag{2.20}$$

which is the pair amplitude for singlet Cooper pairs. This pair amplitude is for instance useful when studying how far into metals and ferromagnets normal singlet Cooper pairs reach before being broken down. The superconducting gap parameter, $\Delta(\mathbf{r})$, would have been zero inside this region due to $V_{\uparrow\downarrow}$ being zero, and f_0 may thus bring information which is not contained in Δ. We furthermore define the triplet amplitudes,

$$f_1(\mathbf{r},\tau) = \frac{1}{2}\Big(f_{\uparrow\downarrow}(\mathbf{r},\tau) + f_{\downarrow\uparrow}(\mathbf{r},\tau)\Big), \tag{2.21}$$

$$f_2(\mathbf{r},\tau) = \frac{1}{2}\Big(f_{\uparrow\uparrow}(\mathbf{r},\tau) - f_{\downarrow\downarrow}(\mathbf{r},\tau)\Big), \tag{2.22}$$

$$f_3(\mathbf{r},\tau) = \frac{1}{2}\Big(f_{\uparrow\uparrow}(\mathbf{r},\tau) + f_{\downarrow\downarrow}(\mathbf{r},\tau)\Big), \tag{2.23}$$

where f_1 is the amplitude for ($s_z = 0$)-triplet Cooper pairs, while f_2 and f_3 are the amplitudes for ($s_z = \pm 1$)-triplet Cooper pairs. If any of these three odd-frequency triplet amplitudes are non-zero in a system in which the only intrinsic superconductivity is of singlet nature, it implies that some other effect has been participating in creating them. Both experiments and theoretical simulations have shown that different setups with magnetic fields create this effect,[32] and of special interest are inhomogeneous magnetic fields, which produce several of these triplet amplitudes.[33]

2.2 The Bogoliubov-de Gennes equations

The Bogoliubov-de Gennes (BdG) equations are matrix equations equivalent to the Schrödinger equation. Their matrix nature makes them well suited for finding the eigenstates and energy eigenvalues of a system. We will first derive them for the system described by the Hamiltonian in Eq. (2.1), and thereafter generalize them to systems which include magnetic fields and an electric potential.

The key to the derivation is to calculate the commutator

$$\Big[H, \hat{\psi}(\mathbf{r},\sigma)\Big] \tag{2.24}$$

in two different ways. If we then equate the two results, the resulting equations are the BdG equations. We use the anticommutation relations of fermionic operators to show that

$$\begin{aligned}
\left[\int d\mathbf{r}'\hat{\psi}^\dagger(\mathbf{r}',\sigma')\hat{\psi}(\mathbf{r}',\sigma'), \hat{\psi}^\dagger(\mathbf{r},\sigma)\right] &= \hat{\psi}^\dagger(\mathbf{r},\sigma')\delta_{\sigma,\sigma'}, \\
\left[\int d\mathbf{r}'\hat{\psi}^\dagger(\mathbf{r}',\sigma')\hat{\psi}(\mathbf{r}',\sigma'), \hat{\psi}(\mathbf{r},\sigma)\right] &= -\hat{\psi}(\mathbf{r},\sigma')\delta_{\sigma,\sigma'},
\end{aligned} \tag{2.25}$$

and

$$\begin{aligned}
\left[\int d\mathbf{r}'\hat{\psi}(\mathbf{r}',\sigma')\hat{\psi}(\mathbf{r}',\sigma''), \hat{\psi}^\dagger(\mathbf{r},\sigma)\right] &= \hat{\psi}(\mathbf{r},\sigma')\delta_{\sigma,\sigma''} - \hat{\psi}(\mathbf{r},\sigma'')\delta_{\sigma,\sigma'}, \\
\left[\int d\mathbf{r}'\hat{\psi}^\dagger(\mathbf{r}',\sigma')\hat{\psi}^\dagger(\mathbf{r}',\sigma''), \hat{\psi}(\mathbf{r},\sigma)\right] &= \hat{\psi}^\dagger(\mathbf{r},\sigma')\delta_{\sigma,\sigma''} - \hat{\psi}^\dagger(\mathbf{r},\sigma'')\delta_{\sigma,\sigma'}.
\end{aligned} \tag{2.26}$$

If we insert these commutation relations into (2.24), using the Hamiltonian in Eq. (2.1), we obtain

$$\begin{aligned}\left[H, \hat{\psi}(\mathbf{r}, \uparrow)\right] &= -H_e \hat{\psi}(\mathbf{r}, \uparrow) - \Delta(\mathbf{r}) \hat{\psi}^\dagger(\mathbf{r}, \downarrow), \\ \left[H, \hat{\psi}(\mathbf{r}, \downarrow)\right] &= -H_e \hat{\psi}(\mathbf{r}, \downarrow) + \Delta(\mathbf{r}) \hat{\psi}^\dagger(\mathbf{r}, \uparrow).\end{aligned} \tag{2.27}$$

We now perform the Bogoliubov transformation of the field operators, resulting in

$$\begin{aligned}\left[H, \hat{\psi}(\mathbf{r}, \uparrow)\right] &= \sum_{\mathbf{k},\sigma} \left[\Big(- H_e u_{\mathbf{k},\uparrow,\sigma} - \Delta_{\mathbf{k}} v_{\mathbf{k},\downarrow,\sigma} \Big) \gamma_{\mathbf{k},\sigma} - \Big(- H_e v^*_{\mathbf{k},\uparrow,\sigma} + \Delta_{\mathbf{k}} u^*_{\mathbf{k},\downarrow,\sigma} \Big) \gamma^\dagger_{\mathbf{k},\sigma} \right], \\ \left[H, \hat{\psi}(\mathbf{r}, \downarrow)\right] &= \sum_{\mathbf{k},\sigma} \left[\Big(- H_e u_{\mathbf{k},\downarrow,\sigma} - \Delta_{\mathbf{k}} v_{\mathbf{k},\uparrow,\sigma} \Big) \gamma_{\mathbf{k},\sigma} + \Big(- H_e v^*_{\mathbf{k},\downarrow,\sigma} + \Delta_{\mathbf{k}} u^*_{\mathbf{k},\uparrow,\sigma} \Big) \gamma^\dagger_{\mathbf{k},\sigma} \right].\end{aligned} \tag{2.28}$$

When calculating the commutator the second way, we insert the Bogoliubov transformations of the operators from Eq. (2.13) into the Hamiltonian before computing the commutator. We know that these operators by definition diagonalize the Hamiltonian, implying

$$\begin{aligned}\left[H, \gamma_{\mathbf{k},\sigma}\right] &= -E_{\mathbf{k},\sigma} \gamma_{\mathbf{k},\sigma}, \\ \left[H, \gamma^\dagger_{\mathbf{k},\sigma}\right] &= E_{\mathbf{k},\sigma} \gamma^\dagger_{\mathbf{k},\sigma},\end{aligned} \tag{2.29}$$

where we have used the anticommutation relations of the $\gamma_{\mathbf{k},\sigma}$-operators. If we additionally calculate the commutator in Eq. (2.24) explicitly after inserting the Bogoliubov transformation, we finally obtain

$$\begin{aligned}\left[H, \hat{\psi}(\mathbf{r}, \uparrow)\right] &= \sum_{\mathbf{k},\sigma} \Big(- u_{\mathbf{k},\uparrow,\sigma} E_{\mathbf{k},\sigma} \gamma_{\mathbf{k},\sigma} - v^*_{\mathbf{k},\uparrow,\sigma} E_{\mathbf{k},\sigma} \gamma^\dagger_{\mathbf{k},\sigma} \Big), \\ \left[H, \hat{\psi}(\mathbf{r}, \downarrow)\right] &= \sum_{\mathbf{k},\sigma} \Big(- u_{\mathbf{k},\downarrow,\sigma} E_{\mathbf{k},\sigma} \gamma_{\mathbf{k},\sigma} + v^*_{\mathbf{k},\downarrow,\sigma} E_{\mathbf{k},\sigma} \gamma^\dagger_{\mathbf{k},\sigma} \Big).\end{aligned} \tag{2.30}$$

The commutator has now been calculated in two different ways. Equate Eqs. (2.28) and (2.30), which gives the following set of equations:

$$\begin{aligned} H_e u_{\mathbf{k},\uparrow,\sigma} + \Delta v_{\mathbf{k},\downarrow,\sigma} &= E_{\mathbf{k},\sigma} u_{\mathbf{k},\uparrow,\sigma}, \\ H_e u_{\mathbf{k},\downarrow,\sigma} + \Delta v_{\mathbf{k},\uparrow,\sigma} &= E_{\mathbf{k},\sigma} u_{\mathbf{k},\downarrow,\sigma}, \\ -H^*_e v_{\mathbf{k},\uparrow,\sigma} + \Delta^* u_{\mathbf{k},\downarrow,\sigma} &= E_{\mathbf{k},\sigma} v_{\mathbf{k},\uparrow,\sigma}, \\ -H^*_e v_{\mathbf{k},\downarrow,\sigma} + \Delta^* u_{\mathbf{k},\uparrow,\sigma} &= E_{\mathbf{k},\sigma} v_{\mathbf{k},\downarrow,\sigma}. \end{aligned} \tag{2.31}$$

These are the BdG equations, commonly represented as a matrix equation

$$\begin{pmatrix} H_e & 0 & 0 & \Delta \\ 0 & H_e & \Delta & 0 \\ 0 & \Delta^* & -H^*_e & 0 \\ \Delta^* & 0 & 0 & -H^*_e \end{pmatrix} \begin{pmatrix} u_{\mathbf{k},\uparrow,\sigma}(\mathbf{r}) \\ u_{\mathbf{k},\downarrow,\sigma}(\mathbf{r}) \\ v_{\mathbf{k},\uparrow,\sigma}(\mathbf{r}) \\ v_{\mathbf{k},\downarrow,\sigma}(\mathbf{r}) \end{pmatrix} = E_{\mathbf{k},\sigma} \begin{pmatrix} u_{\mathbf{k},\uparrow,\sigma}(\mathbf{r}) \\ u_{\mathbf{k},\downarrow,\sigma}(\mathbf{r}) \\ v_{\mathbf{k},\uparrow,\sigma}(\mathbf{r}) \\ v_{\mathbf{k},\downarrow,\sigma}(\mathbf{r}) \end{pmatrix}. \tag{2.32}$$

By finding the eigenvectors of this matrix, one also finds the eigenstates of the physical system. Note that the exact looks of the BdG equations depend upon the Bogoliubov transformation. If we choose another sign convention in the Bogoliubov transformation, these changes will cause sign changes in the BdG equations as well. In the literature, one usually finds this convention, in addition to one in which there is a negative sign on the anti-diagonal of the matrix in the bottom left corner.

We now want to include an electric potential, $V(\mathbf{r})$, and a magnetic field, $\mathbf{h}(\mathbf{r})$, to the Hamiltonian in Eq. (2.1). We define the magnetic field $\mathbf{h}(\mathbf{r})$ such that it includes the necessary constants in order to represent the magnetic field Hamiltonian as $H_h = -\mathbf{h}\cdot\hat{\boldsymbol{\sigma}}$, where $\hat{\boldsymbol{\sigma}}$ is the dimensionless spin-operator. The dimension of $\mathbf{h}$ is thus energy. The full Hamiltonian is

$$\begin{aligned} H = \sum_{\sigma} \int d\mathbf{r} \hat{\psi}^{\dagger}(\mathbf{r},\sigma)[H_e + V - \mathbf{h}\cdot\hat{\boldsymbol{\sigma}}]\hat{\psi}(\mathbf{r},\sigma) \\ + \int d\mathbf{r}\Big\{\Delta^*(\mathbf{r})\hat{\psi}(\mathbf{r},\downarrow)\hat{\psi}(\mathbf{r},\uparrow) + \Delta(\mathbf{r})\hat{\psi}^{\dagger}(\mathbf{r},\uparrow)\hat{\psi}^{\dagger}(\mathbf{r},\downarrow)\Big\}. \end{aligned} \tag{2.33}$$

The BdG equations for this system can now be derived by doing only a minor analysis of the Hamiltonian. We observe that both $V(\mathbf{r})$ and H_h enter the Hamiltonian in the same term as H_e. Since $V(\mathbf{r})$ is a scalar, it is not spin-dependent, and we may only substitute $H_e \to H_e + V(\mathbf{r})$ every time H_e appears the BdG equations. H_h however is an operator in spin space, which may be represented in terms of the Pauli matrices. The bottom half of the matrix in Eq. (2.32) is complex conjugated. While σ_x and σ_z are left unaltered by this operation, we have $\sigma_y^* = -\sigma_y$. Furthermore, σ_x and σ_y couple operators of different spin, giving them an additional minus sign in the bottom right corner, as implied by how Δ appears in the two lower lines of Eq. (2.31). Following this analysis, we obtain the BdG equations

$$\begin{pmatrix} H_e + V - h_z & -h_x + ih_y & 0 & \Delta \\ -h_x - ih_y & H_e + V + h_z & \Delta & 0 \\ 0 & \Delta^* & -(H_e^* + V - h_z) & -h_x - ih_y \\ \Delta^* & 0 & -h_x + ih_y & -(H_e^* + V + h_z) \end{pmatrix} \begin{pmatrix} u_{\mathbf{k},\uparrow}(\mathbf{r}) \\ u_{\mathbf{k},\downarrow}(\mathbf{r}) \\ v_{\mathbf{k},\uparrow}(\mathbf{r}) \\ v_{\mathbf{k},\downarrow}(\mathbf{r}) \end{pmatrix} = E_{\mathbf{k},\sigma} \begin{pmatrix} u_{\mathbf{k},\uparrow}(\mathbf{r}) \\ u_{\mathbf{k},\downarrow}(\mathbf{r}) \\ v_{\mathbf{k},\uparrow}(\mathbf{r}) \\ v_{\mathbf{k},\downarrow}(\mathbf{r}) \end{pmatrix}. \tag{2.34}$$

Note that we have dropped the σ-index which appeared in Eq. (2.32), as the Hamiltonian did not depend on this index. From now on, when we refer to the BdG equations, we refer to this matrix equation. In Chapter 2.3 we will add spin-orbit coupling to the Hamiltonian. By utilizing the analysis made in this chapter, it will however be an easy task to determine how spin-orbit coupling enters the BdG equations.

2.3 Spin-orbit coupling

2.3.1 Derivation in the first quantization

An electron possesses electric charge and spin, both of which interact with an electromagnetic (EM) field. For an electron which is stationary relative to an EM field, the

charge will couple to the electric field, **E**, while the spin will couple to the magnetic field, **B**. These two couplings correspond to the Coulomb and Zeeman interaction. However, if there is a relative motion between the electron and the EM field, cross couplings will occur. To derive this, we refer to a result of special relativity. The Lorentz transformation of an EM field between two inertial frames of reference reads

$$\begin{aligned}
\mathbf{E}'_{\parallel} &= \mathbf{E}_{\parallel} \\
\mathbf{B}'_{\parallel} &= \mathbf{B}_{\parallel} \\
\mathbf{E}'_{\perp} &= \gamma(\mathbf{E}_{\perp} + \mathbf{v} \times \mathbf{B}) \\
\mathbf{B}'_{\perp} &= \gamma(\mathbf{B}_{\perp} - \frac{1}{c^2}\mathbf{v} \times \mathbf{E}),
\end{aligned} \tag{2.35}$$

where the primed and un-primed variables are evaluated in the two separate inertial systems respectively, and where the $\parallel$- and $\perp$-indices refer to the field parallel to and perpendicular to the relative motion, respectively. $\mathbf{v}$ is the relative velocity of the two frames of reference, c is the speed of light in vacuum, and $\gamma = \frac{1}{\sqrt{1-v^2/c^2}}$ is the usual gamma factor. We note that this is a result of classical mechanics, where we view electrons as point objects with a well defined velocity $\mathbf{v}$. Since the energy of a system is a scalar, and scalars are invariant under Lorentz transformations, we can always evaluate the Hamiltonian of a system in any inertial reference frame of choice. We may therefore evaluate the coupling between the EM field and the electron's charge in the inertial frame in which $\mathbf{B} = 0$, and the corresponding Hamiltonian thus reduces to the Coulomb Hamiltonian. With the same argument we may go to the rest frame of the electron when evaluating the coupling between the spin and the EM field, in which frame the corresponding Hamiltonian reduces to the Zeeman interaction.

We have seen that for non-stationary electrons, there is in general a coupling between the spin and the electric field. This interaction is called spin-orbit coupling, abbreviated SOC. We now consider a system where $\mathbf{B} = 0$ in the rest frame of the physical system (in which the electrons move), that is a system without an external magnetic field. An electron moving with velocity $\mathbf{v}$ thus experiences a magnetic field[34]

$$\mathbf{B} = -\frac{\gamma}{c^2}\mathbf{v} \times \mathbf{E} \tag{2.36}$$

in its own rest frame. This magnetic field couples to the electron's magnetic moment as usual, giving the Hamiltonian contribution

$$H_{\mathrm{SO}} = -\boldsymbol{\mu}_e \cdot \mathbf{B}, \tag{2.37}$$

where $\boldsymbol{\mu}_e = \frac{e g_s}{2m_e}\mathbf{S}$ is the electron's magnetic moment. Here, $\mathbf{S}$ is the electron's spin, and m_e is the electron mass. g_s is a constant predicted to be 2 by a first order approach, corrected to $g_s \approx 2.00116$ by including *anomalous* contributions from loop calculations in quantum electrodynamics. The SOC thus enters the Hamiltonian as a magnetic field, depending however upon the electron's orbit, or more accurately, on its velocity. If we write this out, rewriting $\mathbf{v} = \hbar\mathbf{k}/m_e$ in order to only include well defined quantum mechanical variables, we end up with[35,36]

$$H_{\mathrm{SO}} = -\alpha_R \boldsymbol{\sigma} \cdot (\hat{\mathbf{n}} \times \mathbf{k}), \tag{2.38}$$

where we have written the spin operator $\mathbf{S} = \frac{\hbar}{2}\boldsymbol{\sigma}$ in terms of the dimensionless Pauli matrices, $\boldsymbol{\sigma}$, and written the electric field as $\mathbf{E} = E\hat{\mathbf{n}}$. We have also defined $\alpha_R = \frac{\gamma g_s e \hbar^2 E}{4 m_e^2 c^2}$, where we set $\gamma = 1$ as a reasonable approximation for the relevant conditions in solid-state physics. Now apply the vector identity $\mathbf{a} \cdot (\mathbf{b} \times \mathbf{c}) = \mathbf{b} \cdot (\mathbf{c} \times \mathbf{a})$, valid for any vectors $\mathbf{a}$, $\mathbf{b}$ and $\mathbf{c}$, and rewrite $\boldsymbol{\sigma} \cdot (\hat{\mathbf{n}} \times \mathbf{k}) = (\boldsymbol{\sigma} \times \hat{\mathbf{n}}) \cdot \mathbf{k}$. The SOC Hamiltonian thus takes the form

$$H_{\mathrm{SO}} = \alpha_R \cdot (\hat{\mathbf{n}} \times \boldsymbol{\sigma})\mathbf{k}. \tag{2.39}$$

To give an interpretation of the effect SOC has on the electrons, we add the kinetic contribution to the Hamiltonian in Eq. (2.39). By completing the square, we obtain[37,38]

$$H_e + H_{\mathrm{SO}} = \frac{\hbar^2}{2m_e}\Big(\mathbf{k} + \mathbf{k}_{\mathrm{SO}}\Big)^2 - \frac{\hbar^2 \mathbf{k}_{\mathrm{SO}}^2}{2m_e}, \tag{2.40}$$

where we implicitly defined $\mathbf{k}_{\mathrm{SO}} = \frac{m_e}{\hbar^2}\alpha_R(\hat{\mathbf{n}} \times \boldsymbol{\sigma})$. Note that $\mathbf{k}_{\mathrm{SO}} \propto (\hat{\mathbf{n}} \times \boldsymbol{\sigma})$, which is an operator in spin space. Thus SOC lifts the spin degeneracy by moving the minima of the dispersion relations for different spin polarizations differently. If we quantize the spin along the direction of the eigenstates of $\mathbf{k}_{\mathrm{SO}}$, we can treat $\mathbf{k}_{\mathrm{SO}}$ as a usual vector, and the minimum of the dispersion relation thus shifts $\pm\mathbf{k}_{\mathrm{SO}}$ for spin-up or spin-down electrons in this quantization direction, dependent upon the electrons momentum $\mathbf{k}$. We further note that an electron described by the state $|\mathbf{k}, \uparrow\rangle$ and another one described by $|-\mathbf{k}, \downarrow\rangle$ experience the same shift in the dispersion relation.

2.3.2 Transition to the second quantization

By using the definition of second quantized operators expressed in the spin-momentum basis, the general spin-orbit coupling Hamiltonian reads

$$H_{\mathrm{SO}} = \sum_{\mathbf{k}',\mathbf{k}'',\sigma',\sigma''} \langle \mathbf{k}', \sigma' | \alpha_{\mathrm{R}} (\hat{\mathbf{n}} \times \boldsymbol{\sigma}) \cdot \mathbf{k} | \mathbf{k}'', \sigma'' \rangle \, c^{\dagger}_{\mathbf{k}',\sigma'} c_{\mathbf{k}'',\sigma''}, \tag{2.41}$$

where the summation over σ' is a summation over a complete set of spin quantum numbers, but where we in general have not explicitly defined the spin quantization axis. We also treat the electric field, E, as a constant, and will come back to this issue later. Without loss of generalization, we now choose the z-axis to be the spin quantization axis. An explicit calculation of Eq. (2.41), using the Pauli matrices representation for $\boldsymbol{\sigma}$ and the orthogonality relation $\langle \mathbf{k}', \sigma' | \mathbf{k}'', \sigma'' \rangle = \delta_{\mathbf{k}',\mathbf{k}''}\delta_{\sigma',\sigma''}$, gives

$$H_{\mathrm{SO}} = H^x_{\mathrm{SO}} + H^y_{\mathrm{SO}} + H^z_{\mathrm{SO}}, \tag{2.42}$$

where we have defined

$$
\begin{aligned}
H_{\mathrm{SO}}^{x} &= \sum_{\mathbf{k},\sigma} \Big[\alpha_{\mathrm{R}}(n_z k_y - n_y k_z)\Big] c^{\dagger}_{\mathbf{k},\sigma} c_{\mathbf{k},-\sigma}, \\
H_{\mathrm{SO}}^{y} &= \sum_{\mathbf{k},\sigma} \Big[-i\sigma\alpha_{\mathrm{R}}(n_x k_z - n_z k_x)\Big] c^{\dagger}_{\mathbf{k},\sigma} c_{\mathbf{k},-\sigma}, \\
H_{\mathrm{SO}}^{z} &= \sum_{\mathbf{k},\sigma} \Big[\sigma\alpha_{\mathrm{R}}(n_y k_x - n_x k_y)\Big] c^{\dagger}_{\mathbf{k},\sigma} c_{\mathbf{k},\sigma},
\end{aligned}
\tag{2.43}
$$

where the n_i's are the components of $\hat{\mathbf{n}}$, the unit vector pointing in the direction of the electric field.

We may now interpret the effect of SOC even further. Like the magnetic field Hamiltonian, H_h, this Hamiltonian has one diagonal contribution, H_{SO}^{z}, and two spin-flip contributions, H_{SO}^{x} and H_{SO}^{y}. Both H_h and H_{SO} are odd under spin inversion $\boldsymbol{\sigma} \to -\boldsymbol{\sigma}$ However, as opposed to the magnetic field Hamiltonian, H_{SO} is odd under $\mathbf{k} \to -\mathbf{k}$ as well, that is $H_{\mathrm{SO}}(\mathbf{k}) = -H_{\mathrm{SO}}(-\mathbf{k})$. The SOC Hamiltonian is therefore odd under parity inversion, that is a pseudoscalar.

Expressing the Hamiltonian with field operators is a straightforward process. By using the definition of the field operators, the Hamiltonian in its most general form takes the form

$$
H_{\mathrm{SO}} = \sum_{\sigma} \int d\mathbf{r} \psi^{\dagger}(\mathbf{r},\sigma)\Big[i\alpha_{\mathrm{R}}(\boldsymbol{\sigma}\times\hat{\mathbf{n}})\cdot\nabla\Big]\psi(\mathbf{r},\sigma). \tag{2.44}
$$

If we once again choose the z-axis to be the spin quantization axis, we obtain the Hamiltonian given in Eq. (2.42), but with each term given as

$$
\begin{aligned}
H_{\mathrm{SO}}^{x} &= -\sum_{\sigma} \int d\mathbf{r} \psi^{\dagger}(\mathbf{r},\sigma)\Big[i\alpha_{\mathrm{R}}\Big(n_z\frac{\partial}{\partial y} - n_y\frac{\partial}{\partial z}\Big)\Big]\psi(\mathbf{r},-\sigma), \\
H_{\mathrm{SO}}^{y} &= i\sum_{\sigma} \int d\mathbf{r} \psi^{\dagger}(\mathbf{r},\sigma)\Big[i\sigma\alpha_{\mathrm{R}}\Big(n_x\frac{\partial}{\partial z} - n_z\frac{\partial}{\partial x}\Big)\Big]\psi(\mathbf{r},-\sigma), \\
H_{\mathrm{SO}}^{z} &= -\sum_{\sigma} \int d\mathbf{r} \psi^{\dagger}(\mathbf{r},\sigma)\Big[i\sigma\alpha_{\mathrm{R}}\Big(n_y\frac{\partial}{\partial x} - n_x\frac{\partial}{\partial y}\Big)\Big]\psi(\mathbf{r},\sigma).
\end{aligned}
\tag{2.45}
$$

which are analogous to the spin-momentum-space versions in Eq. (2.43), only expressed with field operators. We observe that the Hamiltonian is still diagonal in H_{SO}^{z}, while H_{SO}^{x} and H_{SO}^{y} represent spin-flip events. If we define the SOC-operators (~ is used to mark that it is an operator, as we reserve the more conventional ^ for use later in the thesis)

$$
\tilde{h}_{\mathrm{SO}}^{k} = i\alpha_{\mathrm{R}}\epsilon_{klm} n_m \frac{\partial}{\partial l}, \quad k,l,m \in \{x,y,z\} \tag{2.46}
$$

where ϵ_{klm} is the antisymmetric tensor of rank 3, and where Einstein's summation convention is implied, we observe that we may write

$$
\begin{aligned}
H_{\mathrm{SO}}^{x} &= -\int d\mathbf{r}\Psi^{\dagger}(\mathbf{r})\sigma_x\tilde{h}_{\mathrm{SO}}^{x}\Psi(\mathbf{r}),\\
H_{\mathrm{SO}}^{y} &= -\int d\mathbf{r}\Psi^{\dagger}(\mathbf{r})\sigma_y\tilde{h}_{\mathrm{SO}}^{y}\Psi(\mathbf{r}),\\
H_{\mathrm{SO}}^{z} &= -\int d\mathbf{r}\Psi^{\dagger}(\mathbf{r})\sigma_z\tilde{h}_{\mathrm{SO}}^{z}\Psi(\mathbf{r}),
\end{aligned}
\tag{2.47}
$$

where $\Psi(\mathbf{r}) = [\psi(\mathbf{r},\uparrow),\psi(\mathbf{r},\downarrow)]^{\mathrm{T}}$ are spinors, and where the σ_i's are the Pauli matrices. Writing the Hamiltonian on this form confirms that the $\tilde{h}_{\mathrm{SO}}^{i}$-terms enter the Hamiltonian like magnetic fields, just like we found in the classical derivation. There is however one important difference, namely that the SOC-induced magnetic field, given in Eq. (2.46), is $\mathbf{k}$-dependent.

2.3.3 Spin-orbit coupling at an interface

From the derivation of SOC, we have found quite generally that this is a phenomenon which arises when electrons move within a gradient in the electric potential. Strictly speaking, there is a potential gradient everywhere, as the world is not completely homogeneous. In solid-state physics, materials are often structured in lattices at the atomic level. The electric potential will in general be position dependent inside the lattice, thus implying a potential gradient everywhere. However, if we average this effect over the unit cell, the effect disappears inside a lattice which preserves inversion invariance. In the following we will do this approximation, thus neglecting the contributions to SOC which emerges at smaller length scales than the unit cell.

Potential gradients in solid-state materials are in general found where there is an inversion asymmetry,[39,40] in other words, where the lattice is invariant under the inversion operation. An example where this occurs is at the interface between two different materials, or at the surface of a material (which is an interface between the material and what surrounds it). Such an interface is characterized by a normal (unit-)vector $\hat{\mathbf{n}}$, which is perpendicular to the interface plane. Due to the symmetry of such a problem, the potential gradient, and thus the corresponding electric field, ought to be parallel to $\hat{\mathbf{n}}$. The field only appears where there is a gradient in the electric potential, and thus disappears sufficiently far away from the interface.

We now look at SOC at a planar interface between two materials. We define the system such that the interface forms a plane of infinite extent, take for instance the yz-plane, equivalent to defining $\hat{\mathbf{n}} = \hat{\mathbf{x}}$. Looking back at the Hamiltonian in Eq. (2.45), we observe that only those terms containing n_x survive. For this system, we are thus left with the following terms in the Hamiltonian:

$$
\begin{aligned}
H_{\mathrm{SO}}^{x} &= 0,\\
H_{\mathrm{SO}}^{y} &= i\sum_{\sigma}\int d\mathbf{r}\psi^{\dagger}(\mathbf{r},\sigma)\Big[i\sigma\alpha_{\mathrm{R}}n_x\frac{\partial}{\partial z}\Big]\psi(\mathbf{r},-\sigma),\\
H_{\mathrm{SO}}^{z} &= \sum_{\sigma}\int d\mathbf{r}\psi^{\dagger}(\mathbf{r},\sigma)\Big[i\sigma\alpha_{\mathrm{R}}n_x\frac{\partial}{\partial y}\Big]\psi(\mathbf{r},\sigma).
\end{aligned}
\tag{2.48}
$$

If we once again apply the definitions in Eq. (2.46), only $\tilde{h}^y_{\mathrm{SO}}$ and $\tilde{h}^z_{\mathrm{SO}}$ remain non-zero. In such a system, with a planar interface, the electrons thus effectively experience a magnetic field in the interface. This magnetic field is momentum-dependent, and its direction is parallel to the plane of interface.

2.3.4 In-plane spin-orbit coupling

Let us now define a two-dimensional system. The system is of infinite length in the z-direction (that is, translationally invariant), while it is of finite length in the x-direction. We define $x = 0$ such that for $x > 0$ there is an electric field perpendicular to the system which induces SOC. In other words, $E(x) = E\Theta(x)$, where $\Theta(x)$ is the unit step function. Moreover, as the system is in the xz-plane, we must have $\hat{n} = \pm\hat{y}$. This introduces a challenge, as the Hamiltonian seemingly becomes

$$H_{\mathrm{SO}} = \alpha_R(x)[\sigma_z k_x - \sigma_x k_z]. \tag{2.49}$$

However, this Hamiltonian is not hermitian, as

$$\Big(\alpha_{\mathrm{R}}(x)k_x\Big)^\dagger \propto \Big(i\Theta(x)\frac{\partial}{\partial x}\Big)^\dagger = i\frac{\partial}{\partial x}\Theta(x) \neq i\Theta(x)\frac{\partial}{\partial x}. \tag{2.50}$$

We require the Hamiltonian to be hermitian, and must therefore rewrite the Hamiltonian with the requirement that it simplifies to Eq. (2.49) if we were to interpret the expression in the classical limit. This is obtained if we *symmetrize* the Hamiltonian, by writing it in terms of an anticommutator,

$$H_{\mathrm{SO}} = \frac{1}{2}\{\alpha_{\mathrm{R}}(x), [\sigma_z k_x - \sigma_x k_z]\}. \tag{2.51}$$

As the term including k_z does not cause problems regarding the hermiticity of the Hamiltonian, we need not write this term in the anticommutator. This also applies for the interfacial SOC discussed in section 2.3.3, as the resulting Hamiltonian in Eq. (2.48) is hermitian. Explicit calculation of the anticommutator results in

$$H_{\mathrm{SO}} = \alpha_{\mathrm{R}}(x)\Big[\sigma_z k_x - \sigma_x k_z\Big] - \frac{i}{2}\alpha_{\mathrm{R}}\delta(x)\sigma_z, \tag{2.52}$$

where the position independent Rashba parameter is defined by $\alpha_{\mathrm{R}}(x) \equiv \alpha_{\mathrm{R}}\Theta(x)$. Note that the difference between the non-hermitian and hermitian Hamiltonians in Eqs. (2.49) and (2.52) is an additional term. This term is proportional to $\sigma_z\delta(x)$, and thus enters the Hamiltonian just like a magnetic field in the z-direction at $x = 0$. A difference is however that this *effective* magnetic field is imaginary, as ensured by the imaginary unit i which comes from $k_x = -i\frac{\partial}{\partial x}$. The second quantized Hamiltonian, expressed with field operators, becomes

$$
\begin{aligned}
H^x_{\mathrm{SO}} &= \sum_\sigma \int d\mathbf{r}\psi^\dagger(\mathbf{r},\sigma)\Big[i\alpha_{\mathrm{R}}(x)\frac{\partial}{\partial z}\Big]\psi(\mathbf{r},-\sigma),\\
H^y_{\mathrm{SO}} &= 0,\\
H^z_{\mathrm{SO}} &= \sum_\sigma \int d\mathbf{r}\psi^\dagger(\mathbf{r},\sigma)\sigma\Big[-i\alpha_{\mathrm{R}}(x)n_x\frac{\partial}{\partial y}-\frac{i}{2}\alpha_{\mathrm{R}}\delta(x)\Big]\psi(\mathbf{r},\sigma),
\end{aligned}
\tag{2.53}
$$

The full Hamiltonian is, as before, $H_{\mathrm{SO}} = H^x_{\mathrm{SO}} + H^y_{\mathrm{SO}} + H^z_{\mathrm{SO}}$.

2.3.5 Implementing spin-orbit coupling in the BdG formalism

We have already derived the BdG equations for a system with s-wave superconductivity, a magnetic field and an electric potential. We now want to implement SOC into this formalism. We remember from Chapter 2.2 that the process involved first diagonalizing the Hamiltonian, and then to compute commutation relations $[H,\psi(\mathbf{r},\sigma_z)]$ in two different ways. We now make use of our previous observation, that the SOC enters the Hamiltonian almost as a magnetic field. By using the definitions of the SOC operators $\tilde{h}^k_{\mathrm{SO}}$ in Eq. (2.46), and only include SOC in addition to the kinetic term, we obtain

$$
\begin{aligned}
&\begin{pmatrix}
H_{\mathrm{e}}-\tilde{h}^z_{\mathrm{SO}} & -\tilde{h}^x_{\mathrm{SO}}+i\tilde{h}^y_{\mathrm{SO}} & 0 & \Delta\\
-\tilde{h}^x_{\mathrm{SO}}-i\tilde{h}^y_{\mathrm{SO}} & H_{\mathrm{e}}+\tilde{h}^z_{\mathrm{SO}} & \Delta & 0\\
0 & \Delta^* & -(H^*_{\mathrm{e}}-\tilde{h}^z_{\mathrm{SO}}) & -\tilde{h}^x_{\mathrm{SO}}-i\tilde{h}^y_{\mathrm{SO}}\\
\Delta^* & 0 & -\tilde{h}^x_{\mathrm{SO}}+i\tilde{h}^y_{\mathrm{SO}} & -(H^*_{\mathrm{e}}+\tilde{h}^z_{\mathrm{SO}})
\end{pmatrix}
\begin{pmatrix}
u_{\mathbf{k},\uparrow}(\mathbf{r})\\ u_{\mathbf{k},\downarrow}(\mathbf{r})\\ v_{\mathbf{k},\uparrow}(\mathbf{r})\\ v_{\mathbf{k},\downarrow}(\mathbf{r})
\end{pmatrix}\\
&= E_{\mathbf{k}}\begin{pmatrix}
u_{\mathbf{k},\uparrow}(\mathbf{r})\\ u_{\mathbf{k},\downarrow}(\mathbf{r})\\ v_{\mathbf{k},\uparrow}(\mathbf{r})\\ v_{\mathbf{k},\downarrow}(\mathbf{r})
\end{pmatrix}.
\end{aligned}
\tag{2.54}
$$

which is identical to the BdG equations for magnetic fields, only with $\mathbf{h} \to \tilde{\mathbf{h}}_{\mathrm{SO}}$. However, the operator $\tilde{\mathbf{h}}_{\mathrm{SO}}$ is momentum dependent. Furthermore, hole-like particles have inverted momentum, $\mathbf{k} \to -\mathbf{k}$. As we observed in the last section, H_{SO} is odd under the inversion operation $\mathbf{k} \to -\mathbf{k}$, thus giving a sign switch in the BdG equations for hole-like amplitudes. We thus define h^i_{SO} for $i \in \{x,y,z\}$ such that

$$
\begin{aligned}
\tilde{h}^i_{\mathrm{SO}}u_{\mathbf{k},\sigma} &\equiv h^i_{\mathrm{SO}}u_{\mathbf{k},\sigma},\\
\tilde{h}^i_{\mathrm{SO}}v_{\mathbf{k},\sigma} &\equiv -h^i_{\mathrm{SO}}v_{\mathbf{k},\sigma}.
\end{aligned}
\tag{2.55}
$$

In other words, there is a sign inversion when the operator $\tilde{h}^i_{\mathrm{SO}}$ acts on the hole-like amplitudes. The h^i_{SO}'s are still momentum-dependent, but the hole-/particle-dependence is removed. Inserting this definition into the BdG equations yields

$$\begin{pmatrix} H_e - h_{SO}^z & -h_{SO}^x + ih_{SO}^y & 0 & \Delta \\ -h_{SO}^x - ih_{SO}^y & H_e + h_{SO}^z & \Delta & 0 \\ 0 & \Delta^* & -(H_e^* + h_{SO}^z) & h_{SO}^x + ih_{SO}^y \\ \Delta^* & 0 & h_{SO}^x - ih_{SO}^y & -(H_e^* - h_{SO}^z) \end{pmatrix} \begin{pmatrix} u_{\mathbf{k},\uparrow}(\mathbf{r}) \\ u_{\mathbf{k},\downarrow}(\mathbf{r}) \\ v_{\mathbf{k},\uparrow}(\mathbf{r}) \\ v_{\mathbf{k},\downarrow}(\mathbf{r}) \end{pmatrix} = E_{\mathbf{k}} \begin{pmatrix} u_{\mathbf{k},\uparrow}(\mathbf{r}) \\ u_{\mathbf{k},\downarrow}(\mathbf{r}) \\ v_{\mathbf{k},\uparrow}(\mathbf{r}) \\ v_{\mathbf{k},\downarrow}(\mathbf{r}) \end{pmatrix}. \tag{2.56}$$

It can be observed that the SOC terms enter the BdG equations just as a magnetic field for the particle-like amplitudes, $u_{\mathbf{k},\sigma}(\mathbf{r})$, only with a momentum dependence. However, for the hole-like amplitudes, $v_{\mathbf{k},\sigma}(\mathbf{r})$, there is a switch of signs.

2.4 Rotating the spin basis

When spin-$\frac{1}{2}$ degrees of freedom are present in a system, the z-axis is usually used as the quantization axis, and the spin is quantized as $s_z = \pm\frac{1}{2}$. The physics must however be invariant of the choice of quantization axis, and we may thus choose whichever axis we want. The z-axis usually gives the easiest formalism, hence its widespread use. When s_z is not a well defined quantum number, it may however be more intuitive to rotate the quantization axis so that it captures the spin eigenstates of the system.

2.4.1 Rotation in the presence of a magnetic field

The magnetic field Hamiltonian is in general

$$\mathbf{H}_h = -\mathbf{h}\cdot\hat{\boldsymbol{\sigma}}, \tag{2.57}$$

where $\hat{\boldsymbol{\sigma}}$ is the vector of Pauli matrices. With a uniform magnetic field present, and no other spin-dependent terms, the spin along the direction of the magnetic field is a good quantum number. We will now derive how to rotate z-states into the new set of eigenstates. By defining $I_i = h_i/h_0$, where h_0 is the total magnetic field strength, we can write this Hamiltonian more explicitly as

$$\mathbf{H}_h = -h_0 \begin{pmatrix} I_z & I_x - iI_y \\ I_x + iI_y & -I_z \end{pmatrix}. \tag{2.58}$$

For simplicity, let the magnetic field rotate only in the xz-plane. One can then diagonalize this matrix by applying the same diagonalization procedure as was done to the BCS Hamiltonian in Chapter 2.2, namely $\mathbf{D} = \mathbf{P}\mathbf{H}_h\mathbf{P}^\dagger$, where $\mathbf{D}$ is the diagonalized matrix, and $\mathbf{P}$ is the diagonalization matrix, of which columns are the eigenvectors of $\mathbf{H}_h$. Let the set of $|\psi_n\rangle$ be the eigenvectors of $\mathbf{H}_h$, and $\left|\psi_n'\right\rangle$ be the eigenvectors of $\mathbf{D}$. The eigenvalue problem is originally

$$\mathbf{H}_h |\psi_n\rangle = E_n |\psi_n\rangle, \tag{2.59}$$

which by insertion of the diagonalization procedure becomes

$$\mathbf{D}\left|\psi_n^{'}\right\rangle = E_n\left|\psi_n^{'}\right\rangle, \tag{2.60}$$

where $\left|\psi_n^{'}\right\rangle = \mathbf{P}\left|\psi_n\right\rangle$. Since Eq. (2.60) can easily be solved, due to $\mathbf{D}$ being diagonal, we can now identify the eigenstates. The new spin states span the same subspace of the Hilbert space of states as the old spin states, and there are thus two possible states. We name the new eigenstates, that is the set of $\left|\psi_n^{'}\right\rangle$, $\left|\uparrow^{'}\right\rangle$ and $\left|\downarrow^{'}\right\rangle$, where the prime indicates that these are spin-up and spin-down along a new z'-axis, that is the new axis of quantization. Explicit calculation yields

$$\begin{aligned}\left|\uparrow^{'}\right\rangle &= \frac{1}{\sqrt{2(1+I_z)}}\left[(1+I_z)\left|\uparrow\right\rangle_z + I_x\left|\downarrow\right\rangle_z\right],\\ \left|\downarrow^{'}\right\rangle &= \frac{1}{\sqrt{2(1+I_z)}}\left[(1+I_z)\left|\downarrow\right\rangle_z - I_x\left|\uparrow\right\rangle_z\right],\end{aligned} \tag{2.61}$$

where $\left|\sigma\right\rangle_z$ are the eigenvectors of the Pauli σ_z-matrix, which correspond to spin-up and spin-down along z. One can check that these solutions reduce to the eigenvectors of either the σ_x- or σ_z-matrix if we set $I_x = 1$ or $I_z = 1$, respectively.

In this new rotated system, the s_z-states are no longer single-particle energy eigenstates, and they are thus not stable states. Considering Cooper pairs in this system, we should therefore rather form the pairs by the rotated $\left|\pm\mathbf{k}, \sigma^{'}\right\rangle$-states. Let $\psi(\mathbf{k})$ denote an arbitrary Cooper pair state. Formally, the Cooper pair states must be symmetric under the transformation $\mathbf{k} \to -\mathbf{k}$, that is $\psi(\mathbf{k}) = \psi(-\mathbf{k})$. To simplify the notation, the states we use in this chapter do not satisfy this requirement. However, it can be easily restored by letting $\psi(\mathbf{k}) \to \psi(\mathbf{k}) + \psi(-\mathbf{k})$ in the results for all Cooper pair states.

In general, the Cooper pair states expressed in terms of the eigenstates of a system will not be equal to those obtained with the z-axis as quantization axis. We now want to derive how these are related, analogous to what we did for single-particle states in Eq. (2.61). We temporarily neglect the non-zero center-of-mass momentum (CoM) the Cooper pairs gain inside a ferromagnet, and express all single-particle states with equal momentum $\mathbf{k}$, as the notation becomes less heavy. Insert $I_x = \sin(\theta)$ and $I_z = \cos(\theta)$ into Eq. (2.61), and it follows that the singlet state transforms as

$$\left|\mathbf{k}, \uparrow^{'}\right\rangle\left|-\mathbf{k}, \downarrow^{'}\right\rangle - \left|\mathbf{k}, \downarrow^{'}\right\rangle\left|-\mathbf{k}, \uparrow^{'}\right\rangle = \left|\mathbf{k}, \uparrow\right\rangle\left|-\mathbf{k}, \downarrow\right\rangle - \left|\mathbf{k}, \downarrow\right\rangle\left|-\mathbf{k}, \uparrow\right\rangle, \tag{2.62}$$

that is, it does not transform at all. This is a logical result, as the the singlet state has no net spin, and should therefore be independent upon the choice of quantization axis. As for the triplet ($s' = 0$)-state, in which s' denotes the spin quantum number along the new quantization axis, we obtain

$$\begin{aligned}\left|\mathbf{k},\uparrow'\right\rangle\left|-\mathbf{k},\downarrow'\right\rangle + \left|\mathbf{k},\downarrow'\right\rangle\left|-\mathbf{k},\uparrow'\right\rangle = \cos(\theta)\Big[\,|\mathbf{k},\uparrow\rangle|-\mathbf{k},\downarrow\rangle + |\mathbf{k},\downarrow\rangle|-\mathbf{k},\uparrow\rangle\,\Big] \\ + \sin(\theta)\Big[\,|\mathbf{k},\uparrow\rangle|-\mathbf{k},\uparrow\rangle - |\mathbf{k},\downarrow\rangle|-\mathbf{k},\downarrow\rangle\,\Big].\end{aligned} \tag{2.63}$$

This state is thus a superposition between triplet ($s_z = 0$)- and a ($s_z = \pm 1$)-state. With $\theta = \pi/2$, it is a pure ($s_z = \pm 1$)-state. Equivalently, we obtain

$$\begin{aligned}\left|\mathbf{k},\uparrow'\right\rangle\left|-\mathbf{k},\uparrow'\right\rangle - \left|\mathbf{k},\downarrow'\right\rangle\left|-\mathbf{k},\downarrow'\right\rangle = \cos(\theta)\Big[\,|\mathbf{k},\uparrow\rangle|-\mathbf{k},\uparrow\rangle - |\mathbf{k},\downarrow\rangle|-\mathbf{k},\downarrow\rangle\,\Big] \\ - \sin(\theta)\Big[\,|\mathbf{k},\uparrow\rangle|-\mathbf{k},\downarrow\rangle + |\mathbf{k},\downarrow\rangle|-\mathbf{k},\uparrow\rangle\,\Big]\end{aligned} \tag{2.64}$$

for the triplet ($s' = \pm 1$)-state. Note that if the full Hamiltonian commutes with the σ'-operator, the ($s' = \pm 1$)-pairs would strictly speaking not arise. Putting this system together with an s-wave superconductor does not cause any violation of the conservation of s', as the superconductor produces pairs with $s' = 0$, and we would thus not expect this form of Cooper pairing to occur. The derivation of the rotation of the spin basis is however made completely general, and does not depend on any amplitudes being non-zero. By keeping the expressions general, we may also interpret what happens when putting this system together with a ferromagnet perpendicularly aligned to the first ferromagnet. Sufficiently far from the second ferromagnet, the s'-spin states will be approximate eigenstates. However, the second ferromagnetic region introduces a source of ($s' = \pm 1$)-pairs in the system. These pairs may progress trough the first ferromagnet without gaining a finite CoM, giving them the name "long-ranged" triplets.

When expressing the Cooper pair correlations, defined in Chapter 2.1.1, all choices of spin quantum numbers are equivalent. That is, all physics is captured by f_0, f_1 and f_2 combined for rotations in the xz-plane, although the individual amplitudes may differ depending on the choice of quantization axis. However, when evaluating how a physical interaction, such as a magnetic field, affects a single Cooper pair, it helps to rotate the basis such that the pair state is expressed with spin eigenstates, as these are in fact the stable states of the system.

2.4.2 Rotation in the presence of SOC orthogonal to a magnetic field

In Chapter 2.3, we learned that SOC enters the Hamiltonian almost like a magnetic field. There is however one important difference, namely the momentum dependence. Let us now focus on a two-dimensional version of the system discussed in Chapter 2.3.3. Let the system span the yz-plane, with a SOC-inducing interface along the y-axis, that is $\hat{n} = -\hat{z}$. The SOC Hamiltonian is then given as

$$\mathbf{H}_{\mathrm{SO}} = -\alpha_{\mathrm{R}}\sigma_x\hat{k}_y, \tag{2.65}$$

where the hat over $\hat{k}_y$ indicates that it is an operator. We will now look at a Hamiltonian which includes a magnetic field orthogonal to the SOC-induced fields. The reason why we do not keep the magnetic field orientation fully general is that the calculation in this case eventually involves a lot of messy algebra, and the result is hard to interpret. This situation will however be commented in the Chapter 2.4.3. Analogous to Eq. (2.58), we may express the aforementioned Hamiltonian as

$$\mathbf{H} = -\begin{pmatrix} h_0 & \alpha_{\mathrm{R}}\hat{k}_y \\ \alpha_{\mathrm{R}}\hat{k}_y & -h_0 \end{pmatrix}. \tag{2.66}$$

Now, define $\tilde{h} = \sqrt{h_0^2 + \alpha_{\mathrm{R}}^2|k_y|^2}$ as a net magnetic field strength, and the dimensionless quantities

$$I_h = \frac{h_0}{\tilde{h}} \equiv \cos(\theta_{\mathrm{SO}}), \qquad I_{\mathrm{SO}} = \frac{\alpha_{\mathrm{R}}k_y}{\tilde{h}} \equiv \sin(\theta_{\mathrm{SO}}). \tag{2.67}$$

By doing so, we write the analogy of Eq. (2.61), that is the normalized spin state transformations, as

$$\begin{aligned}
\left|k_y,\uparrow'\right\rangle &= \frac{1}{\sqrt{2(1+I_h)}}\left[(1+I_h)\left|k_y,\uparrow\right\rangle_z + I_{\mathrm{SO}}\left|k_y,\downarrow\right\rangle_z\right], \\
\left|-k_y,\uparrow'\right\rangle &= \frac{1}{\sqrt{2(1+I_h)}}\left[(1+I_h)\left|-k_y,\uparrow\right\rangle_z - I_{\mathrm{SO}}\left|-k_y,\downarrow\right\rangle_z\right], \\
\left|k_y,\downarrow'\right\rangle &= \frac{1}{\sqrt{2(1+I_h)}}\left[(1+I_h)\left|k_y,\downarrow\right\rangle_z - I_{\mathrm{SO}}\left|k_y,\uparrow\right\rangle_z\right], \\
\left|-k_y,\downarrow'\right\rangle &= \frac{1}{\sqrt{2(1+I_h)}}\left[(1+I_h)\left|-k_y,\downarrow\right\rangle_z + I_{\mathrm{SO}}\left|-k_y,\uparrow\right\rangle_z\right].
\end{aligned} \tag{2.68}$$

Note that there is a switch of signs between $k_y \to -k_y$ compared to Eq. (2.61), reflecting the momentum-dependence of SOC. This results implies that there is no longer a single well defined spin quantization axis,[41] as these axes depend upon the both the magnitude and direction of the momentum of the states. We have however identified the eigenstates, enabling us to write out the transformed Cooper pair states in terms of s_z-states. We name the s'-quantum numbers pseudospin, as these are not physical spins. The pseudosinglet state follows as

$$\begin{aligned}
\left|k_y,\uparrow'\right\rangle\left|-k_y,\downarrow'\right\rangle - \left|k_y,\downarrow'\right\rangle\left|-k_y,\uparrow'\right\rangle = \cos(\theta_{\mathrm{SO}})\Big[\left|k_y,\uparrow\right\rangle\left|-k_y,\downarrow\right\rangle - \left|k_y,\downarrow\right\rangle\left|-k_y,\uparrow\right\rangle\Big] \\
+ \sin(\theta_{\mathrm{SO}})\Big[\left|k_y,\uparrow\right\rangle\left|-k_y,\uparrow\right\rangle + \left|k_y,\downarrow\right\rangle\left|-k_y,\downarrow\right\rangle\Big].
\end{aligned} \tag{2.69}$$

and the pseudotriplet ($s' = \pm 1$)-state is

$$\left|k_y,\uparrow'\right\rangle\left|-k_y,\uparrow'\right\rangle+\left|k_y,\downarrow'\right\rangle\left|-k_y,\downarrow'\right\rangle=\cos\left(\theta_{\mathrm{SO}}\right)\left[\left|k_y,\uparrow\right\rangle\left|-k_y,\uparrow\right\rangle+\left|k_y,\downarrow\right\rangle\left|-k_y,\downarrow\right\rangle\right]$$
$$-\sin\left(\theta_{\mathrm{SO}}\right)\left[\left|k_y,\uparrow\right\rangle\left|-k_y,\downarrow\right\rangle-\left|k_y,\downarrow\right\rangle\left|-k_y,\uparrow\right\rangle\right]. \tag{2.70}$$

Combining these equations yields the spin singlet state expressed in terms of the eigenstates of the system, that is the pseudospin states,

$$\left|k_y,\uparrow\right\rangle\left|-k_y,\downarrow\right\rangle-\left|k_y,\downarrow\right\rangle\left|-k_y,\uparrow\right\rangle=\cos\left(\theta_{\mathrm{SO}}\right)\left[\left|k_y,\uparrow'\right\rangle\left|-k_y,\downarrow'\right\rangle-\left|k_y,\downarrow'\right\rangle\left|-k_y,\uparrow'\right\rangle\right]$$
$$-\sin\left(\theta_{\mathrm{SO}}\right)\left[\left|k_y,\uparrow'\right\rangle\left|-k_y,\uparrow'\right\rangle+\left|k_y,\downarrow'\right\rangle\left|-k_y,\downarrow'\right\rangle\right]. \tag{2.71}$$

The spin singlet state thus contains both pseudosinglet and pseudotriplet components. Note that this does not imply that the spin singlet state has gained a net spin-polarization. On the contrary, for the expression to be consistent it is indeed necessary that the pseudosinglet and pseudotriplet states combined gives no net spin polarization. Neither does it imply that we have leakage of singlet Cooper pairs through a triplet channel. It simply implies that a singlet state projected down on the eigenbasis of the Hamiltonian in Eq. (2.66) becomes Eq. (2.71), that is a combination of a pseudosinglet and a pseudotriplet.

In order to see how a state progresses through a system, we must express the state in terms of the eigenstates. Hence, this relation tells us that the singlet state evolves through the system as a superposition of a pseudosinglet and a pseudotriplet. Note that the pseudotriplet could strictly speaking not arise in the system described by the given Hamiltonian, as pseudospin is a conserved quantum number. By putting this system side-by-side with a superconductor however, we have production of singlet pairs in the superconductor. This production violates pseudospin conservation of the Cooper pairs in the system as a whole, and there will thus exist pseudotriplet pairs.

We have now managed to write the singlet state as a linear combination of the possible pairings of the single-particle eigenstates. As the eigenstates are stable, they may be used to get an intuitive picture of the physics. In order to form a wave function, we have to modify Eq. (2.71) slightly. In order for energy to be conserved when an s-wave singlet pair enters a ferromagnetic region, the momenta of the electrons have to shift so that both particles still lie at the same energy level. Hence, we know that in order for $\left|k_y,\uparrow'\right\rangle$ and $\left|k_y,\downarrow'\right\rangle$ to form a pair inside the F-region, we need to modify them to $\left|k_y^+,\uparrow'\right\rangle\left|-k_y^-,\downarrow'\right\rangle$, where $k_y^\pm=k_y+(\Delta k)^\pm$, which by definition gives the different pseudospin states equal energy. By using the notation $\left|k_y^\pm,\sigma'\right\rangle=\left|k_y,\sigma'\right\rangle e^{i(\Delta k)^\pm x}$, we can express the singlet pair wave function as

$$\psi_{\perp}(x) \sim \cos(\theta_{\mathrm{SO}}) \left\{ \left|k_y^+, \uparrow'\right\rangle \left|-k_y^-, \downarrow'\right\rangle e^{i[(\Delta k)^+ - (\Delta k)^-]x} - \left|k_y^-, \downarrow'\right\rangle \left|-k_y^+, \uparrow'\right\rangle e^{-i[(\Delta k)^+ - (\Delta k)^-]x} \right\} \\ - \sin(\theta_{\mathrm{SO}}) \left\{ \left|k_y^+, \uparrow'\right\rangle \left|-k_y^+, \uparrow'\right\rangle + \left|k_y^-, \downarrow'\right\rangle \left|-k_y^-, \downarrow'\right\rangle \right\}, \tag{2.72}$$

where the $\perp$-index denotes that the SOC-induced magnetic field is perpendicular to the magnetic field. This wave function contains one term with a non-zero CoM, and a term which has zero CoM. If the SOC-induced field and the magnetic field were parallel, the wavefunction would have become

$$\psi_{\parallel}(x) \sim \left|k_y^+, \uparrow'\right\rangle \left|-k_y^-, \downarrow'\right\rangle e^{i[(\Delta k)^+ - (\Delta k)^-]x} - \left|k_y^-, \downarrow'\right\rangle \left|-k_y^+, \uparrow'\right\rangle e^{-i[(\Delta k)^+ - (\Delta k)^-]x}. \tag{2.73}$$

The difference between $\psi_{\perp}$ and $\psi_{\parallel}$ is that $\psi_{\perp}$ is projected down on both pseudosinglets and pseudotriplets, while $\psi_{\parallel}$ is exclusively a pseudosinglet (in which case pseudospin simply reduces to spin, as spin becomes a good quantum number). The pseudosinglets have a non-zero CoM, giving them a relative phase difference which effectively breaks down the singlet pair correlation. This is conceptually similar to the proximity effect which occurs in clean ferromagnet-superconductor junctions. The pseudotriplets however are long-ranged, meaning they have no CoM, giving them no relative phase difference as they progress through the system. These pseudotriplets thus allows for long-ranged singlet pairs to exist in the system, and is a result of including SOC. Fig. 2.1 illustrates this difference between a clean F/S-structure (above) and an F/S-structure with SOC present in the F-region (below). The dispersion relations of the different pairings are illustrated to the right, which demonstrate that the pseudotriplets have no CoM, as opposed to (pseudo-)singlets.

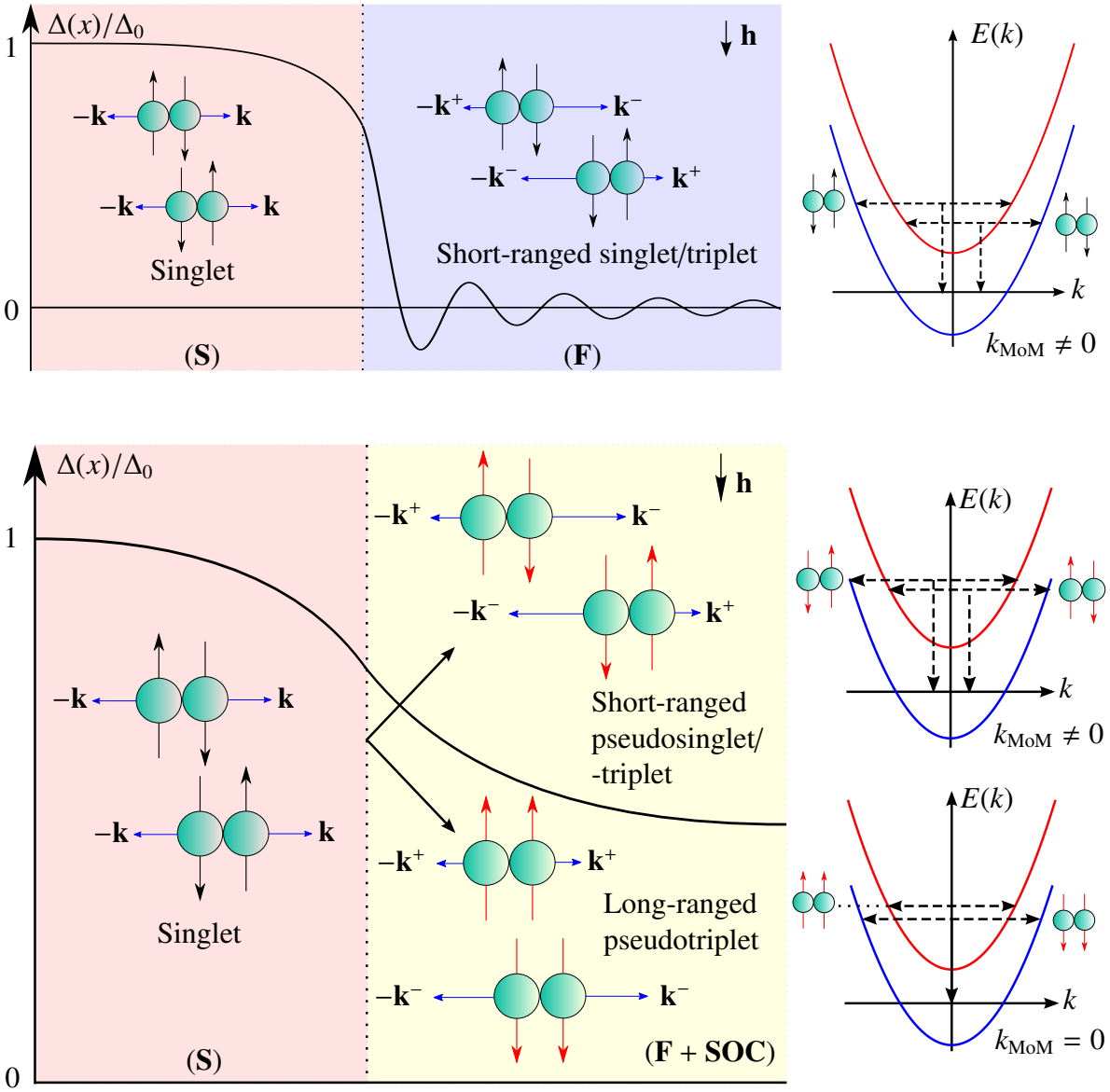

Figure 2.1: An illustration of the *s*-wave Cooper pairing in an F/S-structure (above), and in an F/S-structure with SOC in the F-region (below). Black arrows indicate spin, red arrows indicate pseudospin, while blue arrows indicate momenta. Singlet pairs are made in the S-region in both structures. As they enter the F-region of the clean F/S-structure, these pairs gain a non-zero center-of-mass momentum, k_{MoM}. This is illustrated by the plot to the right, where the dispersion relations of free electron states are plotted. It is evident that pairing between spin-up (red) and spin-down (blue) particles at the same energy level produces Cooper pairs with non-zero k_{MoM}. The different pairings really occur at the same energy level, but are illustrated at slightly different levels in order to make the figure more readable. The non-zero k_{MoM} causes a phase shift, which creates short-ranged triplets. This process also causes a non-zero triplet amplitude inside the S-region, but this is not explicitly shown in the figure. With inclusion of SOC, the same mechanism is present, only with pseudospin as eigenstates. However, some of the singlet pairs also progress through the F-region as long-ranged pseudotriplets. These have $k_{\mathrm{MoM}} = 0$, as illustrated by the plot of the dispersion relation to the right. As a consequence, a fraction of the singlet amplitude remains through the F-region, rather than dropping abruptly as in the clean F/S-structure.

The term “long-ranged” is usually used to describe triplet pairs. These are Cooper pairs of equal spin, where the spins are parallel to a magnetic field. Long-ranged triplet pairs have zero CoM inside the magnetic field, and are thus not broken down by a built-up relative phase, as singlets and ($s_z = 0$)-triplets most commonly are. The existence of such long-ranged Cooper triplet pairs effectively opens up a new channel of leakage from singlet pairs into triplet pairs, and thus usually lowers the critical temperature of a system. A simple analogy would be a bathtub of water in equilibrium, with a constant flow of water into the bathtub, and water draining out of it. Equilibrium in this sense means that the volume of water is constant, that is the inflow and outflow are equal. The water represents the singlet Cooper pairs, the constant inflow represents the creation of these in the superconductor, and the drainage represents the leakage into triplet pairs. By opening a new triplet channel, that is the long-ranged channel, it would effectively be as opening another plug, thus increasing the leakage. The system would react by stabilizing at a lower equilibrium, which means lowering the superconducting gap, giving a lower critical temperature.

By the term “long-ranged singlets”, we aim to describe singlets which gain no relative phase inside a magnetic field. Under normal circumstances, that is without SOC, these are conventionally not believed to exist. However, with the introduction of a magnetic field orthogonal to a SOC-induced magnetic field, we have proved that these in fact may exist, as the singlet state projected down on the eigenbasis reveals a non-zero component of a ($s' = \pm 1$)-pseudotriplet. Once again, we turn to the bathtub analogy for the interpretation. Where the existence of long-ranged triplets was equivalent to opening a new plug in the bathtub, long-ranged singlets represent in fact just the opposite. Since only a fraction of the singlet state experiences a phase shift, that is the part projected onto the eigenbasis as a pseudosinglet, this fraction is what remains of the first leakage channel. We thus effectively place a plug inside the first leakage which covers a fraction of the leakage equal to the fraction of a singlet state being a pseudotriplet. We have no second leakage, as there are no other channels converting singlet pairs into triplet pairs. This will affect the equilibrium such that the water level stabilizes at a higher level, and the superconducting energy gap will analogously increase. With a larger singlet amplitude, the critical temperature will be increased. Hence, a magnetic field perpendicular to a SOC-induced magnetic field should increase the critical temperature as compared to the configuration in which they are parallel. The bathtub analogy is illustrated in Fig. 2.2.

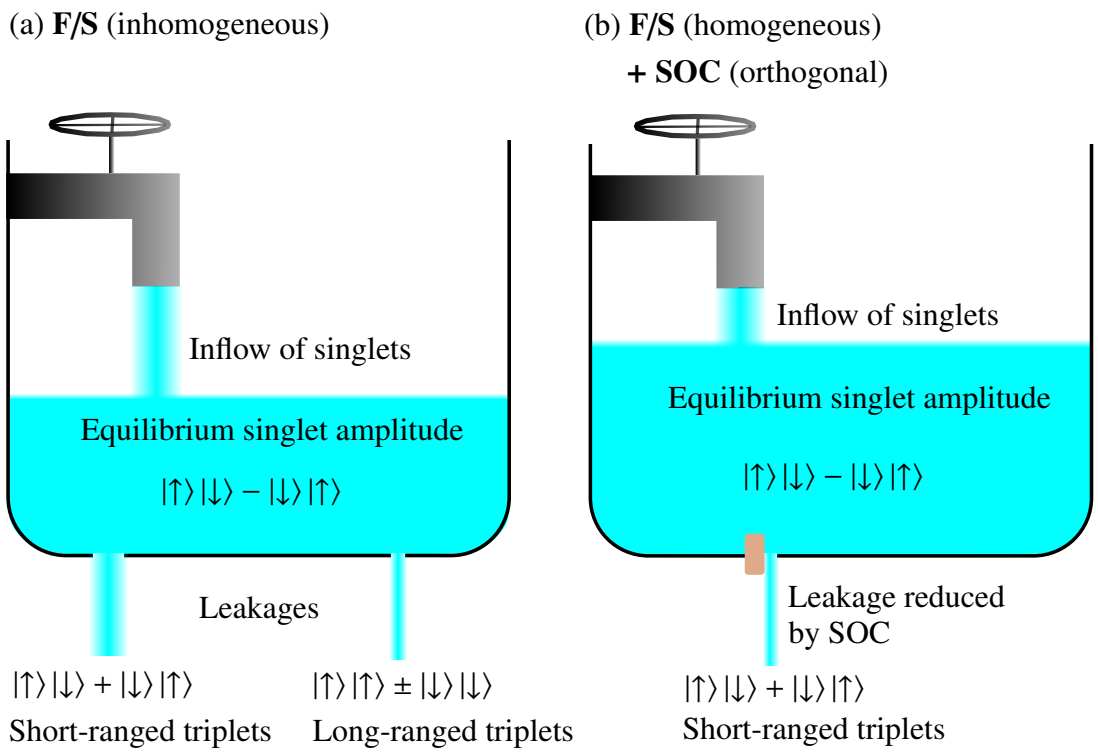

Figure 2.2: An illustration of the bathtub analogy presented in the text. The leftmost configuration (a) depicts the inhomogeneously magnetized F/S-structure. The leakages into the short-ranged and long-ranged channels will depend upon the magnetization setup. Note that we have named $|\uparrow\rangle|\uparrow\rangle \pm |\downarrow\rangle|\downarrow\rangle$ long-ranged states, but this strictly speaking only true inside a z-aligned magnetic field. The rightmost plot (b) depicts a homogeneously magnetized F/S-structure with SOC-induced fields orthogonal to the magnetic field. In this situation, only the $|\uparrow\rangle|\downarrow\rangle + |\downarrow\rangle|\uparrow\rangle$ channel is open, that is the short-ranged triplet channel. However, SOC has partly blocked the leakage, so that the total leakage is reduced. As a consequence of there being multiple leakages in (a), as well as the fact that the only channel of leakage is partly blocked in (b), the equilibrium stabilizes at a higher level in (b) than in (a).

Having discussed the behaviour of the singlet amplitude, we note that Eqs. (2.69) and (2.70) also implies the following relation for one of the ($s_z = \pm 1$)-triplets:

$$\begin{aligned}\left|k_y,\uparrow\right\rangle\left|-k_y,\uparrow\right\rangle + \left|k_y,\downarrow\right\rangle\left|-k_y,\downarrow\right\rangle = \cos(\theta_{\mathrm{SO}})\left[\left|k_y,\uparrow'\right\rangle\left|-k_y,\uparrow'\right\rangle + \left|k_y,\downarrow'\right\rangle\left|-k_y,\downarrow'\right\rangle\right] \\ + \sin(\theta_{\mathrm{SO}})\left[\left|k_y,\uparrow'\right\rangle\left|-k_y,\downarrow'\right\rangle - \left|k_y,\downarrow'\right\rangle\left|-k_y,\uparrow'\right\rangle\right].\end{aligned} \tag{2.74}$$

That is, this triplet projected onto the eigenbasis is also a linear combination of a pseudosinglet and a pseudotriplet. Without the presence of SOC, this triplet would have been a long-ranged triplet. However, after introducing SOC, it is evident that it rather becomes a superposition of a long-ranged and a short-ranged state, just as

the singlet state. With the Hamiltonian in Eq. (2.66), these triplet states are not certain to be produced. If this system was put side-by-side with another ferromagnetic region however, with magnetization in the y-direction, such triplets would generally have occurred. Strictly speaking, the pseudostates would not have been eigenstates of the entire system anymore, but they still serve as approximate eigenstates inside the first region. As both the s-wave singlet state and the s-wave ($s_z = \pm 1$)-triplet state are projected onto the eigenbasis as linear combinations of a pseudosinglet and a pseudotriplet, it could be argued that this would imply mixing between the singlet and the triplet state. That is, they seemingly progress through the system using the same pseudospin channels, and they may thus be mixed. However, the relative time coordinate on both sides of equations such as Eq. (2.74) must be equal. The appearance of both a non-zero singlet and triplet state within the same equation would involve either a singlet with $\tau \neq 0$ or a triplet with $\tau = 0$. This would violate the Pauli principle, and it is therefore required that either the singlet or triplet state in such an equation is zero. The singlet and triplet state therefore do not project onto the same pseudospin states, as they differ in the quantum number τ, and they are therefore not mixed by this effect. Note however that mixing between singlets and triplets is known to happen in ferromagnet-superconductor structures, and this analysis does not exclude this possibility. The analysis simply shows that spin-mixing between singlets and triplets due to the projection onto the eigenbasis cannot occur.

There are a couple of remarks which should be made before closing off this chapter. Firstly, in the previous chapter, we stated that $\mathbf{k}$-symmetry could be restored by letting $\psi(\mathbf{k}) \to \psi(\mathbf{k}) + \psi(-\mathbf{k})$. At first sight, this seems not to apply to the SOC-case, due to the $\mathbf{k}$-dependence of the SOC Hamiltonian. If the full singlet amplitude was written out, the sign before the $\sin(\theta_{\mathrm{SO}})$-terms in Eqs. (2.69) and (2.70) would have been changed for the $\psi(-k_y)$-terms, thus giving a minus sign in front of these components. The overall $\mathbf{k}$-symmetry is however restored by the fact that $\theta_{\mathrm{SO}} \to -\theta_{\mathrm{SO}}$ under the transformation $k_y \to -k_y$. Secondly, for simplicity, we have omitted any position dependence of the magnetic field and SOC. The pseudospin, and therefore the eigenstates, would in general have been dependent upon the spatial dependence of the terms in the Hamiltonian. The effect would likely be most prominent if the SOC-region and the ferromagnetic region were close. However, the qualitative effect would remain no matter the spatial distribution, namely that the singlet amplitude projected down on the eigenbasis would reveal a long-ranged pseudotriplet component, giving long-ranged behaviour to the singlet amplitude. One last remark is that although we have proved that the singlet state projected down on the eigenbasis contains a $\cos(\theta_{\mathrm{SO}})$-fraction of a pseudosinglet and a $\sin(\theta_{\mathrm{SO}})$-fraction of a pseudotriplet, this analysis does not tell us exactly how large the pseudosinglet and pseudotriplet amplitudes are. One must therefore go further in order to analyze the quantitative effect. This is just analogous to rotating the spin basis in the presence of a magnetic field, derived in Chapter 2.4.1, in which we considered how we could express the eigenstate pairings in terms of the s_z-states. The analysis did not tell us how whether or not the actual pairings existed, and if they did, how large the amplitudes were as function of the magnetic field strength.

2.4.3 Rotation in the presence of SOC and an arbitrary magnetic field

The above section covered the system configuration in which the magnetic field is orthogonal to the SOC-induced fields. Had we performed the complete calculation for an arbitrary magnetic field, the calculation would have become messy and complicated, as it involves a lot of tedious algebra. To put it briefly, the net magnetic field strength $\tilde{h}$ would have become become dependent upon the direction of $\mathbf{k}$, and as would all the other dimensionless quantities used to define the different field strengths relative to each other. Obtaining the full result is however not that important, as we are not able to use it to make an accurate quantitative prediction. A qualitative analysis is sufficient to capture the physics of it.

For a general magnetization, the pseudosinglet amplitude would have been a linear combination of a singlet, as well as all types of triplets, that is the ($s_z = 0$)- and both ($s_z = \pm 1$)-triplets. This can be generalized to apply for all the pseudotriplet amplitudes as well. The pseudosinglet and pseudotriplets all evolve differently inside the system we consider. Thus, if we project the pseudostates onto the spin-states at different positions in the system, they will in general give different results. This implies that there may be mixing between the spin-states. That is, the different kinds of triplets are being mixed. The Pauli principle still forbids such mixing between the singlet and triplet states, as discussed in the previous chapter. Mixing between the triplets of equal relative time τ is however allowed, and one would thus expect all triplet amplitudes to appear. This applies for all but two special magnetizations, namely the two configurations which were covered in the last section, with a magnetic field either parallel or orthogonal to the SOC-induced fields.

3 Methods

In this thesis we will look at two-dimensional systems comprised of *s*-wave superconductors, ferromagnets and normal metals. These kinds of systems have been studied for many years, and are well understood today. In this thesis however, we will also study how spin-orbit coupling affects these kinds of hybrid structures. In order to do so, we will use an approach in which we solve the Bogoliubov-de Gennes equations numerically. We use the solutions, which are the eigenstates of the system, to calculate important and characteristic results and observables. These include the superconducting gap parameter, triplet amplitudes, the critical temperature and local density of states (LDOS).

In this chapter, we will explain in detail the methods used for obtaining these results. What all methods have in common is that they require the solutions of the BdG equations. We will therefore start out by finding these solutions in Chapters 3.1-3.3, before we derive expressions for the other physical quantities in Chapters 3.4-3.6. This work requires both analytical as well as numerical analyses. The numerical steps are closely related to the analytical steps, and we will therefore give a full explanation of the numerical procedure in between all the analytical work. After reading this chapter, one should be able to reproduce the results given in Chapters 4-5.

All the methods which are presented in this chapter are inspired by a number of papers published by Klaus Halterman and co-authors, with the non-trivial exception of including SOC. These papers explain the methods to various degree, and no single paper sums up all of the methods. However, Refs. [33, 42–45] combined provide a solid platform for the implementation of these methods. The inclusion of SOC in this formalism is the main novel result of this thesis.

3.1 Hamiltonian

The general Hamiltonian for systems comprised of *s*-wave superconductors, ferromagnets and normal metals, with SOC, is

$$\begin{aligned} H = \sum_{\sigma} \int d\mathbf{r} \hat{\psi}^{\dagger}(\mathbf{r},\sigma)\Big[H_e + V(\mathbf{r}) - \mathbf{h}(\mathbf{r})\cdot\hat{\boldsymbol{\sigma}} + i\alpha_{\mathrm{R}}(\mathbf{r})(\hat{\boldsymbol{\sigma}}\times\hat{\mathbf{n}})\cdot\nabla\Big]\hat{\psi}(\mathbf{r},\sigma) \\ + \int d\mathbf{r}\Big\{\Delta^{*}(\mathbf{r})\hat{\psi}(\mathbf{r},\downarrow)\hat{\psi}(\mathbf{r},\uparrow) + \Delta(\mathbf{r})\hat{\psi}^{\dagger}(\mathbf{r},\uparrow)\hat{\psi}^{\dagger}(\mathbf{r},\downarrow)\Big\}. \end{aligned} \tag{3.1}$$

H_e is the kinetic term, $V(\mathbf{r})$ is the electric potential, $\mathbf{h}$ is the magnetic field, and $\alpha_{\mathrm{R}}(\mathbf{r})$ is the Rashba coupling constant. All of these physical quantities are thoroughly introduced and defined in Chapter 2. Note that it has been assumed that this SOC Hamiltonian is hermitian. If the position dependence of the Rashba parameter is such that

this Hamiltonian is non-hermitian, one must follow the symmetrization procedure presented in Chapter 2.3.4. If we furthermore use the SOC operators defined in Eq. (2.46) and the definitions in Eq. (2.55), that is the same notation as used in the BdG equations in Eq. (2.56), we obtain the BdG equations for the complete system:

$$\begin{pmatrix} H_e + V(\mathbf{r}) - h_z - h_{SO}^z & -h_x + ih_y - h_{SO}^x + ih_{SO}^y & 0 & \Delta \\ -h_x - ih_y - h_{SO}^x - ih_{SO}^y & H_e + V(\mathbf{r}) + h_z + h_{SO}^z & \Delta & 0 \\ 0 & \Delta^* & -(H_e^* + V(\mathbf{r}) - h_z + h_{SO}^z) & -h_x - ih_y + h_{SO}^x + ih_{SO}^y \\ \Delta^* & 0 & -h_x + ih_y + h_{SO}^x - ih_{SO}^y & -(H_e^* + V(\mathbf{r}) + h_z - h_{SO}^z) \end{pmatrix} \begin{pmatrix} u_{n,\uparrow}(\mathbf{r}) \\ u_{n,\downarrow}(\mathbf{r}) \\ v_{n,\uparrow}(\mathbf{r}) \\ v_{n,\downarrow}(\mathbf{r}) \end{pmatrix}$$
$$= E_n \begin{pmatrix} u_{n,\uparrow}(\mathbf{r}) \\ u_{n,\downarrow}(\mathbf{r}) \\ v_{n,\uparrow}(\mathbf{r}) \\ v_{n,\downarrow}(\mathbf{r}) \end{pmatrix}, \tag{3.2}$$

where n labels the energy eigenstates. To simplify the notation, we denote these energy eigenstates as $\psi_n(\mathbf{r}) = [u_{n,\uparrow}(\mathbf{r}), u_{n,\downarrow}(\mathbf{r}), v_{n,\uparrow}(\mathbf{r}), v_{n,\downarrow}(\mathbf{r})]^T$.

3.2 The BdG equations in Fourier space

We aim to solve the BdG equations in Fourier space. This is suited for a numerical approach, as we may adjust the accuracy of the calculation by changing the order of the expansions. Additionally, an energy cut-off will later justify the choice of an upper Fourier order.

Before we do the formal transition to Fourier space, we will define a few necessary system parameters, in addition to some notation which will make the derivations more tidy. The Fourier expansion firstly requires us to define the system dimensions. The system is two-dimensional, with infinite extent in the z-direction.[a] In other words, the system is translationally invariant in the z-direction. In the x-direction, $x = 0$ and $x = d$ define the outer boundaries of the system. As the system is two-dimensional, the system has no width in the y-direction. We use $\parallel$ to label quantities which are related to the x-direction, and $\perp$ for those related to the z-direction. For instance, the quantum numbers $\mathbf{k} = (k_\parallel, k_\perp)$ define a momentum state. Equivalently, we may also label the state with energy quantum numbers, $n \equiv (n_\parallel, n_\perp)$. Note that each energy state $E_\perp$ may have either $k_\perp$ or $-k_\perp$ as momentum quantum number if H is quadratic in $\mathbf{k}$, in which case there formally is a 2-to-1 correspondence between these labels. However, we define the purely symbolical quantum number n so that it describes non-degenerate energy states, keeping the one-to-one relation between the momentum and energy quantum numbers. That is, $k_\perp$ or $-k_\perp$ would have two different $n_\perp$.

An energy eigenstate of the system, $\psi_n(x)$, may in general a expressed as a superposition of free-particle momentum states.[46] More formally, we can express it as a Fourier series,

[a] The reason why the z-axis was chosen, instead of the more conventional y-axis, is only because it results in less needed CPU-time for the numerical calculations. This is due to that the "z-terms" end up in the diagonal of the BdG-matrix, which is beneficent for the algorithms used for finding the eigenvectors of the matrix. Additionally, the y-terms results in complex numbers in the BdG-matrix, giving complex eigenvectors, which requires twice the RAM. However, analytically speaking, the choice of axes is (of course) arbitrary, as no physical quantities depend upon this choice.

$$\psi_n(x) = \sqrt{\frac{2}{d}} \sum_{q=1}^{\infty} \hat{\psi}_{nq} \sin\Big(k_q x\Big), \tag{3.3}$$

where $k_q = q\pi/d$, and $\hat{\psi}_{nq} = [\hat{u}^{\uparrow}_{nq}, \hat{u}^{\downarrow}_{nq}, \hat{v}^{\uparrow}_{nq}, \hat{v}^{\downarrow}_{nq}]^{\mathrm{T}}$ are the Fourier components of the expansion. Note that we only care about the x-dependence of the wave functions, as the system is translationally invariant in the z-direction. With this definition, we have enforced the well suited boundary conditions $\psi_n = 0$ at $x = 0$ and $x = d$. By letting the kinetic term of the Hamiltonian act on $\psi_n(x)$, we obtain

$$H_e\psi_n(x) = \sqrt{\frac{2}{d}} \sum_{q=1}^{\infty} \left[\frac{\hbar^2}{2m}\Big(\frac{\pi q}{d}\Big)^2 + E_{\perp} - E_{\mathrm{F}} \right] \hat{\psi}_{nq} \sin\Big(k_q x\Big). \tag{3.4}$$

We have here defined the zero-point energy at the Fermi energy, E_{F}. We have furthermore defined $E_{\perp}$ as the kinetic energy contribution from the quantum number related to the z-direction, $n_{\perp}$. Note that $\psi_n(x)$ is an eigenstate of H_e only if there is one, and one only, contribution from the sum over q's, in which case ψ_n describes a free particle. Generally this is not the case, and we must solve the BdG equations in order to reveal the eigenstates. In order to obtain the BdG equations in Fourier space, we insert Eqs. (3.3) and (3.4) into the real space BdG equations in Eq. (3.5), as well as performing a Fourier transform on both sides by operating with $\int dx \sin\Big(k_{q'} x\Big)$, resulting in

$$\begin{pmatrix} \hat{H}_e + \hat{V} - \hat{h}_z - \hat{h}^z_{\mathrm{SO}} & -\hat{h}_x + i\hat{h}_y - \hat{h}^x_{\mathrm{SO}} + i\hat{h}^y_{\mathrm{SO}} & 0 & \hat{\Delta} \\ -\hat{h}_x - i\hat{h}_y - \hat{h}^x_{\mathrm{SO}} - i\hat{h}^y_{\mathrm{SO}} & \hat{H}_e + \hat{V} + \hat{h}_z + \hat{h}^z_{\mathrm{SO}} & \hat{\Delta} & 0 \\ 0 & \hat{\Delta}^* & -(\hat{H}^*_e + \hat{V} - \hat{h}_z + \hat{h}^z_{\mathrm{SO}}) & -\hat{h}_x - i\hat{h}_y + \hat{h}^x_{\mathrm{SO}} + i\hat{h}^y_{\mathrm{SO}} \\ \hat{\Delta}^* & 0 & -\hat{h}_x + i\hat{h}_y + \hat{h}^x_{\mathrm{SO}} - i\hat{h}^y_{\mathrm{SO}} & -(\hat{H}^*_e + \hat{V} + \hat{h}_z - \hat{h}^z_{\mathrm{SO}}) \end{pmatrix} \begin{pmatrix} \hat{u}^{\uparrow}_n \\ \hat{u}^{\downarrow}_n \\ \hat{v}^{\uparrow}_n \\ \hat{v}^{\downarrow}_n \end{pmatrix}$$
$$= E_n \begin{pmatrix} \hat{u}^{\uparrow}_n \\ \hat{u}^{\downarrow}_n \\ \hat{v}^{\uparrow}_n \\ \hat{v}^{\downarrow}_n \end{pmatrix}, \tag{3.5}$$

where we have defined $\hat{u}^{\sigma}_n = [\hat{u}^{\sigma}_{n1}, \hat{u}^{\sigma}_{n2}, \hat{u}^{\sigma}_{n3}, ...]$ and $\hat{v}^{\sigma}_n = [\hat{v}^{\sigma}_{n1}, \hat{v}^{\sigma}_{n2}, \hat{v}^{\sigma}_{n3}, ...]$, and the matrix elements

$$\hat{H}_e(q, q') = \frac{2}{d} \int_0^d dx \ \sin\Big(k_{q'} x\Big) \left[\frac{\hbar^2}{2m}\Big(\frac{\pi q}{d}\Big)^2 + E_{\perp} - E_{\mathrm{F}} \right] \sin\Big(k_q x\Big), \tag{3.6}$$

$$\hat{V}(q, q') = \frac{2}{d} \int_0^d dx \ \sin\Big(k_{q'} x\Big) V(x) \sin\Big(k_q x\Big), \tag{3.7}$$

$$\hat{\Delta}(q, q') = \frac{2}{d} \int_0^d dx \ \sin\Big(k_{q'} x\Big) \Delta(x) \sin\Big(k_q x\Big), \tag{3.8}$$

$$\hat{h}_i(q, q') = \frac{2}{d} \int_0^d dx \ \sin\Big(k_{q'} x\Big) h_i(x) \sin\Big(k_q x\Big), \quad i \in \{x, y, z\}, \tag{3.9}$$

$$\hat{h}^i_{\mathrm{SO}}(q,q') = \frac{2}{d}\int_0^d dx\ \sin\Big(k_{q'}x\Big)h^i_{\mathrm{SO}}(x)\sin\Big(k_q x\Big), \quad i \in \{x,y,z\}. \tag{3.10}$$

Note that while most of these integrals contain only scalar functions, $h^i_{\mathrm{SO}}(x)$ is general a differential operator. If it includes the k_x-operator, it converts a sine-function into a cosine, as well as giving a constant prefactor of $q\pi/d$.

The real space BdG equations have now been transformed into eigenvalue equations which determine the fourier components of the energy eigenstates of the system. Although Eq. (3.5) at first glance looks like a (4×4) matrix equation, one must keep in mind that $\hat{u}^\sigma_n$ and $\hat{v}^\sigma_n$ are vectors of length $N_{\max}$, where $N_{\max}$ is the highest Fourier order of the expansion in Eq. (3.3). Hence, the equation is in reality a much more intricate $(4N_{\max}\times 4N_{\max})$ matrix equation. Before introducing a cut-off order of the Fourier expansion, Eq. (3.5) thus represent a set of infinitely many equations. When such a cut-off is introduced however, we have a finite set of equations which is well suited for a numerical procedure.

3.3 The superconducting gap parameter

Before we can solve Eq. (3.5) numerically, we must resolve one issue, namely the fact that $\Delta(x)$ is undetermined. Determining $\Delta(x)$ is a non-trivial analytical task, and we therefore look for a method of doing this numerically as well. As it turns out, we can do this with a self-consistent approach which includes solving Eq. (3.5) iteratively, each time defining a new $\Delta(x)$ from the eigenvectors of Eq. (3.5), until $\Delta(x)$ converges.

If we insert the Bogoliubov transformations in Eq. (2.13) of the operators $\psi_\sigma(x)$ into the definition of $\Delta(x)$ in Eq. (2.2), using $\left\langle \gamma^\dagger_{\mathbf{k},\sigma}\gamma_{\mathbf{k}',\sigma'}\right\rangle = \delta_{\mathbf{k},\mathbf{k}'}\delta_{\sigma,\sigma'}f(E_{\mathbf{k}})$, where $f(E_{\mathbf{k}})$ is the Fermi-Dirac distribution, we obtain

$$\Delta(x) = \frac{V(x)}{2}\sum_{\mathbf{k}}\{1-2f(E_{\mathbf{k}})\}[u_{\mathbf{k},\uparrow}(x)v^*_{\mathbf{k},\downarrow}(x) + u_{\mathbf{k},\uparrow}(x)v^*_{\mathbf{k},\downarrow}(x)]. \tag{3.11}$$

We now switch to the n-labeling of the states introduced above. One conventionally defines the dimensionless coupling constant $\lambda(x) = V(x)D(0)$, where $D(0)$ is the density of states per area at the Fermi level. We insert the density of states per area in two dimensions, which is $D_2(0) = \frac{m}{\pi\hbar^2}$, as well as noting that we may rewrite $[1-2f(E_n)] = \tanh(E_n/2k_{\mathrm{B}}T)$. Hence Eq. (3.11) becomes

$$\Delta(x) = \lambda(x)\frac{E_{\mathrm{F}}}{4k_{\mathrm{F}}}\sum_n [u_{n,\uparrow}(x)v^*_{n,\downarrow}(x) + u_{n,\uparrow}(x)v^*_{n,\downarrow}(x)]\tanh(E_n/2k_{\mathrm{B}}T), \tag{3.12}$$

where we identify $u_{n,\sigma}$ and $v_{n,\sigma}$ as the components of the eigenstates defined by the real space BdG equations in Eq. (3.5). We have thus managed to express $\Delta(x)$ as a function of the eigenstates, which opens up for a self-consistent solution of the problem. By "guessing" an initial $\Delta(x)$, solving the Fourier space BdG equations, and use the solution to define a new $\Delta(x)$, repeatedly, one should hope to obtain a convergent solution which in that case would be the correct superconducting potential for the

given physical system. A natural guess would be a zeroth order approach in which we neglect any proximity effect in the system, thus initializing $\Delta(x)/\Delta_0 = 1$ inside the intrinsic superconductors, and set it to zero elsewhere. We have here introduced Δ_0, which is defined as the bulk value for the superconducting gap parameter inside an intrinsic superconductor.

Now that we have derived the qualitative approach of the numerical method, it follows naturally to comment more on the exact numerics. It has been shown that solving the BdG equations and finding a convergent self-consistent solution of $\Delta(x)$ is equivalent. We will therefore now explain in detail how to calculate $\Delta(x)$ numerically. All other physical quantities which is discussed later in this thesis are based on these same results, and thus also this method.

3.3.1 Introducing an energy cut-off

As discussed in Chapter 3.2, we need to reduce the BdG equations into a finite set of equations. In order to do so, we need a cut-off order for the Fourier expansions. Since the BCS theory assumes attractive electron-electron coupling only between electrons with energy on the interval $[E_\mathrm{F} - \hbar\omega_\mathrm{D}, E_\mathrm{F} + \hbar\omega_\mathrm{D}]$, where ω_D is the so-called Debye cut-off frequency, we may use this to derive a legitimate cut-off order for the Fourier expansions. The electron kinetic energy contribution from a plane wave in the x-direction is given by $\frac{\hbar^2}{2m}(\frac{\pi q}{d})^2$, where q is the Fourier order of the plane wave. Due to the energy coupling interval in the BCS theory, we may thus limit the maximal Fourier order in the calculation of Δ to $N_\mathrm{max} = \frac{\sqrt{2m}d}{\pi\hbar}\sqrt{E_F + \hbar\omega_\mathrm{D}}$. Moreover, we merely need to include $0 < E_\perp < (E_\mathrm{F} + \hbar\omega_\mathrm{D})$ as kinetic energy contribution from the z-direction.

By introducing the energy cut-off, we have therefore reduced the BdG equations into a finite $(4N_\mathrm{max} \times 4N_\mathrm{max})$ matrix equation. This simplification is sufficient for calculating the superconducting gap parameter, $\Delta(x)$. For other physical quantities which are not restricted by coupling on an energy interval, we may have to include higher Fourier orders. However, one can then use the self-consistent solution of $\Delta(x)$ obtained with the given N_max, and solve the BdG equations only once with a higher cut-off order, and then obtain a larger and more accurate set of eigenstates. It is however not necessary to do the self-consistent procedure all over again with a higher N_max, as $\Delta(x)$ only depends on those eigenstates below the cut-off.

3.3.2 Discretizing continuous variables

The self-consistent procedure involves using Eq. (3.12) for calculating a new $\Delta(x)$ after every iteration of solving the BdG equations. This step includes doing a sum over quantum states, or equivalently over energy levels, $\sum_n$, where $n = (n_\parallel, n_\perp)$. The energy levels of the kinetic energy contribution from the x-direction are discretized due to the finite system length, d. In the z-direction however, the energy levels are formally continuous, as the system is translationally invariant in this direction. The numerical procedure requires discretized energy levels, imposing the need for discretization of $E_\perp$. The sum over $n_\perp$ is really a (continuous) energy integral over the density of states times some function f, and we use the "rectangle rule" to approximate and discretize it:

$$\int_0^{E_F+\hbar\omega_D} dE_\perp D(E_\perp) f(E_\perp) \to (\Delta E) \sum_{i=0}^{N_\perp - 1} D(E_i) f(E_i), \tag{3.13}$$

where we defined the set of equally distributed energy levels, E_i, on the interval $[0, E_F + \hbar\omega_D]$ with spacing (ΔE). Note that this descretization works fine in two dimensions for all energies except $E = 0$, as the density of states in one dimension behaves as $\sim 1/\sqrt{E}$. To avoid dividing by zero, which of course causes numerical trouble, one should rather sum over the energy interval $[\delta_E, E_F + \hbar\omega_D]$, where δ_E is adjusted so that the integral approximation in (3.13) is fairly accurate. In this thesis, $\delta_E = (\Delta E)/4$ has been used.

Another continuous variable in the problem is the x-axis, which must simply be discretized into a set of equally distributed points with spacing (Δx). As for the energy levels, we choose the accuracy of the discretization so that it fits the required accuracy of the physical quantities. That is, we choose (Δx) and (ΔE) such that if we increase the accuracy, $(\Delta x) \to (1 - \delta)(\Delta x)$ and $(\Delta E) \to (1 - \delta)(\Delta E)$ for some $0 < \delta < 1$, the results remain invariant within the requirements of accuracy.[b]

3.3.3 Numerical procedure

After the BdG equations have been reduced to a finite set of equations, and the continuous variables have been discretized, the problem is prepared for the numerics. As discussed in the previous chapters, we start with an initial guess of $\Delta(x)$. From now on, let $\Delta(x)/\Delta_0 \to \Delta(x)$. With this notation, $\Delta(x)$ is dimensionless, and we presumably have $0 < \Delta(x) < 1$. Hence, we start with the initial guess that $\Delta(x) = 1$ inside the superconductors, and 0 elsewhere. Now solve the BdG equations in Eq. (3.5) with the Fourier cut-off order given in Chapter 3.3.1. The solutions will be energy eigenstates with corresponding energy eigenvalues, and use these to define a new $\Delta(x)$ from the formula in Eq. (3.12). Iterate this procedure until the solution is sufficiently convergent, that is until $\Delta(x)$ at no point along the x-axis changes more than some factor δ_Δ between each iteration. In this thesis, the calculations have been done for $\delta_\Delta = 10^{-3}$.

As these are full quantum mechanical calculations, the complexity quickly increases with increasing system dimensions. The requirements for computational power depend mainly on the choice of coherence length (ξ_0), Fermi wave vector (k_F), system dimensions and energy cut-off. In this thesis, we have used $k_F\xi_0 = 100$, and $\hbar\omega_D/E_F = 0.04$, and the programs were executed using MATLAB's Parallel Computing Toolbox, which is restricted to running on one computer node. With $N_\perp = 1000$, this limits the maximum system size to $d/\xi_0 \approx 3$ when executing the programs on one HPC node with an available RAM of 28 GB, before the inclusion of SOC. When SOC is included, the energy levels become fully non-degenerate, as $k_\perp$ and $-k_\perp$ generally gives different energy levels, and this requires even more RAM. The runtime is less of an obstacle for this computation, as solving the BdG equations for different $n_\perp$ is

[b] Increasing the discretization accuracy of the energy levels eventually causes problems, as the need for computational power increases roughly as $N_\perp^2$. This must also be accounted for when determining $N_\perp$.

suited for parallel computing. One HPC node had 16 available cores, usually resulting in a convergent solution of the superconducting pair potential in under an hour.

3.4 Pair amplitudes

In Chapter 2.1.3 we defined the pair amplitudes, $f_{\sigma\sigma'}$, which described the correlation between electrons with spin σ and σ'. If we use the definition of the pair amplitudes in Eqs. (2.20)-(2.23), and insert the Bogoliubov transformations of the operators from Eq. (2.13), we obtain rather straightforwardly

$$f_0(x) = \sum_n \left[u_{n,\uparrow}(x)v^*_{n,\downarrow}(x) + u_{n,\downarrow}(x)v^*_{n,\uparrow}(x)\right] \tanh\left(\frac{E_n}{2k_\mathrm{B}T}\right), \tag{3.14}$$

for the singlet amplitude. The triplet amplitudes becomes[47]

$$f_1(x,\tau) = \frac{1}{2}\sum_n \left[u_{n,\uparrow}(x)v^*_{n,\downarrow}(x) - u_{n,\downarrow}(x)v^*_{n,\uparrow}(x)\right]\zeta_n(\tau), \tag{3.15}$$

$$f_2(x,\tau) = -\frac{1}{2}\sum_n \left[u_{n,\uparrow}(x)v^*_{n,\uparrow}(x) + u_{n,\downarrow}(x)v^*_{n,\downarrow}(x)\right]\zeta_n(\tau), \tag{3.16}$$

$$f_3(x,\tau) = -\frac{1}{2}\sum_n \left[u_{n,\uparrow}(x)v^*_{n,\uparrow}(x) - u_{n,\downarrow}(x)v^*_{n,\downarrow}(x)\right]\zeta_n(\tau), \tag{3.17}$$

$$\tag{3.18}$$

where $\zeta_n(\tau)$ is defined as

$$\zeta_n(\tau) = \sin\left(\frac{E_n\tau}{\hbar}\right) - i\cos\left(\frac{E_n\tau}{\hbar}\right)\tanh\left(\frac{E_n}{2k_\mathrm{B}T}\right). \tag{3.19}$$

f_0 is normalized naturally between 0 and 1 by only dividing Δ with $\lambda(x)$. A suitable normalization scheme should also be used for the triplet amplitudes. We will however not focus on the exact numbers of these, but rather their relative amplitudes. In order to obtain a dimensionless relative time coordinate, we scale it up with the Debye frequency, that is $\tau \to \omega_\mathrm{D}\tau$. When referring to τ from now on, we implicitly refer to $\omega_\mathrm{D}\tau$.

We remind ourselves that these pair amplitudes do not depend on any cut-off energy, and we therefore have to include higher Fourier orders than N_max. As it turns out, f_0 is not sensitive to higher Fourier orders. We may therefore calculate f_0 only by dividing the superconducting gap parameter by the coupling constant, V, thus implicitly summing over all eigenstates within the cut-off interval. For the triplet amplitudes however, we need to include higher Fourier orders. An easy verification of the results is to check whether or not $f_i(x,0) = 0$ for all x and $i \in \{1, 2, 3\}$, as implied by the Pauli principle. If this is not the case, one must increase the applied cut-off levels for energies and momenta until this requirement is satisfied.

3.5 Local density of states

The local density of states (LDOS), $N(E, x)$, provides information on the distribution of states as a function of energy and position. Its interpretation is that $N(E, x)dE$ equals the number of quantum states within the infinitesimal energy interval $[E, E + dE]$ at position x.

We define the zero-point energy at the Fermi level. Hence, $E = 0$ is the point that separates particle and hole states in the ground state. When a particle is being excited, it "jumps" up above the Fermi surface, and leaves a hole below. The particle excitations are thus located at energies $E > 0$, while the hole excitations are found below the Fermi surface, at $E < 0$. The probabilistic nature of the wavefunctions implies that the local density of states can be expressed as[44]

$$N(E, x) = \sum_n \sum_\sigma \Big\{ |u_{n\sigma}(x)|^2 \delta(E - E_n) + |v_{n\sigma}(x)|^2 \delta(E + E_n) \Big\}, \tag{3.20}$$

where the δ-function is the Dirac-delta function. As all the energy levels are discretized, $N(E, x)$ will be a discrete distribution function. We want the density of states to be continuous, and in this thesis we solve this issue by performing a convolution with a Gaussian of width $0.02\Delta_0$. A proper choice of the width of the Gaussian ensures that the discrete points are being smoothed out into a continuous function, but without losing too much detailed information on the energy dependence. In this thesis, the LDOS is used as a tool to explore how superconductivity affects the configuration of electronic states compared to in a normal metal. We therefore normalize the LDOS to be 1 in the normal metal limit, and refer to this simply as the LDOS. The normal metal limit may be found in superconductors by evaluating $N(E, x)$ far from the Fermi level, that is several times Δ away from E_F.

3.6 Critical temperature

The critical temperature, T_c, of a system is defined as the temperature at which the electrons condense into the superconducting state and the system starts showing superconducting behaviour. This temperature can be thoroughly derived by finding the point where the condensation free energy of the system is zero, or in other words, the point where the free energy is the the same in the superconducting state as in the non-superconducting state. At this point, the electrons balance between favouring the superconducting and non-superconducting state. Finding this point requires an extensive numerical procedure with a high level of precision,[48,49] and will not be performed in this thesis. Instead, the critical temperature will be found by doing a perturbation expansion, treating the superconducting band gap, Δ, as a first order result, that is a small perturbation. By doing so we are implicitly assuming that the transition from the superconducting to non-superconducting state is a second-order phase transition.[50] Note that this method will not work for superconductors well within the type II regime, which cannot be accurately described by mean-field approximations due to phase fluctuations near the critical temperature. The method is briefly described in Refs. [43] and [45]. In order to get a full understanding of the method and the resulting formula for the critical temperature, we will derive it in detail here.

3.6.1 *Perturbation expansion to first order*

We start by defining particle-/hole-amplitude vectors

$$\mathbf{u}_n(x) = \begin{pmatrix} u_{n,\uparrow}(x) \\ u_{n,\downarrow}(x) \end{pmatrix}, \qquad \mathbf{v}_n(x) = \begin{pmatrix} v_{n,\uparrow}(x) \\ v_{n,\downarrow}(x) \end{pmatrix}, \tag{3.21}$$

and the matrices

$$\bar{H}_0 = \begin{pmatrix} H_e + V(x) & 0 \\ 0 & H_e + V(x) \end{pmatrix}, \qquad \bar{\Delta} = \mathbf{J}_2 \Delta\,, \tag{3.22}$$

where $\mathbf{J}_2$ is the (2×2) exchange matrix, sometimes also referred to as the backward identity matrix,

$$\mathbf{J}_2 = \begin{pmatrix} 0 & 1 \\ 1 & 0 \end{pmatrix}. \tag{3.23}$$

This matrix will also be of use later to express cross-coupling terms like $u_{n,\sigma} v_{n,-\sigma}$. Furthermore define $\boldsymbol{\sigma}$ as the vector of Pauli matrices, and a slightly altered vector of Pauli matrices $\tilde{\boldsymbol{\sigma}} = [-\sigma_x, \sigma_y, \sigma_z]$. By using this notation, the BdG equations take the form

$$\begin{pmatrix} \bar{H}_0 - \mathbf{h}\cdot\boldsymbol{\sigma} - \mathbf{h}_{\mathrm{SO}}\cdot\boldsymbol{\sigma} & \bar{\Delta} \\ \bar{\Delta}^* & -\left[\bar{H}_e - \mathbf{h}\cdot\tilde{\boldsymbol{\sigma}} + \mathbf{h}_{\mathrm{SO}}\cdot\tilde{\boldsymbol{\sigma}}\right] \end{pmatrix} \begin{pmatrix} \mathbf{u}_n \\ \mathbf{v}_n \end{pmatrix} = E_n \begin{pmatrix} \mathbf{u}_n \\ \mathbf{v}_n \end{pmatrix}, \tag{3.24}$$

where we remind ourselves that $\mathbf{h}_{\mathrm{SO}}$ is a momentum-dependent operator, while $\boldsymbol{\sigma}$ and $\tilde{\boldsymbol{\sigma}}$ act in spin space. We now do a perturbation expansion,[46,51]

$$\mathbf{u}_n = \mathbf{u}_n^{(0)} + \delta\mathbf{u}_n^{(1)} + O(\delta^2), \tag{3.25}$$
$$\mathbf{v}_n = \mathbf{v}_n^{(0)} + \delta\mathbf{v}_n^{(1)} + O(\delta^2), \tag{3.26}$$
$$E_n = E_n^{(0)} + \delta E_n^{(1)} + O(\delta^2), \tag{3.27}$$
$$\bar{\Delta} = 0 + \delta\bar{\Delta}^{(1)} + O(\delta^2), \tag{3.28}$$

where δ is an arbitrary perturbation parameter, which eventually will be set to 1. $\mathbf{u}_n^{(1)}$ is conventionally assumed to be an orthogonal function to $\mathbf{u}_n^{(0)}$, that is $\int_0^d dx \mathbf{u}_n^{(1)\dagger}(x)\mathbf{u}_n^{(0)}(x) = 0$, and $\mathbf{v}_n^{(1)}$ is likewise assumed to be orthogonal to $\mathbf{v}_n^{(0)}$. We have defined the superconducting band gap such that it first enters the equations at order $O(\delta)$. To zeroth order, Eq. (3.24) is diagonal, meaning $\mathbf{u}_n$ and $\mathbf{v}_n$ are completely decoupled. This implies that $\mathbf{u}_n^{(0)}$ and $\mathbf{v}_n^{(0)}$ have separate energy spectra, E_n^p and E_n^h respectively, where p and h denote particle and hole, and are found by solving the zeroth order BdG equations:

$$\left(\bar{H}_0 - \mathbf{h}\cdot\boldsymbol{\sigma} - \mathbf{h}_{\mathrm{SO}}\cdot\boldsymbol{\sigma}\right)\mathbf{u}_n^{(0)}(x) = E_n^p \mathbf{u}_n^{(0)}(x), \tag{3.29}$$
$$-\left(\bar{H}_0 - \mathbf{h}\cdot\tilde{\boldsymbol{\sigma}} + \mathbf{h}_{\mathrm{SO}}\cdot\tilde{\boldsymbol{\sigma}}\right)\mathbf{v}_n^{(0)}(x) = E_n^h \mathbf{v}_n^{(0)}(x). \tag{3.30}$$

To order first order, $O(\delta)$, the BdG equations read

$$\Big(\bar{H}_0 - \mathbf{h}\cdot\boldsymbol{\sigma} - \mathbf{h}_{\mathrm{SO}}\cdot\boldsymbol{\sigma}\Big)\mathbf{u}_n^{(1)} + \bar{\Delta}^{(1)}\mathbf{v}_n^{(0)} = E_n^{(1)}\mathbf{u}_n^{(0)} + E_n^{(0)}\mathbf{u}_n^{(1)}, \tag{3.31}$$

$$-\Big(\bar{H}_0 - \mathbf{h}\cdot\tilde{\boldsymbol{\sigma}} + \mathbf{h}_{\mathrm{SO}}\cdot\tilde{\boldsymbol{\sigma}}\Big)\mathbf{v}_n^{(1)} + \bar{\Delta}^{(1)*}\mathbf{u}_n^{(0)} = E_n^{(1)}\mathbf{v}_n^{(0)} + E_n^{(0)}\mathbf{v}_n^{(1)}. \tag{3.32}$$

Now operate on Eq. (3.31) with $\sum_{m_\parallel \neq n_\parallel}\int_0^d dx'\mathbf{u}_m^{(0)}(x)\mathbf{u}_m^{(0)\dagger}(x')$, and on Eq. (3.32) with $\sum_{m_\parallel \neq n_\parallel}\int_0^d dx'\mathbf{v}_m^{(0)}(x)\mathbf{v}_m^{(0)\dagger}(x')$. Use the orthogonality and completeness relations of $\mathbf{u}_n$ and $\mathbf{v}_n$, and the following formulas for the first order corrections are then obtained:

$$\mathbf{u}_n^{(1)}(x) = \sum_{m_\parallel \neq n_\parallel} \frac{\int_0^d dx'\mathbf{u}_m^{(0)\dagger}(x')\bar{\Delta}^{(1)}(x')\mathbf{v}_n^{(0)}(x')}{E_n^{(0)} - E_m^p}\mathbf{u}_m^{(0)}(x), \tag{3.33}$$

$$\mathbf{v}_n^{(1)}(x) = \sum_{m_\parallel \neq n_\parallel} \frac{\int_0^d dx'\mathbf{v}_m^{(0)\dagger}(x')\bar{\Delta}^{(1)*}(x')\mathbf{u}_n^{(0)}(x')}{E_n^{(0)} - E_m^h}\mathbf{v}_m^{(0)}(x), \tag{3.34}$$

where it is implied in the notation that the perpendicular energy quantum number is equal for all involved wave functions, that is $m_\perp = n_\perp$. The sum over $m_\parallel \neq n_\parallel$ is a sum over a complete set of one-dimensional eigenfunctions, with the exception of $m_\parallel = n_\parallel$, which is not included due to the assumption that the first order corrections are orthogonal to the zeroth order functions. Keep in mind that for the perturbation expansion to be valid, the fractions in Eqs. (3.33) and (3.34) have to be $\ll 1$.

We now want to derive an expression for the first order correction to $\Delta(x)$, that is $\Delta^{(1)}(x)$, by using the first order results for the wave functions. First expand $\Delta(x)$ in its Fourier components,

$$\Delta(x) = \sum_q \Delta_q \sin\Big(k_q x\Big), \tag{3.35}$$

where, as previously, $k_q = q\pi/d$. Equivalently, we may write

$$\Delta_l = \frac{2}{d}\int_0^d dx\Delta(x)\sin(k_l x). \tag{3.36}$$

$\Delta(x)$ is non-zero only inside intrinsic superconductors. Thus for a system in the x-direction with a non-superconducting region on the interval $[0, x_0)$, and a superconducting material on the interval $[x_0, d]$, we may also write

$$\Delta(x) = \Theta(x - x_0)\Delta(x) = \Theta(x - x_0)\sum_q \Delta_q \sin\Big(k_q x\Big), \tag{3.37}$$

where $\Theta(x - x_0)$ is the unit step function. It seems as though introducing this step function is unnecessary, but it will come of use quite soon. We now insert the definition of $\Delta(x)$, given in Eq. (3.12), into Eq. (3.36), and obtain

$$\Delta_l = \lambda\frac{E_{\mathrm{F}}}{2k_{\mathrm{F}}d}\sum_n \int_0^d dx\mathbf{v}_n^\dagger(x)\mathbf{J}_2\mathbf{u}_n(x)\sin(k_l x)\tanh(E_n/2k_{\mathrm{B}}T), \tag{3.38}$$

where $\mathbf{J}_2$ is the exchange matrix defined in Eq. (3.23). We now do a perturbation expansion of the Fourier coefficients of Δ. Since we are working to first order, we want to find $\Delta_l^{(1)}$, and $\Delta_l^{(0)} = 0$ by assumption. By inserting the perturbation expansion of Δ_l to first order on the left hand side, and the perturbation expansions of $\mathbf{u}_n$ and $\mathbf{v}_n$ in Eqs. (3.25) and (3.26) on the right hand side of Eq. (3.38), we obtain

$$\delta\Delta_l^{(1)} = \lambda\frac{E_\mathrm{F}}{2k_\mathrm{F}d}\sum_n\int_0^d dx\Big(\mathbf{v}_n^{(0)\dagger}(x)+\delta\mathbf{v}_n^{(1)\dagger}(x)\Big)\mathbf{J}_2\Big(\mathbf{u}_n^{(0)}(x)+\delta\mathbf{u}_n^{(1)}(x)\Big)\sin(k_l x)\tanh(E_n/2k_\mathrm{B}T). \tag{3.39}$$

We observe that there is no term of order $O(\delta^0)$ on either side of the equation, which is consistent. Now insert the first order results from Eqs. (3.33) and (3.34) into (3.39), expand $\mathbf{u}_n$ and $\mathbf{v}_n$ as in Eq. (3.3), and expand $\Delta^{(1)}(x)$ as in Eq. (3.37). We neglect the terms of order $O(\delta^2)$ which appear on the right hand side of the equation, and we get the following matrix equation

$$\Delta_l^{(1)} = \sum_k \mathbf{J}_{lk}(T)\Delta_k^{(1)}, \tag{3.40}$$

where the matrix elements $\mathbf{J}_{lk}$ are defined by the formula

$$\begin{aligned}\mathbf{J}_{lk}(T) = \lambda\frac{2E_\mathrm{F}}{k_\mathrm{F}d^3}\sum_n\sum_{m_\parallel}\sum_{p,q}K_{pql}\Bigg\{&\mathbf{v}_{mq}^{(0)\dagger}\mathbf{J}_2\mathbf{u}_{np}^{(0)}\frac{\sum_{i,j}\mathbf{u}_{ni}^{(0)\dagger}\mathbf{J}_2\mathbf{v}_{mj}^{(0)}K_{ijk}}{E_n^p-E_m^h}\tanh\left(\frac{E_n^p}{2k_BT}\right)\\ &+\mathbf{v}_{nq}^{(0)\dagger}\mathbf{J}_2\mathbf{u}_{mp}^{(0)}\frac{\sum_{i,j}\mathbf{u}_{mi}^{(0)\dagger}\mathbf{J}_2\mathbf{v}_{nj}^{(0)}K_{ijk}}{E_n^h-E_m^p}\tanh\left(\frac{E_n^h}{2k_BT}\right)\Bigg\}.\end{aligned} \tag{3.41}$$

To simplify notation, we have introduced $K_{ijk} = \int_0^d dx\Theta(x-x_0)\sin(k_i x)\sin\Big(k_j x\Big)\sin(k_k x)$. The sums over i, j, p and q go over the Fourier wave numbers. The constrained sum over n goes over the kinetic energy contributions from all directions. The sum over $m_\parallel$ goes over all kinetic energy contributions from the x-direction, with $m_\perp = n_\perp$ implied. We still keep in mind that the sum over $E_\perp$ really is an integral, since $E_\perp$ formally is a continuous variable.

Eq. (3.40) is a matrix eigenvalue equation. It has one obvious solution, the trivial solution, that is $\Delta(x) = 0$. This solution is of no particular interest, since it implies that superconductivity is absent. If we assume $\Delta(x) \neq 0$ however, the equation has a solution if and only if the matrix $\mathbf{J}(T)$ has an eigenvalue which is 1. Since superconductivity is sensitive to temperature, one should therefore expect only the trivial solution to remain if $T > T_\mathrm{c}$, where the critical temperature, T_c, is defined as the temperature at which superconductivity breaks down. This involves that all the eigenvalues of $\mathbf{J}(T)$ falls below 1. The critical temperature is therefore found by identifying at which temperature the largest eigenvalue of $\mathbf{J}(T)$ drops below 1.

3.6.2 Numerical procedure to find the critical temperature

In order to find the eigenvalues of the matrix $\mathbf{J}(T)$, we first have to do the same simplifications as was done when calculating the superconducting gap in Chapter 3.3. The

sum over the quantum numbers n originates from the definition of Δ, which means that we constrain the energy of the eigenstates to be on the interval $[E_\mathrm{F} - \hbar\omega_\mathrm{D}, E_\mathrm{F} + \hbar\omega_\mathrm{D}]$. This limits the highest Fourier order to N_max, as well as it limits $E_\perp$ to the interval $[0, E_\mathrm{F} + \hbar\omega_\mathrm{D}]$. The sum over $m_\parallel$ however originates from the sum over a complete set of states. As this in general means that we have to include all possible energies, we cannot constrain this sum to the same energy cut-off. However, it will turn out to be sufficiently accurate to constrain this sum to a few times the energy cut-off, that is $E_m \lessapprox 2E_\mathrm{F}$. The sums in Eq. (3.41) thus effectively reduce to

$$\sum_n \sum_{m_\parallel} \sum_{p,q} \sum_{i,j} \rightarrow \sum_n{}' \sum_{m_\parallel}{}'' \sum_{p,q}^{N_\mathrm{max}} \sum_{i,j}^{N_\mathrm{max}}, \tag{3.42}$$

where the prime denotes the energy constraint within the Debye cut-off energy, while the double prime denotes the aforementioned energy constraint $E_m \lessapprox 2E_\mathrm{F}$.

The problem has now been reduced to a solvable eigenvalue problem. One first has to find the zeroth order solutions $\mathbf{u}_n^{(0)}$ and $\mathbf{v}_n^{(0)}$ by solving the BdG equations with $\Delta = 0$ over the whole domain. These solutions are inserted into the definition of $\mathbf{J}$ in Eq. (3.41), and the task is now to find the temperature at which the largest eigenvalue drops below 1. A systematic procedure of doing so is by first calculating $\mathbf{J}(T_\mathrm{c}^0)$, where T_c^0 is defined as the critical temperature in a bulk superconductor. The eigenvalues of this matrix should presumably be 1 or less, as this defines the theoretical maximum temperature for a superconducting state to exist. If all eigenvalues are below 1, the temperature must be gradually reduced until the largest eigenvalue reaches 1 from below, at which point $T = T_\mathrm{c}$ to first order. If all eigenvalues of $\mathbf{J}$ are below 1 for all positive T, only the trivial solution remains, which implies that superconductivity is absent to first order.

Calculating T_c only requires solving the BdG equations once, at zeroth order, which reduces the complexity of the calculation as compared to calculating the superconducting gap parameter self-consistently. However, we may no longer restrict the Fourier order of the BdG equations to N_max, which greatly increases the complexity of the numerical procedure. As the number of necessary Fourier orders increase with the system size, this method therefore requires a substantial amount of computational power when applied on large systems. The method is based on a trial-and-error-approach when it comes to finding the correct T_c, and a new $\mathbf{J}$-matrix has to be calculated for every guess. The computational runtime may therefore be somewhat reduced by applying a clever guessing algorithm which converges towards the correct T_c in as few trials as possible. However, solving the BdG equations with a high cut-off order remains the most demanding operation, resulting in an extensive computational runtime.

4 Superconductors, metals and ferromagnets

The purpose of this chapter is to briefly review the proximity effect in two-dimensional systems comprised of superconductors (S), normal metals (N) and ferromagnets (F). These types of systems are already studied in great detail, for instance in numerous papers published by Klaus Halterman and co-authors, such as Refs. [33, 42–45], which have served as inspiration during the work with this thesis. These are however three-dimensional systems, where the system is translationally invariant in two directions. As this thesis treats two-dimensional systems, this chapter was included in order to add a complete set two-dimensional results to the thesis. These results will further be compared to the results obtained in Chapter 5, where SOC is included. The present chapter will also serve as a benchmark for the numerical framework developed herein, as we demonstrate that we are able to reproduce previously known results in the literature.

We start by gaining results for the most basic systems, namely those consisting of S, N or F, with maximum one junction. Towards the end of the chapter, we explore the F/S/F- and F/F/S-systems, which are of particular interest in creating long-range Cooper triplet pairs. All calculations in this chapter, as well as in Chapter 5, are made with a common set of physical constants, defined in Table 1.

Table 1: Definition of the system parameters for all calculations in Chapters 4 - 5.

System parameter	Definition
Coherence length	$k_{\mathrm{F}}\xi_0 = 100$
Debye cut-off	$\hbar\omega_{\mathrm{D}}/E_{\mathrm{F}} = 0.04$
Temperature	$T = 0$

The lengths of the systems considered will vary between the different structures, and the lengths will be specified explicitly in each section. d specifies the length of the entire system, while d_{S}, d_{N} and d_{F} denote the lengths of superconductors, normal metals and ferromagnets, respectively. If a system is comprised of several regions of the same type, they will be labeled with an additional number, for instance d_{F1}, d_{F2} etc., starting from the left of the system.

4.1 Normal metal

We start out with the simplest system, namely a system consisting of only a normal metal. Setting Δ to zero, we are simply left with a Hamiltonian of a two-dimensional

free electron gas. Such a system can easily be treated analytically, as the quasiparticle excitations reduce to those of electrons and holes. $d_N/\xi_0 = 2$ is used for all calculations, where ξ_0 is the coherence length of a superconductor with the parameters defined in Table 1.

4.1.1 Local density of states

The density of states as function of energy for a two-dimensional electron gas is a constant, assuming that the states are continuously distributed. Since the two-dimensional system considered here is translationally invariant along one axis, we should expect the energy levels to be continuously distributed, thus giving a constant density of states. The calculated normalized LDOS in the middle of the metal is plotted in Fig. 4.1, for two different energy discretizations. The LDOS is normalized to the mean value of the LDOS far away from the Fermi energy.

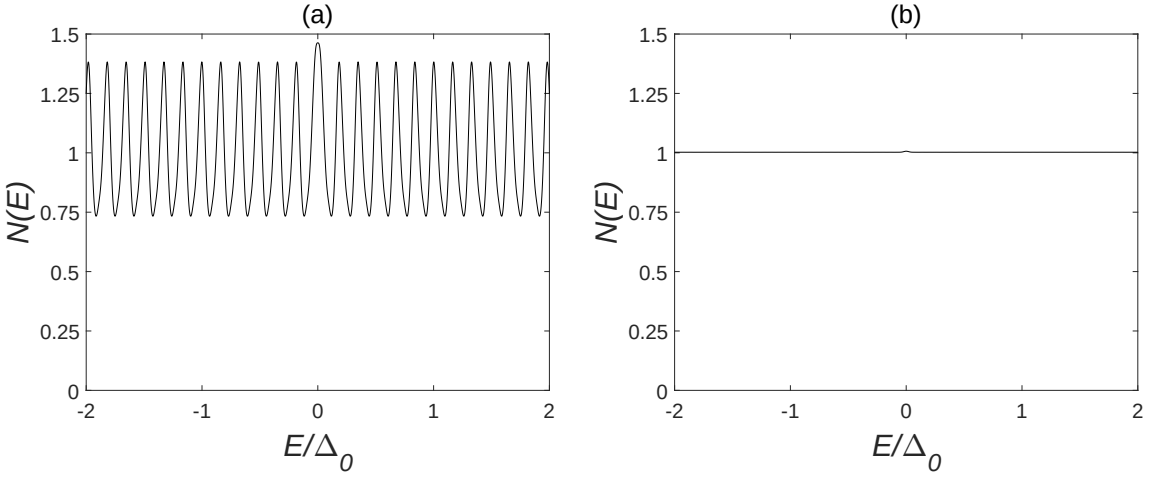

Figure 4.1: The local density of states at the center of a normal metal of $2\xi_0$, calculated for two different energy discretizations, $N_\perp$. (a) gives the LDOS with $N_\perp = 1000$, while (b) for $N_\perp = 8000$.

The results clearly confirms that the LDOS is fairly constant in the normal metal. That is, there are no energies at which there are distinct gaps. However, there are easily observable "oscillations" in Fig. 4.1(a). In addition, there is a prominent peak at $E = 0$. These irregularities occur due to the discretization of $E_\perp$, which is evident by comparing this plot with Fig 4.1(b), which is made with a discretization eight times finer than that of Fig. 4.1(a). The calculation with the finest discretization results in an almost perfectly constant LDOS. We therefore learn from Fig. 4.1 that these periodic oscillations of relatively small magnitude in the density of states do not necessarily represent a physical phenomenon, but is rather a result of the numerical approximation. We keep this result in mind when going further, and will therefore

not automatically interpret all irregularities in the LDOS as a physical result.[c] This non-physical, unwanted oscillatory behaviour of the LDOS is generally larger for two-dimensional calculations than in three dimensions. For instance, Ref. [42] finds that $N_\perp = 1000$ is a sufficiently accurate discretization, while this is clearly not the case for this two-dimensional calculation.

4.2 Bulk superconductor

After having explored the case of a pure metal, we follow up by considering a pure superconductor. In such a system, no other materials interfere with the superconducting properties of the system, that is there are no proximity effects present. Hence, we should be able to illustrate the predicted properties of a clean *s*-wave superconductor from the BCS theory. All results in this chapter have been obtained with $N_\perp = 1000$.

4.2.1 The superconducting gap

By the definition of Δ, which was normalized to 1 for bulk superconductors in Chapter 3.3, we expect Δ to be 1 in the center of the superconductor. At the boundaries however, Δ is forced to zero, and one should therefore expect oscillations close to the edges of the system. This is confirmed by a numerical calculation, of which results are illustrated in Fig. 4.2. Fig 4.2(a) depicts the results for a superconductor of two coherence lengths, that is $d_S/\xi_0 = 2$. In Fig 4.2(b), the system length is doubled, that is $d_S/\xi_0 = 4$.

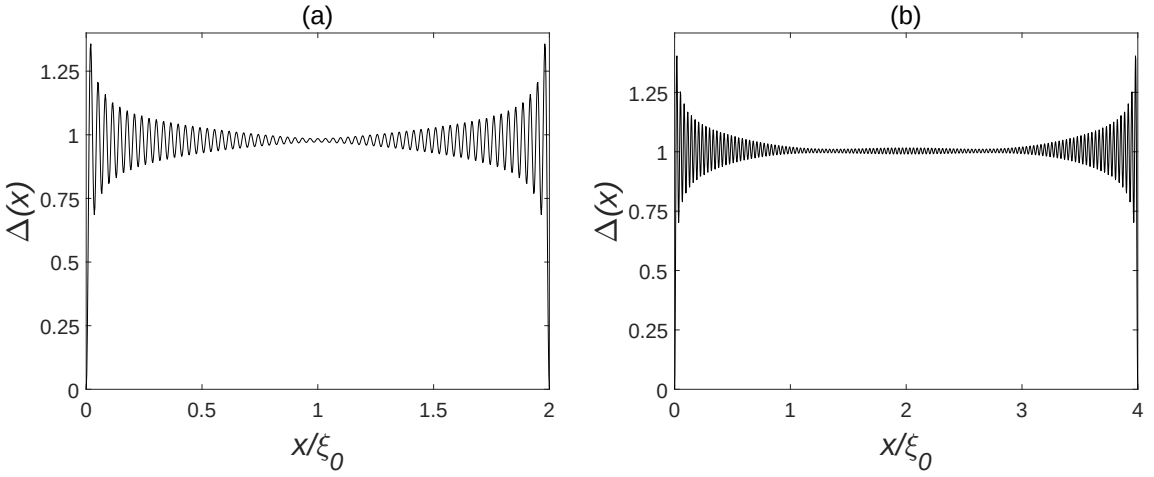

Figure 4.2: Plots of the superconducting gap parameter, $\Delta(x)$, in two bulk superconductors. The left plot (a) depicts a superconductor of $d_S/\xi_0 = 2$, while the length is doubled in the right plot (b), that is $d_S/\xi_0 = 4$.

[c] One could argue that one should use a sufficiently large $N_\perp$ so that these oscillations do not occur in all further calculations. However, this would require a lot of computational power, enabling only the smallest systems to be computed on one node on *Vilje* (the high performance computer at NTNU on which the calculations in this thesis are made). Moreover, other physical quantities are not this sensitive to the fine details of the energy spectrum.

Just as expected, Δ is approximately 1 inside the superconductor, apart from close to the edges. Near the edges of the system, oscillations occur, before the amplitude goes to exactly zero just at the edges. These oscillations are known as Friedel oscillations, and occur due to the sudden abruption of the electron density at the boundaries.[52] For the superconductor depicted in Fig. 4.2(a), which only has a length two times the coherence length, Δ is fairly constant equal to 1 only just in the center of the system. Besides this point, the oscillations are present throughout the entire domain. As coherence length is qualitatively defined as the length superconductivity requires to stabilize from the edges of a superconductor, it makes sense that Δ stabilizes to 1 after one coherence length in the results. This is moreover confirmed by Fig. 4.2(b), in which Δ also stabilizes at 1 approximately one coherence length into the system. This system is twice as long as the system considered first, and there is thus a region of about two coherence lengths inside the superconductor in which Δ has a fairly constant value of 1. It is evident that Friedel oscillations become increasingly dominant as the system is shortened. For systems shorter than two coherence lengths, the oscillations are expected to occur everywhere.

This system is a clean s-wave superconductor, hence there are no effects which may give rise to a triplet amplitude. Explicit calculations of the triplet amplitudes have been performed, and they confirmed that the triplet amplitudes are indeed exactly zero throughout the entire system for all relative times τ. This comes as no surprise, as this actually can be derived analytically for a clean superconductor due to the decoupling and symmetry of the BdG equations.

4.2.2 Local density of states

In the BCS theory, a band gap of width 2Δ is derived to occur at the Fermi level in the quasiparticle dispersion relation. Therefore, there are in fact no states allowed on the energy interval $E \in [E_\mathrm{F} - \Delta, E_\mathrm{F} + \Delta]$. The normalized LDOS has been calculated numerically for the two superconductors considered above in Fig. 4.2, and is plotted in Fig 4.3. Both plots depict the LDOS at $x = d_\mathrm{S}/2$, that is in the center of the systems. The LDOS is once again normalized to the mean of the LDOS far from the Fermi level.

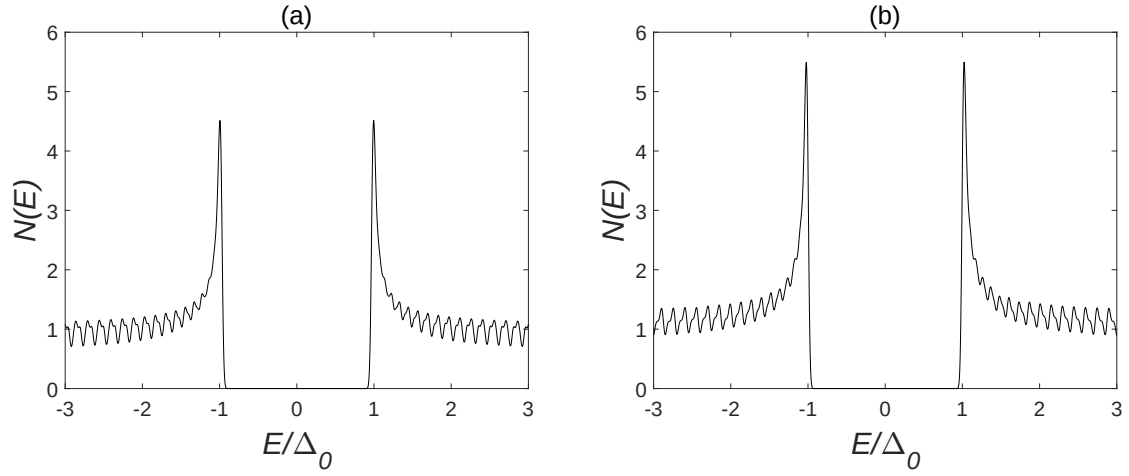

Figure 4.3: The local density of states at the center of two clean s-wave superconductors of different lengths. The left plot (a) depicts the results for a superconductor of length $d_S/\xi_0 = 2$, while the right one (b) depicts the results for a superconductor of length $d_S/\xi_0 = 4$.

The normalized LDOS confirms what the BCS theory predicts. Between $E/\Delta_0 = -1$ and $E/\Delta_0 = 1$, there are no allowed states. Just outside the band gap, there is a tiny interval with high density of states, and farther away from the band gap, the LDOS approaches 1. It seems as though the states which were inside the given energy interval before introducing superconductivity have now been pushed just outside it, resulting in a "crowded" area of states close to $E/\Delta_0 = \pm 1$. The states are however not pushed that far, and the results are rather equal to the LDOS for normal metals, depicted in Fig. 4.1, already at about $E/\Delta_0 = \pm 3$. The states far away from the Fermi level seem to be unaffected by superconductivity, which reflects that superconductivity is a phenomenon which happens at the Fermi level. It can moreover be observed that the plots are qualitatively equal, reflecting that the band gap does not depend on the superconductor's length, at least not when the length is above a certain lower threshold.

4.3 N/S-structure

Having covered both N- and S-structures separately, it is time to explore the effects of combining two such structures in an N/S-structure. The physical properties of such comprised structures will not simply behave as adding the properties from the two structures separately, but the different building blocks will influence each other, giving rise to the so-called proximity effects. The system considered in this chapter is defined by $d/\xi_0 = 2$, $d_N/\xi_0 = 0.2$, and $d_S/\xi_0 = 1.8$. The system thus has a length of two coherence lengths, and the superconductor spans 9/10 of it. We define $x/\xi_0 = 0$ to be at the junction. All results in this chapter have been obtained with $N_\perp = 1000$.

4.3.1 Δ and the pair amplitudes

Quite generally in quantum mechanics, wave functions are of trigonometric nature where they are classically allowed, while they drop off exponentially when they are

classically forbidden. Due to this brief analysis, we may expect the superconducting gap parameter to drop off in the N-region, as there is no interaction which creates and sustains Cooper pairs in this region. In order to fulfill the requirement of continuous derivatives of the wave functions, we must also expect Δ to drop off slightly near the interface. The result of an explicit numerical calculation of the superconducting gap is plotted in Fig. 4.4(a), while the singlet pair amplitude is plotted in 4.4(b).

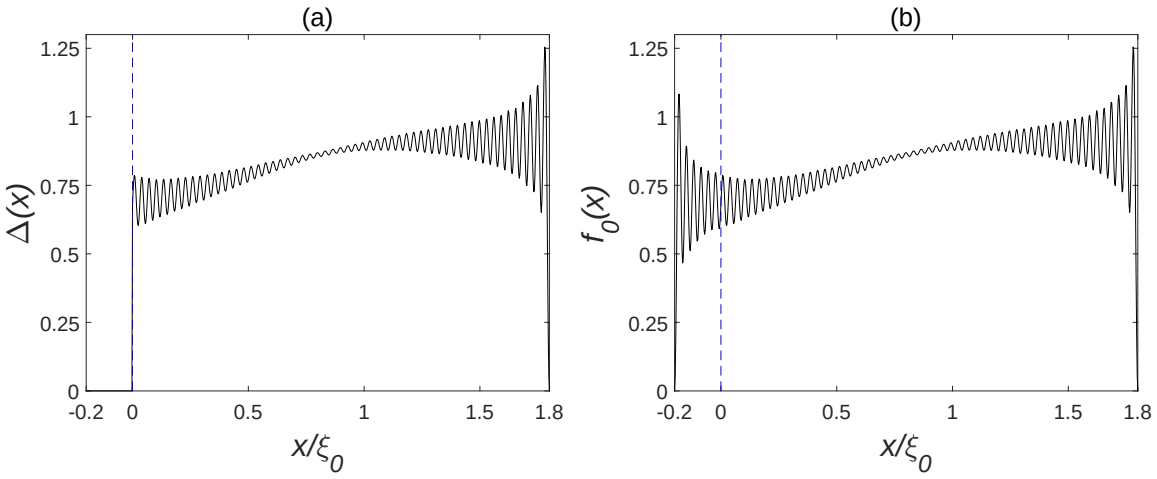

Figure 4.4: The superconducting gap parameter (a) and the singlet pair amplitude (b) for the N/S-structure. The dotted blue lines mark the junction between the N- and S-region.

The results more or less confirm our intuitive guess. Δ drops off in N, and rises towards approximately 0.9 inside S. Had we made the S-region narrower, we should expect that Δ would be furthermore suppressed. Eventually, when the region was too short to give rise to stable Cooper pair states, superconductivity would have broken down, defining a critical width of the S-region.[53] In the opposite case, in which we had made the S-region wider, we would expect Δ to stabilize closer to 1 in the regions far away from both the interface and the rightmost system edge. Using the aforementioned interpretation of the coherence length ξ_0, we would expect this limit to be $d_S \gg \xi_0$.

One may observe that the pair amplitude and Δ in this normalization regime only differs in the non-superconducting region. Since $f_0(x)$ contains all information, plotting $\Delta(x)$ as well is redundant, and from here on we will therefore only plot the singlet pair amplitude, $f_0(x)$.

As for the clean N- and S-structures, we still expect the triplet amplitudes to be exactly zero. The reason for this is that the BdG equations still decouple, resulting in an analytical zero-amplitude of the triplet pairs. Explicit numerical calculations confirm this, yielding that the triplet amplitudes are indeed zero everywhere.

4.3.2 Local density of states

The LDOS at four different positions inside the N/S-structure are plotted in Figure 4.5. One position is inside the metal, while the latter three positions are at different lengths into the superconductor.

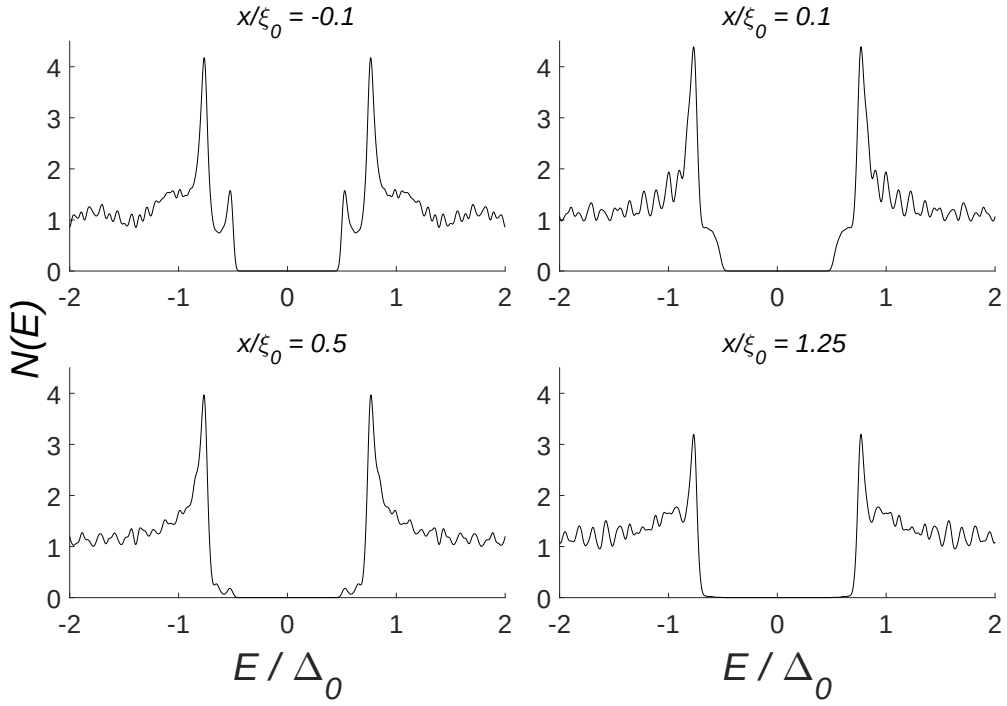

Figure 4.5: The LDOS at four different positions inside an N/S-structure. The upper left plot gives the density of states halfway inside the N-region, while the three other plots give the density of states at different positions inside the S-region. The positions are indicated on top of each plot. The results are obtained with $N_\perp = 1000$.

The plots illustrate nicely the proximity effects at an N/S-junction. Firstly, it is evident that the superconducting gap is narrower compared to that of a clean superconductor. The prominent peaks which mark the ends of the energy gap are now positioned at approximately $\pm 0.76\Delta_0$. Furthermore, close to junction, as well as inside the N-region, there is a small peak inside the energy gap. The resulting energy gap is now often referred to as the minigap,[54,55] and its presence inside the N-region is a visible consequence of the proximity effect. The peaks which mark the end of the minigap are most prominent inside the normal metal, but easily recognizable traces of them are evident also at $x/\xi_0 = 0.1$ and $x/\xi_0 = 0.5$. These peaks represent bound states, which arise due to Andreev reflection. Briefly, this is a process where a quasiparticle from the N-region are joined by another quasiparticle at the interface, entering the superconductor as a Cooper pair.[56,57] The second quasiparticle leaves a quasihole behind, which travels into the metallic side of the junction. Andreev reflection thus allows single particle states on the N-side with energies inside the energy gap to exist. These states drop off into the superconductor, where they are exponentially suppressed. There are however still traces of these a certain length into the S-region, as is evident in the LDOS plots.

4.4 F/S-structure

We now switch on a magnetic field inside the metal, turning it into a ferromagnet. Magnetic fields are known to break down Cooper pairs with zero spin projection parallel to the axis of the magnetic field, as the two electrons are treated differently in the magnetic field due to their anti-parallel spin alignment. Classically, one pictures that the magnetic field tries to align the two magnetic momenta, thus ripping the Cooper pair apart due to the imposed symmetry of the wave function. Quantum mechanically, the energy difference between the spin-↑- and spin-↓-particles results in pairing between electrons of slightly different momenta, giving them a non-zero center-of-mass momentum. This causes a phase shift which efficiently breaks down superconductivity. Additionally, magnetic fields induce surface currents on the superconductor. When the kinetic energy of such currents approaches the energy the electrons gain from forming Cooper pairs, Cooper pairs are no longer the preferred states (the superconducting state is no longer a minimum in the free energy). We thus expect magnetic fields to considerably suppress superconductivity.

The system parameters used in this chapter are the same as for the N/S-structure, but additionally we introduce a magnetic field $\mathbf{h} = h_0\hat{\mathbf{z}}$, with $h_0/E_\mathrm{F} = 0.3$.

4.4.1 Pair amplitudes

The singlet pair amplitude as a result of a self-consistent numerical calculation is plotted in Fig. 4.6, where the junction is positioned at $x/\xi_0 = 0$.

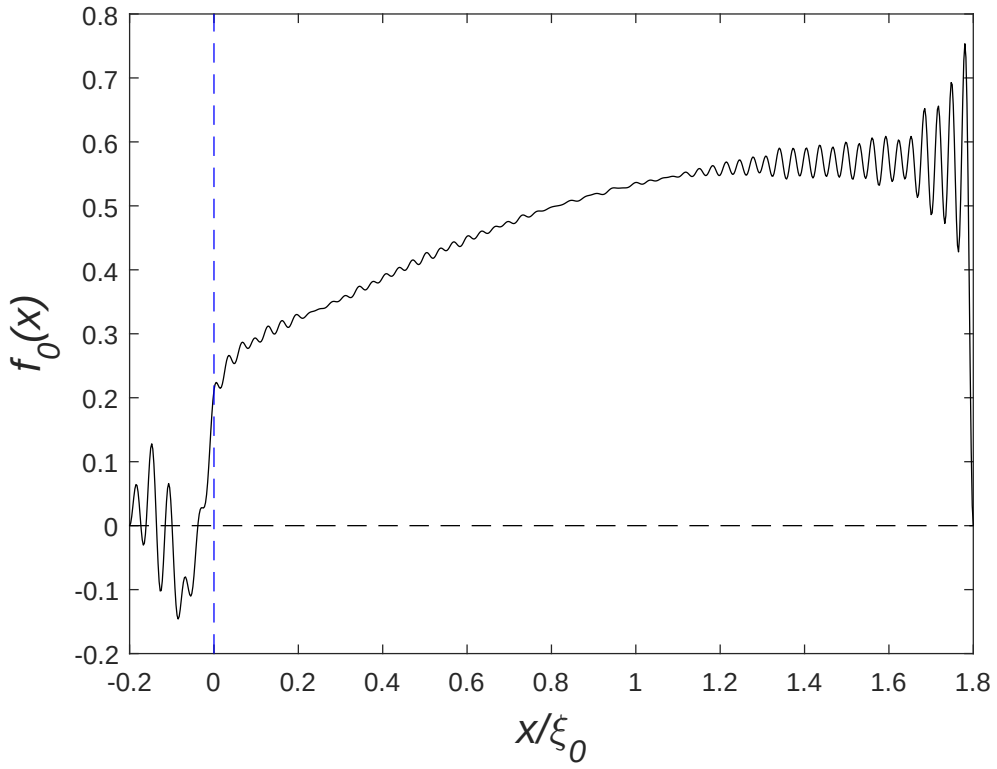

Figure 4.6: The singlet pair amplitude, f_0, plotted for an F/S-structure. The dotted blue line marks the junction between the two regions, with the F-region to the left and the S-region to the right.

The plot clearly shows that the superconducting gap parameter drops much faster in the F/S-system compared to that of the N/S-structure, in accordance with what we should expect from the discussion of the mixing of superconductivity and magnetic fields. Δ is moreover even more suppressed inside the S-region than in the N/S-structure, reaching only a fairly stable value of approximately $0.55\Delta_0$ before oscillations start at the edge. Approaching the junction from the right side, Δ drops rapidly very close to the junction. Continuing into the F-region, the pair amplitude oscillates around zero with a fairly low magnitude, and in what seems like an unsystematic manner. This effect can be understood from the fact that the spin-$\uparrow$ and spin-$\downarrow$ electrons gain different phases in the magnetic field, giving rise to oscillatory behaviour. Hence, from these results, it is evident that a magnetic field not only kills superconductivity efficiently inside the ferromagnetic region, but it also affects the conditions for superconductivity far inside the S-region.

The phase difference of the electrons gives rise to another meaningful coordinate for the Cooper pairs, namely the relative time, τ. The electrons may pair in spin-symmetric states if the total wavefunction is antisymmetric, and the introduction of the relative time enables us to place the anti-symmetry in τ, or equivalently, in frequency. This gives rise to so-called odd-frequency triplet Cooper pairs. The ($s_z = 0$)-triplet amplitude, f_1, is plotted in Fig. 4.7 for five different relative times τ.

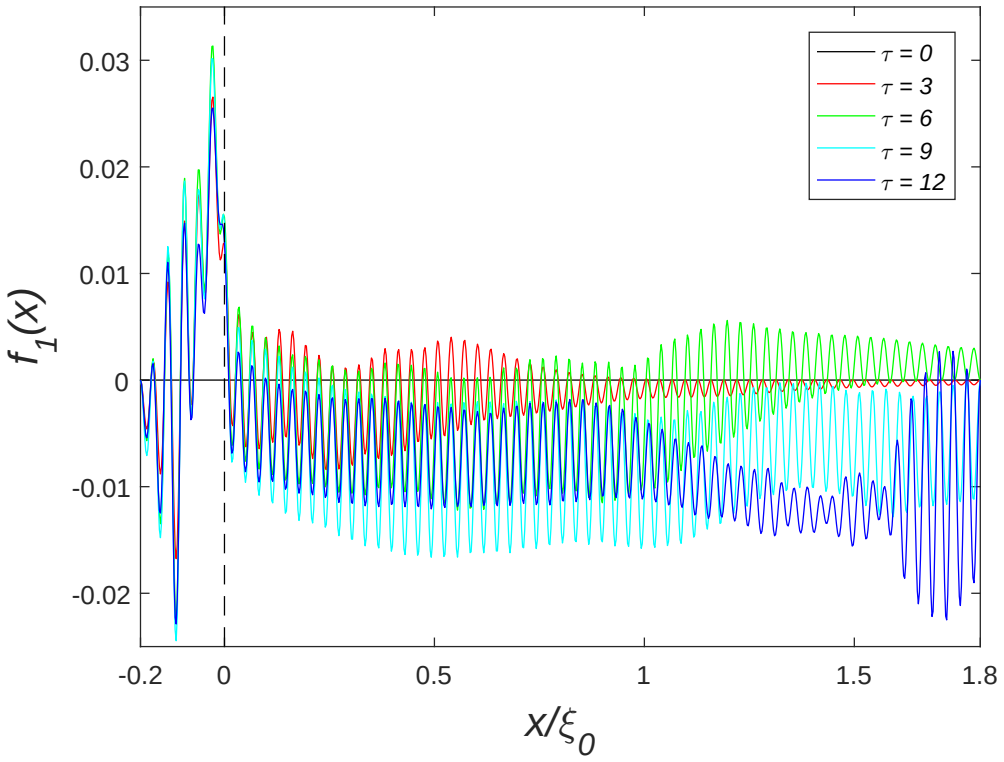

Figure 4.7: The triplet pair amplitude f_1 for the F/S-structure. The different colours indicate different relative times, τ, as explained by the legend. The dotted black line marks the junction between the F- and S-region.

We observe that the triplet amplitude is zero for $\tau = 0$, in accordance with the Pauli principle. For other relative times, it is clearly non-zero. Note the different behavior of the triplet amplitude inside the F-region as compared to inside the S-region. While the mean of the amplitude is fairy stable in the S-region, it varies extensively and unsystematically inside the F-region, just as we observed for the singlet amplitude. We can explain this from the fact that the ($s_z = 0$)-triplets, just as the singlets, have a non-zero center-of-mass momentum inside a magnetic field. This causes the aforementioned phase shift of the Cooper pairs, and as a consequence the amplitude becomes unstable in the F-region. In the S-region however, the triplets may live with a zero center-of-mass momentum, just as the singlets, causing a more stable amplitude.

The two remaining triplet amplitudes have been evaluated explicitly, and they are identically zero everywhere, as expected. This is a consistent result, as the Hamiltonian commutes with the z-component spin operator, σ_z. s_z is thus a conserved quantum number, forbidding the existence of an f_2- or f_3-amplitude.

4.4.2 LDOS

The LDOS at four different positions inside the F/S-structure is plotted in Fig. 4.8. The positions are equal to those used in the corresponding plot for the N/S-structure in Fig. 4.5.

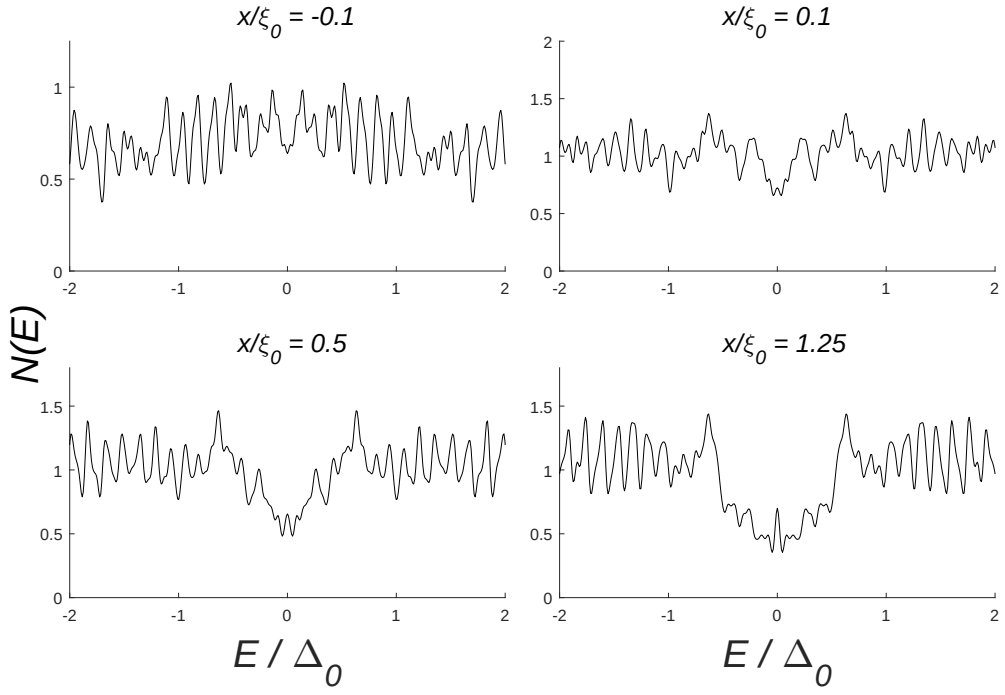

Figure 4.8: The LDOS plotted for the F/S-structure at four different positions. The upper left plot depicts the density of states at the center of the F-region, while the three remaining plots depict the density of states at different positions inside the S-region. The results are obtained with $N_\perp = 1000$.

It is apparent from the plots that the superconducting energy gap is in fact not fully developed at any position inside the structure. There are available states at all energies, clearly illustrating how magnetic fields suppress superconductivity. An energy gap is growing more prominent as one moves farther inside the superconductor, but it never evolves into a proper gap. An interesting observation is the peak at $E/\Delta_0 = 0$ which is clearly visible far inside the S-region. This peak is often an indication of the existence of triplet Cooper pairs.[58]

In the upper left plot, which is from inside the F-region, the density of states stabilizes at below 1 far from the Fermi level. This can be explained by the fact that the magnetic field favours one spin state, while the other spin state is equally suppressed. That is, one spin state experiences a potential well inside the magnetic field, while the other spin state experiences an equally strong potential barrier. In the limit of a very strong magnetic field, one should thus expect that the normalized density of states approaches 0.5 far from the Fermi level.

4.4.3 Critical temperature

In order to find out more explicitly how introducing a magnetic field affects the superconducting properties of the system, we plot the critical temperature as a function of the superconductors length, $T_c(d_S)$. The length of the ferromagnet is kept at a constant

$d_F/\xi_0 = 0.2$. The results from a numerical calculation is depicted in Fig. 4.9, for four different magnitudes of the magnetic field, including the limit of a normal metal.

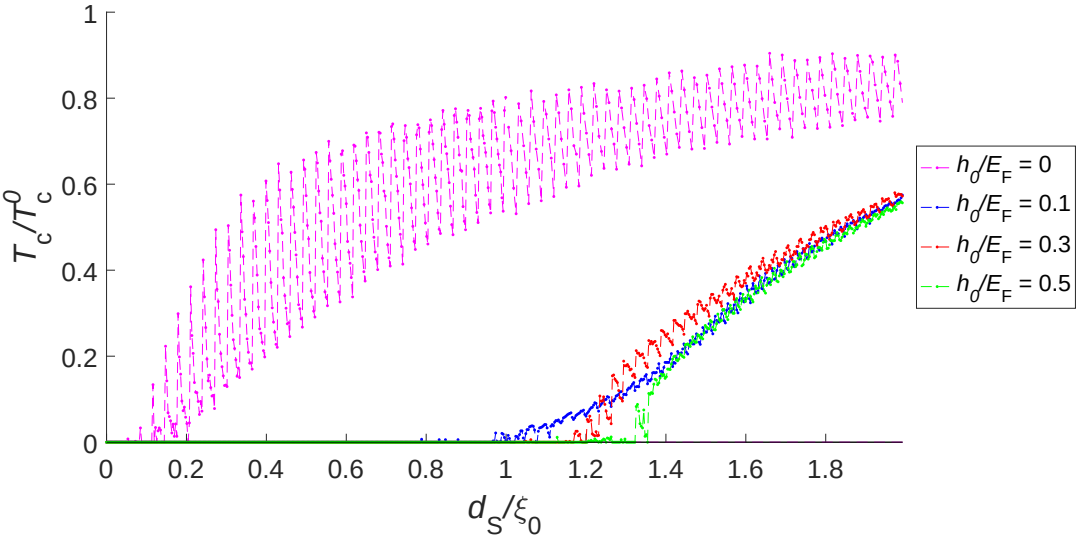

Figure 4.9: The critical temperature of the F/S-structure plotted with respect to the superconductor length, d_S, for four different magnetic field strengths. The critical temperature, T_c, is normalized to the temperature of a bulk superconductor with the same system dimensions, T_c^0.

In the normal metal limit, that is when $h_0 = 0$, one observes that superconductivity already appears at $d_S/\xi_0 \approx 0.1$. The critical temperature further shows a prominent oscillatory behaviour with respect to d_S. This behaviour can be explained by the symmetry of the wave function. Since Cooper pairs are formed by electrons at the Fermi level, we expect most of the electrons to have approximately the Fermi wave vector, k_F. Imagine now that we start with a specified system length d, and then increase or decrease the system size with (Δd). If we neglect any change in the proximity effect, the boundary behaviour of the wavefunctions will be more or less unaltered if we do this in half integer factors of the Fermi wavelength $2\pi/k_F$, resulting in approximately equal physical conditions. We may formulate this requirement mathematically as

$$\frac{(\Delta d)}{\xi_0} = \frac{\pi}{k_F \xi_0} \approx 1/32, \tag{4.1}$$

where we inserted $k_F\xi_0 = 100 \approx 32\pi$. Figure 4.9 confirms that the period of the oscillations is fairly accurately $\xi_0/32$, supporting this explanation. This derivation assumed no difference in proximity effect as we increase the system length, which generally is wrong. The consequence of this is that the local maxima of the critical temperature increases as we increase d_S, but we still manage to predict the period of the oscillations. In the limit of large d_S, the approximation of non-altered proximity effect is good, and we also observe in the figure that the mean amplitude flattens out as the superconductor reaches a certain length.

We now turn to the critical temperature where a magnetic field is present. The analysis is performed for $h_0/E_F = 0.1$, 0.3 and 0.5. As magnetic fields break down

superconductivity, the initial guess would be that stronger magnetic field implies more suppressed critical temperature. It can be observed that by increasing d_S, the first system in which superconductivity arises is indeed the one with the weakest magnetic field, when $d_S/\xi_0 \approx 1$. The next one to become superconducting is $h_0/E_F = 0.3$, and the system with the strongest magnetic field becomes superconducting first at $d_S/\xi_0 \approx 1.3$.

What might be surprising about this figure is that as d_S is being increased, the critical temperature of the system with $h_0/E_F = 0.3$ goes above the one with $h_0/E_F = 0.1$ at $d_S/\xi_0 \approx 1.3$. This seems to be somewhat in contradiction to the simplified statement that magnetic fields suppress superconductivity, as one would believe that stronger magnetic fields has a stronger impact. This therefore deserves a closer look. Below, in Fig. 4.10, the critical temperature in an S/F/S-structure is plotted with respect to magnetic field strength, h_0/E_F. The dimensions of the system are defined by $d_{S1}/\xi_0 = d_{S2}/\xi_0 = 1$, $d_F/\xi_0 = 0.2$. That is, both superconductors have a length of one coherence length, while the ferromagnet's length is $1/5$ coherence length. The blue line in Fig. 4.10 shows the results for a 2-dimensional system, while the red line shows the results for a 3-dimensional system. This analysis was performed for a trilayer- rather than a bilayer-structure as this leaves reflection at the system edges out of the analysis.

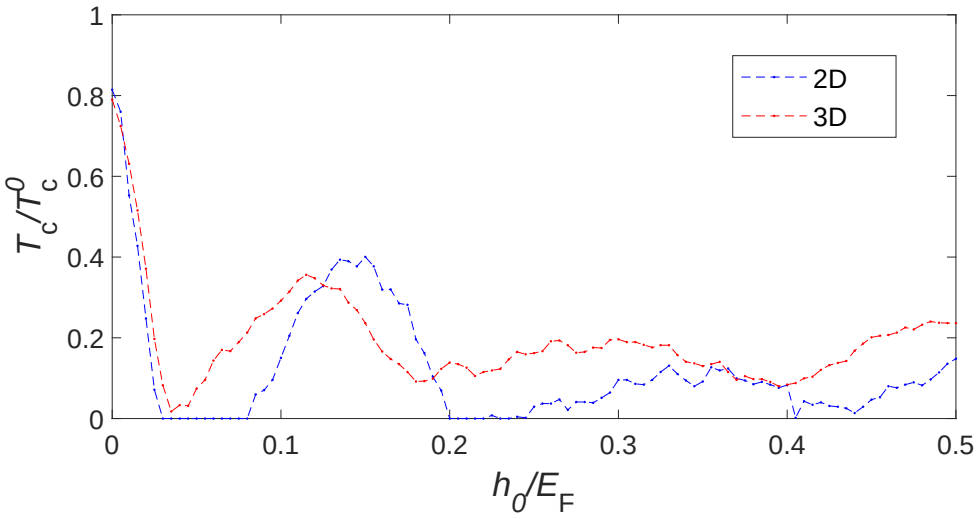

Figure 4.10: The critical temperature of an S/F/S-structure plotted with respect to the magnetic field strength, h_0. The blue line depicts the 2-dimensional result, while the red line shows the corresponding 3-dimensional result.

For both the 2-dimensional and 3-dimensional system, T_c oscillates with respect to h_0, which probably explains what we observed in Figure 4.9. That is, T_c is not a monotonic function with respect to h_0, and we should therefore in general not expect an increased magnetic field to result in a lower critical temperature. What is left to explain is what causes this seemingly periodic behaviour in T_c as function of the magnetic field strength, why the maxima and minima are placed where they are, and

why the oscillations are much more prominent in two dimensions compared to in three dimensions. To explain this, we need to do both a mathematical and a geometrical analysis.

First, we look at how a magnetic field impacts a quasiparticle wave function. Depending on whether the particle has spin-↑ or spin-↓, the particle either sees the magnetic field as a potential barrier or a potential well. From a classical perspective, the energy of the particle is raised or lowered with the Zeeman energy,[59] h_0, thus $E \to E \pm h_0$ inside the ferromagnetic region. The corresponding classical momentum would therefore go to $k \to \sqrt{2m/\hbar^2(E \pm h_0)} \equiv k^{\pm}$. Inside the ferromagnet, the momentum eigenstates will therefore transform approximately as

$$u_{k,\sigma} \sim e^{i(k+k^{\sigma})x} \equiv u_{\sigma}^{0} e^{ik^{\sigma}x}, \tag{4.2}$$

$$v_{k,\sigma}^{*} \sim e^{-i(k+k^{\sigma})x} \equiv v_{\sigma}^{0} e^{-ik^{\sigma}x}. \tag{4.3}$$

Each quasiparticle thus gains a phase. After the particles have traveled a distance d_{F} through the ferromagnet, the phase shift is $k^{\pm}d_{\mathrm{F}}$. The singlet pairs are formed by particles of approximately equal energy, and they thus transform as

$$f_0 \sim e^{-i(k^{+}-k^{-})d_{\mathrm{F}}} \left(u_{\uparrow}^{0} v_{\downarrow}^{0*} + e^{2i(k^{+}-k^{-})d_{\mathrm{F}}} u_{\downarrow}^{0} v_{\uparrow}^{0*} \right). \tag{4.4}$$

Observe that the singlet amplitude gains a phase. In Eq. (4.4) we have written this in terms of an overall phase as well as a relative phase between $u_{\uparrow}v_{\downarrow}$ and $u_{\downarrow}v_{\uparrow}$. If this relative phase, $\Delta\phi = 2(k^{+}-k^{-})d_{\mathrm{F}}$ evaluates to $(2n+1)\pi$, for some integer n, the singlet pair has in fact been transformed into a triplet pair. With the same argument, if the phase evaluates to $2n\pi$, the relative phase shift is zero, and the electron pair is still a singlet pair after having passed through the ferromagnet. One expects superconductivity to break down when a fair amount of all singlet Cooper pairs are converted into triplet pairs after passing through the ferromagnet. When all incoming singlet pairs exits the F-region still as singlet pairs, that is when the relative phase shift is minimal, one should expect superconductivity to be preserved. The particles forming Cooper pairs are found approximately at the Fermi level, and the equation for finding the maxima and minima of the critical temperature therefore becomes

$$\sqrt{1+I} - \sqrt{1-I} = \begin{cases} \frac{(2n+1)\pi}{2k_{\mathrm{F}}d_{\mathrm{F}}} & \text{(minima)} \\ \frac{2n\pi}{2k_{\mathrm{F}}d_{\mathrm{F}}} & \text{(maxima)} \end{cases} \tag{4.5}$$

where we have defined $I = h_0/E_{\mathrm{F}}$. Solving this equation yields minima at $I_{\min} \in \{0.08,\ 0.23,\ 0.39\ ...\}$ and maxima at $I_{\max} \in \{0,\ 0.157,\ 0.310,\ 0.457\ ...\}$, which is in good correspondance with what we observed in Fig. 4.10. If we focus on the two-dimensional case, it is evident that the first few minima and maxima fits the model well, while for higher I, there is a slight deviation, and the maxima and minima become less prominent. One must remember that a lot of classical approximations have been done in the derivation, as well as setting $E = E_{\mathrm{F}}$, which in fact deviates with $\pm\hbar\omega_{\mathrm{D}}$. These approximations are probably the reason to why the model misses of increasing magnitude as we turn to larger I. We have however managed to predict

where the first few maxima and minima appear, and have thus probably understood the physics behind the phenomenon.

What is now left to answer is why this effect is stronger in two dimensions than in three. In arriving at that answer, we must first reveal a flaw in the previous argument. We considered only electrons moving perpendicularly to the junctions between the superconductors and the ferromagnet. However, in systems spanning more than one dimension, we also have electrons at the Fermi level moving in other directions, carrying kinetic energy from movement in the directions parallel to the junction plane. Therefore, although the strictly perpendicular-moving electrons experience a special phase shift at the solutions of Eq. (4.5), electrons from all other directions do not share this symmetry, and will thus cancel the full effect. We name these other electrons "interfering" electrons.

We will now show that this full effect indeed happens in a two-dimensional free electron gas. The plane of intersection between the ferromagnetic and superconducting regions in two dimensions correspond to a one-dimensional line. Say we define a point p_0 somewhere along this line. From this point, an electron from a singlet Cooper pair, e_0, travels into the ferromagnetic region, perpendicular to the plane of intersection, eventually hitting the other superconducting side at point p_s. The phase shift argument above applies for this electron, and for certain magnetic field strengths the electron will exit the F-region as part of a singlet Cooper pair. Along this same line there exist exactly two points which are positioned at any specified distance, d_1, from the first point p_0. There is one such point at each side of p_0. For simplicity, we will now only consider one of these sides, but the analysis applies for both sides. We refer to this point as p_1. From this point, there exists exactly one trajectory on which a (classical) electron may travel in order to hit the point p_s. We name this electron e_1, and this electron will in general interfere with the effect discussed above. However, for each interfering electron, e_1, there exists another electron, e_2, traveling from point p_2 a distance $d_2 > d_1$ from p_0, hitting the exact same point p_s, with exactly opposite phase of e_1. Thus the wavefunction of e_2 cancels the wavefunction of e_1 at point p_s, and the interfering effect therefore vanishes. This argument can be applied to all positions along the intersecting line, with the exception of point p_0. As the electrons in a two-dimensional electron gas is evenly distributed with respect to the direction of $\mathbf{k}$, the interfering effect will cancel exactly. The electrons which do not move perpendicularly to the interface do therefore not interfere with the effect discussed above, causing the effect to take place in two dimensions.

In three dimensions however, the number of points at distances d_i from p_0 grows proportionally to d_i. As a consequence, the interfering electrons will not add up in perfect cancellation. The total breakdown of superconductivity for certain magnetic field strengths, as happens in two dimensions, does therefore generally not occur in three dimensions. The effect is however still easily visible in three dimensions, as T_c has local (non-zero) minima and maxima approximately where they are predicted by Eq. (4.5), proving that some symmetry remains.

4.5 Long-range triplet pairs

We have now covered both N- and S-systems, as well as N/S- and F/S-structures. We observed that triplet pairs occurred in the F/S-structure, while they were absent for all other systems. However, only the ($s_z = 0$)-Cooper pairs occurred. Their penetration depth in a ferromagnet with magnetic field orientation in the z-direction is short, as the discussion of pair breaking due to non-zero center-of-mass momentum in ferromagnets applies generally for all ($s_z = 0$)-pairs. In order to obtain long-range Cooper pairs, we need to construct Cooper pairs of which both electrons are treated equally by the magnetic field, that is with equal spin projection along the axis of the magnetic field. There are two system compositions which are of special interest for this purpose, namely the F/S/F- and F/F/S-structures.[60,61] These systems have magnetic fields in two separate regions, which we allow to have different directions. When the magnetic fields are not parallel, σ_z no longer commutes with the Hamiltonian, and the ($s_z = \pm 1$)-Cooper pairs are allowed to form. When these enter the region with a z-aligned magnetic field, they will be long-ranged. This effect applies more generally to all inhomogeneously magnetized structures.

In this chapter, we will investigate the F/S/F- and F/F/S-structures in two dimensions. Unless otherwise specified, we set the length of the two ferromagnetic regions to $d_{\mathrm{F1}}/\xi_0 = d_{\mathrm{F2}}/\xi_0 = 0.2$, the length of the superconductor to $d_{\mathrm{S}}/\xi_0 = 3$, and the magnetic field strength to $h_0/E_{\mathrm{F}} = 0.3$. For both systems, we also define the relative magnetic field alignment θ_h, which is the angle between the magnetic fields in F1 and F2, $\mathbf{h}_1$ and $\mathbf{h}_2$ respectively.

4.5.1 F/S/F-structure

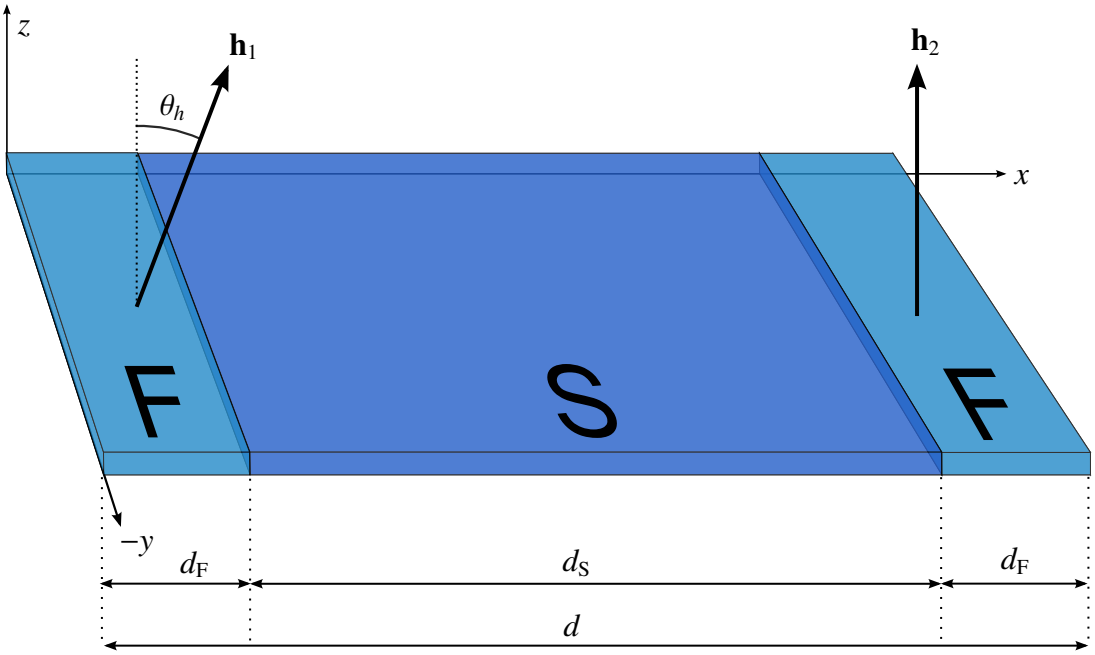

Figure 4.11: An illustration of the F/S/F-structure. The system considered is in reality not of restricted length along the y-axis, but is of infinite extent in this direction. Moreover, the structure is of no extent in the z-direction.

We first consider the F/S/F-structure, which is sketched in Fig. 4.11. The singlet correlation function $f_0(x)$ is plotted in Fig. 4.12, for $\theta_h = 0$.

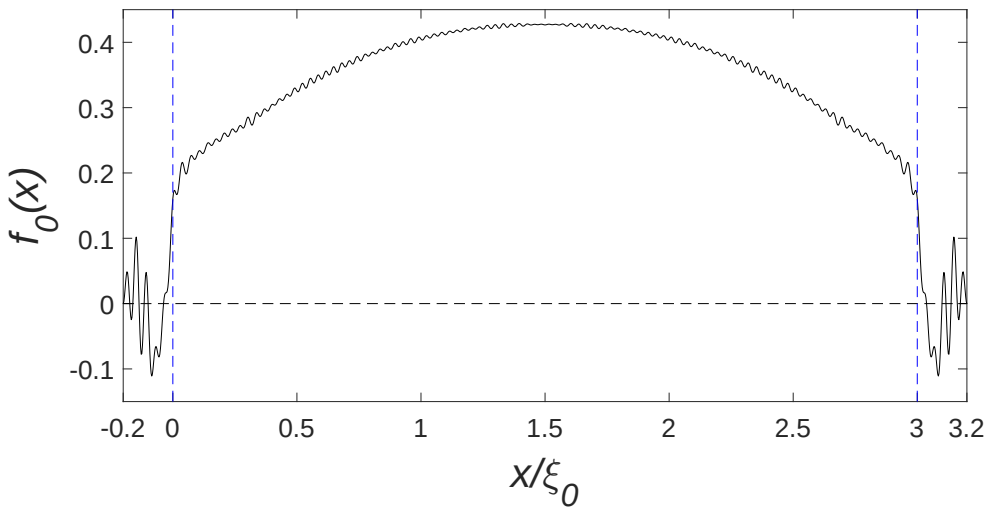

Figure 4.12: The singlet amplitude f_0 plotted for the F/S/F-structure with $\theta_h = 0$. The amplitudes for the other relative magnetization angles are qualitatively more or less equal to this, and are thus not plotted. The dotted blue lines mark the junctions between the three regions.

The singlet amplitude behaves as one would expect after having explored the F/S-junction, as the same kind of proximity effect finds place at each end. Note however how suppressed the pair amplitude is compared to the F/S-case in Fig. 4.6. Keep in mind that the superconductor in this system is three coherence lengths, that is three times the length of the F/S-structure. This clearly indicates that having a ferromagnet at each side greatly weakens superconductivity, and the superconductor must be large in order for superconductivity to arise. Explicit numerical calculations have been performed for $d_S = 2$, which in fact resulted in $\Delta = 0$ for all x at $T = 0$ and $\theta = 0$. For the system with $d_S/\xi_0 = 3$, the pair amplitude is qualitatively fairly equal for other values of θ_h. However, it grows slightly when increasing θ_h, and its peak value has grown about $0.08\Delta_0$ when reaching $\theta_h = \pi$, where the fields are antiparallel.

In Fig. 4.13, two triplet amplitudes, f_1 and f_2, are plotted for five different magnetic field alignments, $\theta_h \in \{0, \pi/4, \pi/2, 3\pi/4, \pi\}$, for five different values of the relative time coordinate, τ, as indicated by the figure legend. The remaining triplet amplitude, f_3, is zero for all θ_h and τ, and has therefore been left out from the further analysis.

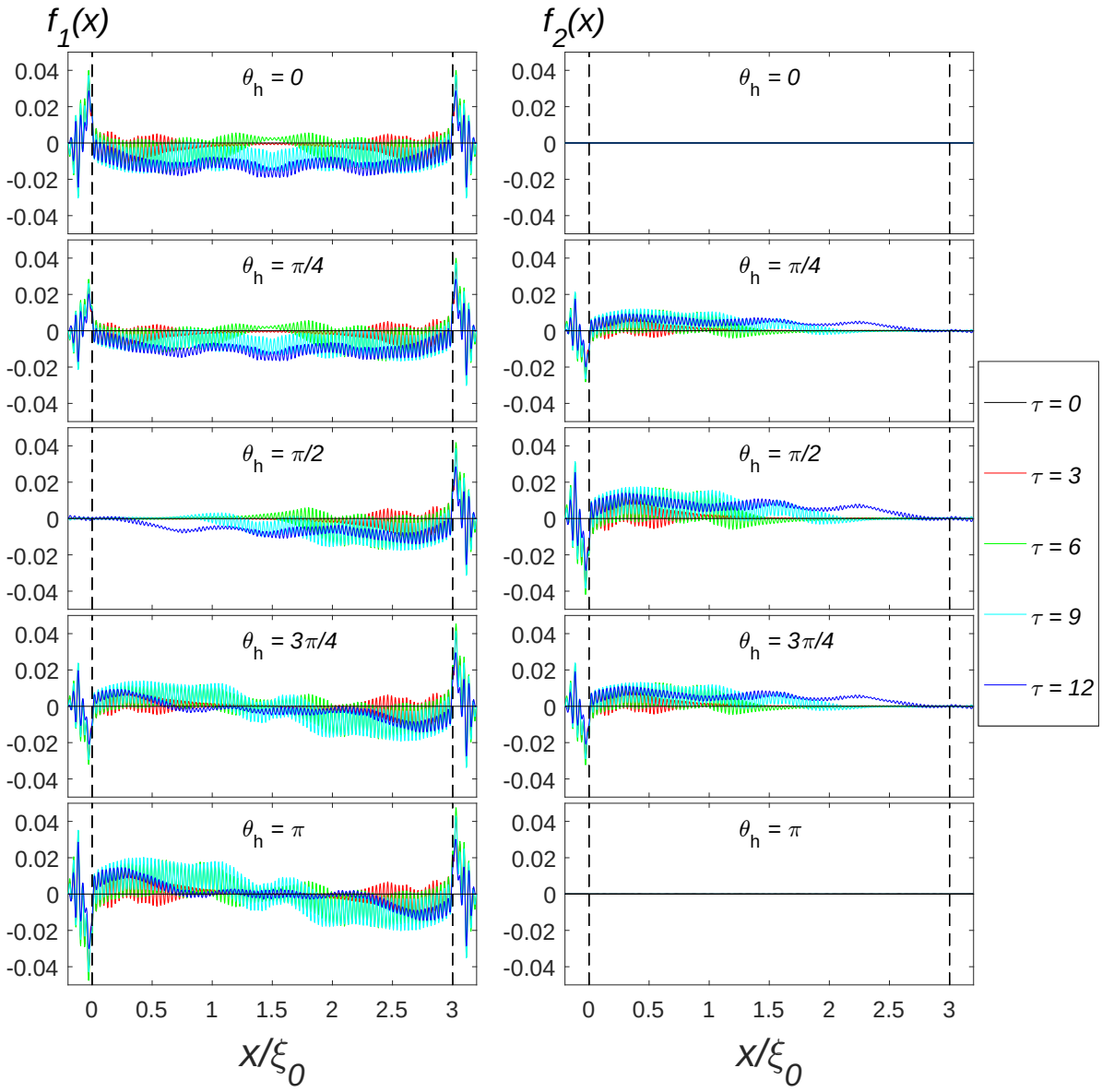

Figure 4.13: The triplet amplitudes, f_1 and f_2, plotted for the F/S/F-structure for five different magnetization angles. The amplitudes are plotted for five different relative times τ, each with a different colour. The dotted black lines mark the junctions between the three regions.

When $\theta_h \in \{0,\ \pi\}$, the system is symmetric or antisymmetric, respectively. This is reflected in f_1, being symmetric and anti-symmetric in these situations. For both these special cases, s_z is a good quantum number, thus forbidding the existence of an f_2-amplitude. For non-aligned spins however, the f_1-amplitude loses its symmetry, while an f_2 amplitude arises. The f_2-amplitude is at its greatest at $\theta_h = \pi/2$. For the f_2-amplitude to correspond to a long-range amplitude, it needs to enter a region in which the magnetic field is polarized in the z-direction, which is the case in the F2-region. However, it is evident that the amplitude weakens greatly inside the S-region, and only a small fraction reaches the F2-region.

Another observation worth mentioning is that the combined leakage of Cooper

pairs into the triplet channel seems to be lowest when $\theta_h = \pi$, and the largest leakage seems to occur for $\theta_h = 0$. For intermediate configurations with non-aligned magnetic fields, both the f_1-channel and the f_2-channel are open. However, the combined leakage of singlets into triplets seem to decay as θ_h is increased, although two channels are open. This implies that the number of states inside the superconducting gap should presumably be at the lowest, and the critical temperature its highest, when $\theta_h = \pi$.

We confirm this by plotting the LDOS at four positions inside the system, inside the F1-region, at the interface, and at two positions of various length inside the S-region. The results are plotted for the same set of θ_h's as above in Fig. 4.14, each given with a different colour. We clearly observe how the number of states inside the gap gradually falls as θ_h approaches π, and this applies for all positions. This result indicates that there are fewer triplet states for this magnetic field orientation, and is consistent with the triplet correlations observed in Fig. 4.13.

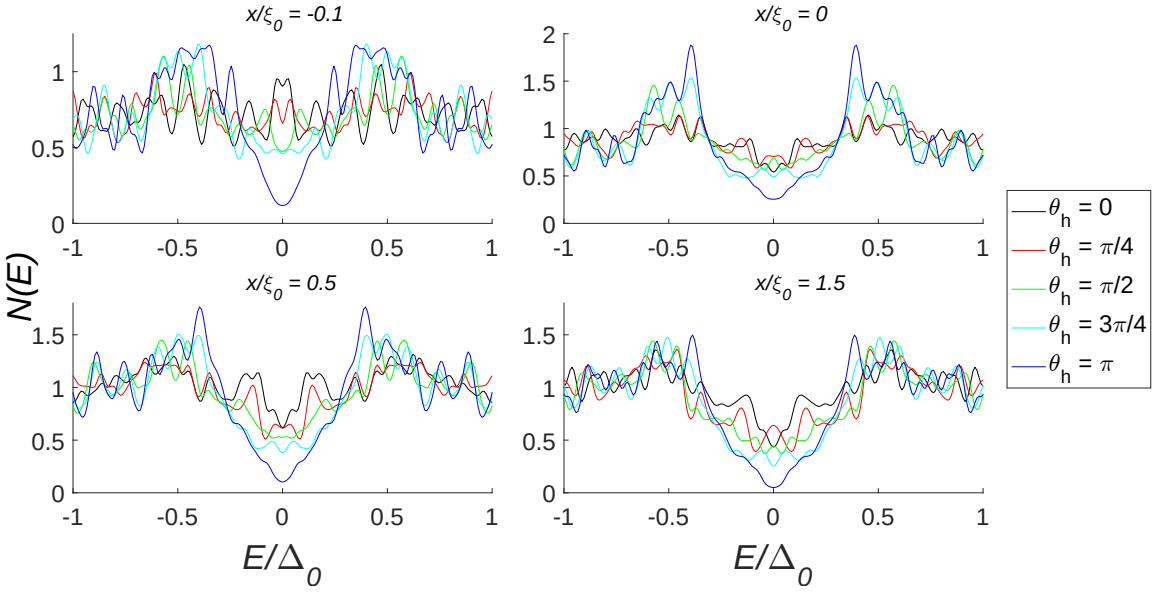

Figure 4.14: The LDOS plotted at four positions inside the F/S/F-structure, at positions indicated by the text above each plot. Each colour corresponds to a value of θ_h, as given by the legend. The results are obtained with $N_\perp = 1000$.

From the results obtained so far, we have argued that an antiparallel magnetic field configuration would result in the highest critical temperature. This hypothesis has been tested explicitly for an F/S/F-structure of equal d_{F1} and d_{F2} as above, but with the S-region shortened to $d_{\mathrm{S}}/\xi_0 = 2$.[d] The results are plotted in Fig. 4.15.

[d]This change of superconductor length had to be done due to the greatly reduced computational power this requires. The analysis for a system of length $d/\xi_0 = 3.4$ was not able to run on one node of the HPC with the required accuracy. The qualitative physics remain however the same.

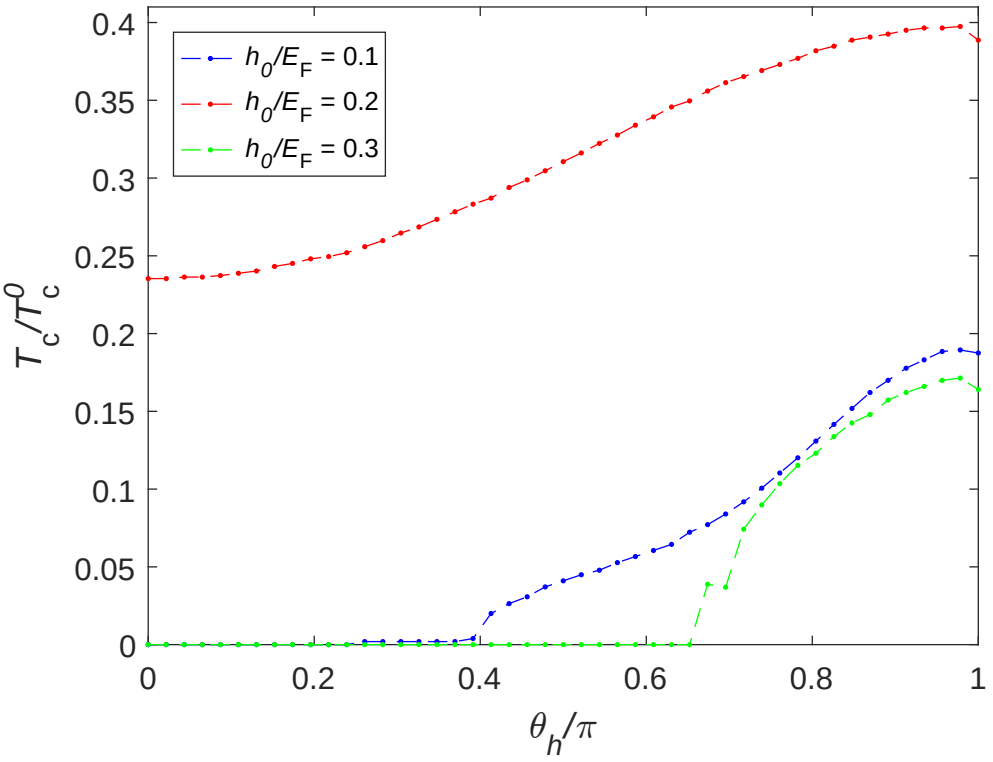

Figure 4.15: The critical temperature of the F/S/F-structure plotted as function of the relative magnetization angle θ_h. It is plotted for three magnetic field strengths, $h_0/E_F = 0.1$ (blue), 0.2 (red) and 0.3 (green).

As predicted, the critical temperature in general increases with an increasing magnetization angle. For $h_0/E_F = 0.2$, the critical temperature is non-zero for all θ. For $h_0/E_F = 0.1$ and $h_0/E_F = 0.3$ however, T_c is zero up to a certain critical θ_h, after which the critical temperature increases close to monotonically. This difference between the magnetization strengths is probably a result of the same h_0-dependence of T_c as discussed in Chapter 4.4. There is a local minimum in the graph for $h_0/E_F = 0.3$ at about $\theta_h = 0.7\pi$. This minimum is however not very prominent, and might as well be a result of a numerical imprecision. More interestingly, all graphs decrease slightly just as θ_h approaches π. Although an interesting result, we will not go further into the F/S/F-structure in this thesis.

We have showed that the critical temperature of the F/S/F-structure is highly θ_h-dependent. The results also reveal that it could indeed create and control long-range triplet Cooper pairs. The F/S/F-structure is thus a potential building block in spintronics devices, and may serve as for instance a spin-valve.[62] A downside of the structure is the need for a long S-region.

4.5.2 F/F/S-structure

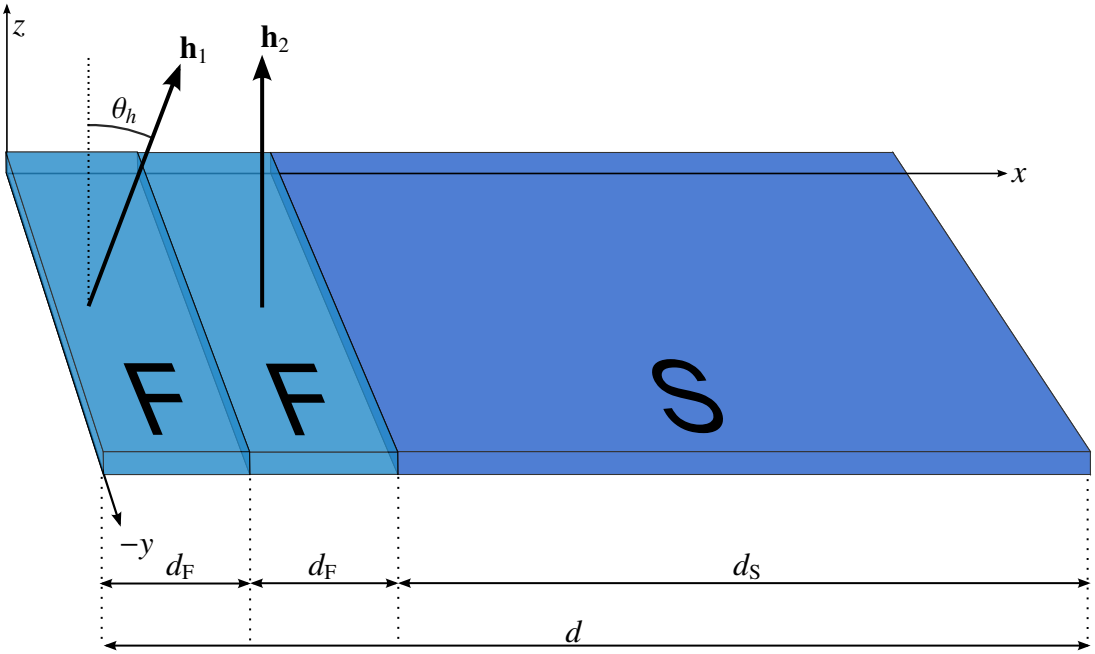

Figure 4.16: An illustration of the F/F/S-structure. The system considered is in reality not of restricted length along the y-axis, but is of infinite extent in this direction. Moreover, the structure is of zero height, that is of no extent in the z-direction.

We now perform the same analysis for the F/F/S-structure, for the same values of θ_h and τ. The system is sketched in Fig. 4.16. Putting the F-regions together should solve the problem regarding the need for a long S-region we encountered for the F/S/F-structure. Since this system shares a lot of properties with the F/S- and F/S/F-junctions, we will not plot all properties, but give only the relevant differences.

First, we look at the triplet amplitudes, which are depicted in Fig. 4.17. These share some properties with the F/S/F-structure, amongst them the zero-valued f_2-amplitude for aligned fields, which is yet again a consequence of the commutation between the σ_z-operator and the Hamiltonian for these cases. The f_2-amplitude arises when θ_h is different from 0 and π, and seems to be at its overall greatest for $\theta_h = \pi/2$. There are however some quantitative differences from the F/S/F-structure. The triplet production seems to be maximum at about $\theta_h = \pi/2$, and approach minima at $\theta_h \in \{0, \pi\}$. Compared to the F/S/F-structure, this structure also has a much greater amplitude of long-range Cooper pairs, that is Cooper pairs spin-polarized in the direction of the magnetic field. For $\theta_h = \pi/2$, f_1 corresponds to long-ranged Cooper pairs in the left F-region, while f_2 always corresponds to long-ranged pairs in the rightmost F-region. One can observe that these amplitudes are much greater than they were for the F/S/F-structure. As for the F/S/F-structure, f_3 is zero for all θ_h and τ, and is thus left out of further analysis.

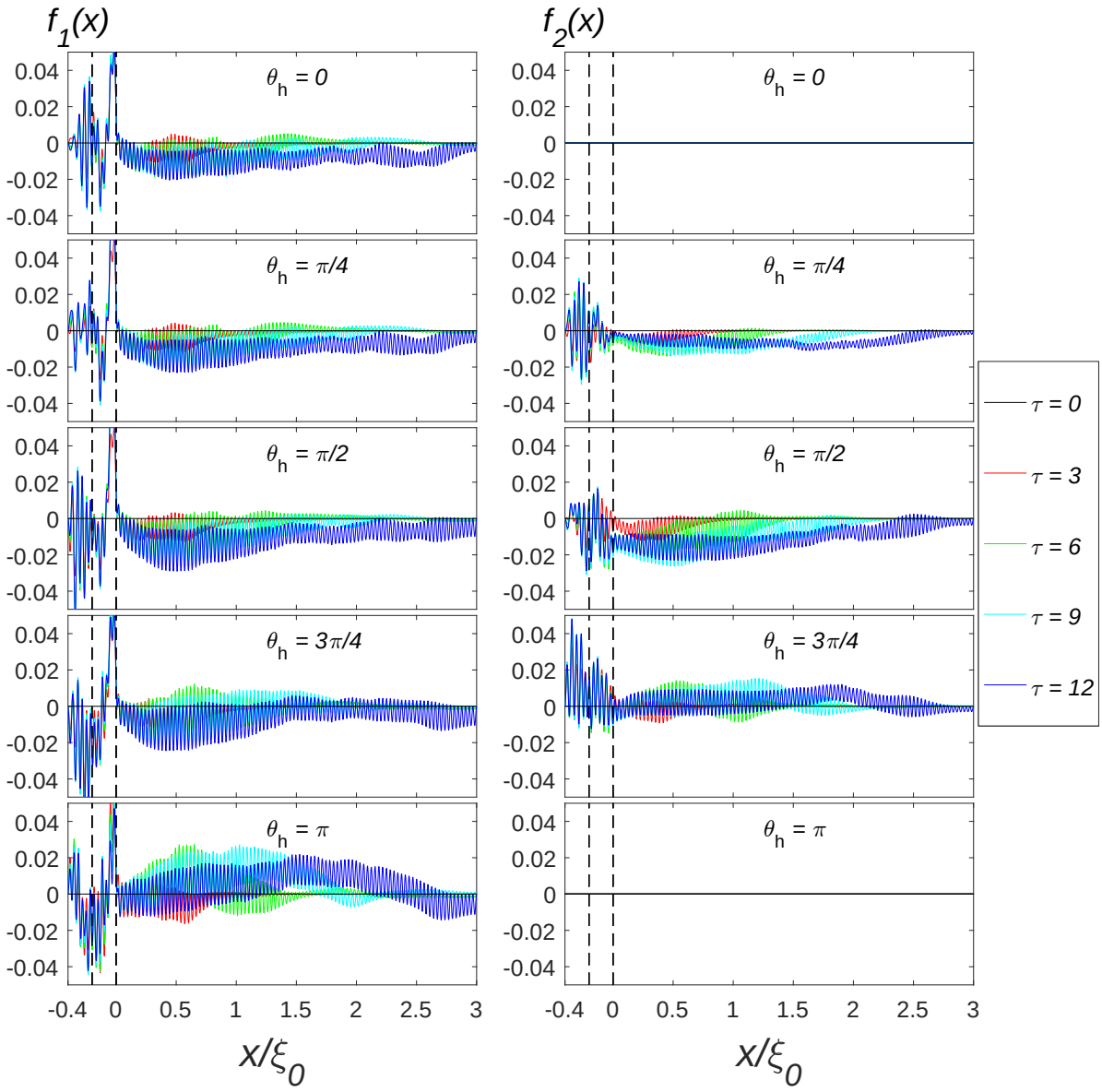

Figure 4.17: The triplet amplitudes, f_1 and f_2, for the F/F/S-structure, plotted for five different magnetization angles, θ_h. The amplitudes are plotted for five different relative times, τ. The dotted black lines mark the junctions between the three regions.

Furthermore we expect that putting the F-regions together, which essentially means that we only have F/S-proximity effect on one side of the superconductor, gives a rise in the critical temperature compared to that of the F/S/F-structure. This is confirmed by Fig. 4.18, in which the critical temperature is plotted with respect to the relative magnetization angle θ_h for three different magnetic field strengths. As for the F/S/F-structure, the system under consideration in the T_c-plot consists of a superconductor of length $d_S/\xi_0 = 2$, while $d_{F1}/\xi_0 = d_{F2}/\xi_0 = 0.2$. The lowest obtained critical temperature for this structure is about $0.55T_c^0$, for $I = 0.3$, and superconductivity is thus much more robust compared that of an F/S/F-structure of equal dimensions.

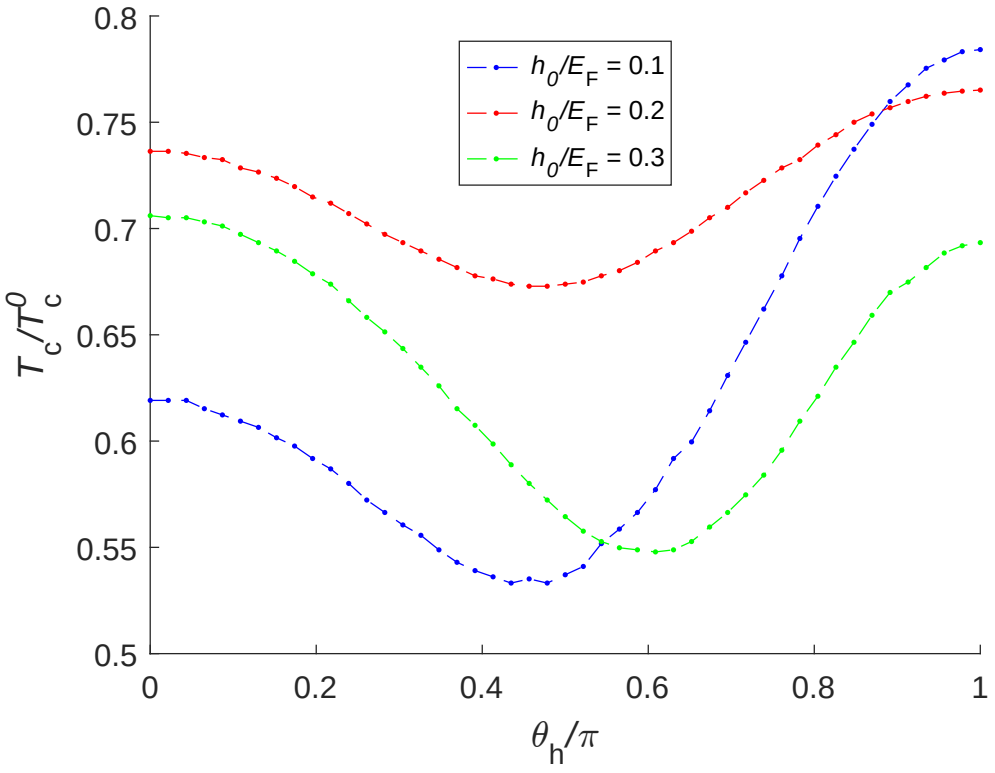

Figure 4.18: The critical temperature of the F/F/S-structure plotted with respect to the relative magnetization angle, θ_h. The results are plotted for three different magnetic field strengths, as indicated by the legend.

In this system, as opposed to in the F/S/F-structure, the minimum in T_c is not at $\theta_h = 0$, and the maximum is not necessarily at $\theta_h = \pi$. Fig. 4.17 indicated that the leakage of singlets into triplet pairs reached a maximum when $\theta_h \approx \pi/2$. As leakage of singlets generally weakens superconductivity, this is thus also where we expect the minimum of the critical temperature to be. As is evident from Fig. 4.18, the minimum of the graphs are all found around $\theta_h = \pi/2$. The exact behaviour of T_c is however dependent upon the magnetic field strength, and this indicates that there are more parameters than simply θ_h which affect T_c.

The F/F/S-structure shows promising properties. By adjusting macroscopic parameters like magnetic fields strength and magnetization angle, we are able to control both the critical temperature and the triplet production in the system. The structure moreover produces long-range triplets, which makes it interesting for technological purposes in spintronics.

5 Spin-orbit coupling

In the previous chapter, we have seen some important results on the proximity effects which arise when superconductors are combined with either normal metals or ferromagnets. Of particular interest are the effects which occur with inhomogeneously magnetized ferromagnetic regions. These systems produce not only short-ranged Cooper pairs, but also the long-ranged Cooper pairs. By rotating two individually homogeneous ferromagnets relative to each other, we are moreover able to turn superconductivity on and off. We have also seen that superconductivity shows re-entrant behaviour even in simple F/S-structures in two dimensions when adjusting the magnetic field strength. Superconductivity, which is of microscopic origin, may therefore be controlled by adjusting macroscopic system parameters. This effect may for instance be used in spintronics, as a control parameter, on equal grounds as gate voltage is used to control transistors in regular electronics today.

In this chapter we aim to explore the effects of combining spin-orbit interaction with S-, F- and N-regions. We will develop a quantum mechanical understanding of how spin-orbit coupling impacts the Cooper pairs and superconductivity in general. Thereafter we will use this knowledge to suggest new systems which may be used to control superconductivity by adjusting macroscopic parameters, just as we observed when adjusting the relative magnetization angle θ_h in Chapter 4.5. We will look into two types of SOC, namely SOC in an interface, and in-plane SOC.

5.1 SOC at an N/S-interface

In order to temporarily put aside the effects of ferromagnets, we start out by considering a simple N/S-structure in which there is a thin SOC-inducing layer between the two regions. Experimentally, this can be realized by using a thin heavy metal (large atomic number Z) such as Pt or Au between the N- and S-regions.[63] The normal metal could for instance be chosen to be Cu,[64] while Nb and Al are both good candidates for the superconductor.[65] As the SOC-layer is thin, the mathematical model of the spatial distribution of the interaction mimics how we would model impurities. While a magnetic impurity is expected to have a large impact in superconductivity,[66] a non-magnetic impurity should not have that large of an impact due to Anderson's theorem.[67] In order to understand better the impact of SOC, we will therefore compare the results of SOC with both magnetic and non-magnetic impurities. We refer to Chapter 4.3 for comparison with respect to a clean N/S-junction, that is without SOC.

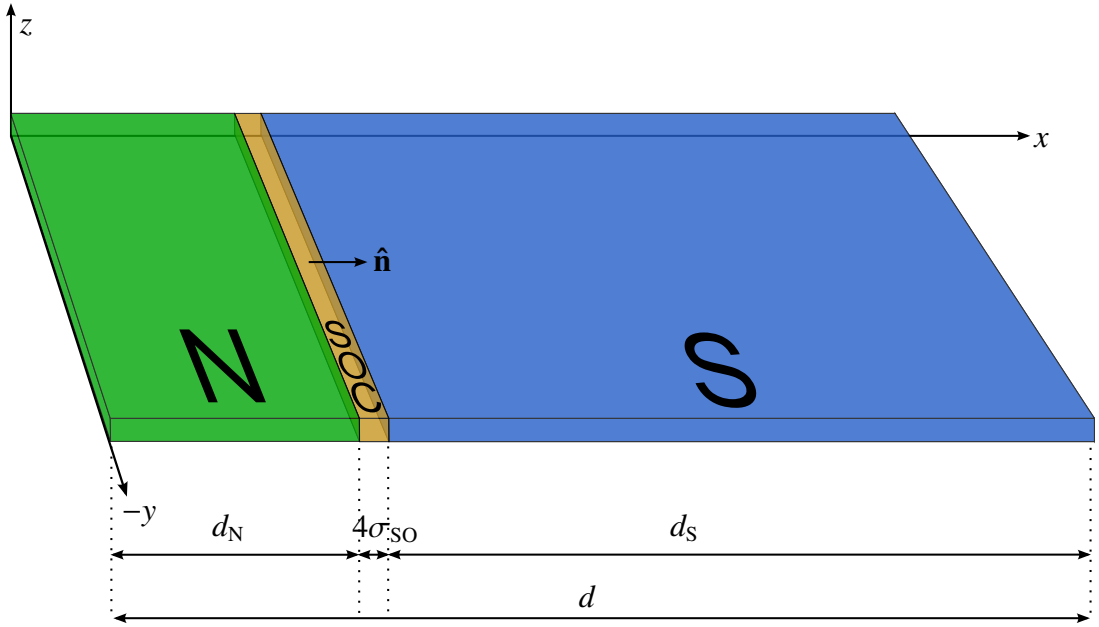

Figure 5.1: An illustration of the N/S-structure with SOC in the junction. The system considered is in reality not of restricted length along the y-axis, but is of infinite extent in this direction. Moreover, the structure is of zero height, that is of no extent in the z-direction.

The system which is used in most of this chapter is defined in Table 2, and illustrated in Fig. 5.1. For the impurity systems, we use α_h to denote the magnetic impurity strength, and α_U to denote the non-magnetic impurity strength. Both the SOC-layer and the impurities are modeled with a Gaussian distribution, that is

$$h_{SO}(x) = N(x; \lambda_{SO}, \sigma_{SO})\alpha_R(\hat{\mathbf{n}} \times \hat{\boldsymbol{\sigma}}) \cdot \mathbf{k}, \tag{5.1}$$

$$\mathbf{h}(x) = N(x; \lambda_{SO}, \sigma_{SO})\alpha_h \hat{\boldsymbol{\sigma}}, \tag{5.2}$$

$$U(x) = N(x; \lambda_{SO}, \sigma_{SO})\alpha_U, \tag{5.3}$$

where λ_{SO} is the center of the Gaussian distribution, placed in the middle of the SOC layer. σ_{SO} is the variance of the Gaussian distribution, and is quantitatively defined in Table 2. Most of the distribution is contained within a width of $4\sigma_{SO}$. In the case of SOC, the axis of symmetry breaking which causes SOC to occur is $\hat{\mathbf{n}} = \hat{\mathbf{x}}$. Since we consider only two dimensional systems, the SOC Hamiltonian therefore reduces to the z-component of the Hamiltonian derived in Eq. (2.48).

Table 2: Definition of the system parameters for the N/S-structure with a SOC-inducing layer in the interface.

System parameter	Definition
Length of S-region	$d_S/\xi_0 = 1$
Width of SOC layer	$4\sigma_{SO}/\xi_0 = 0.03$
Length of F-region	$d_N/\xi_0 = 0.2$
SOC strength	$\alpha_R k_F = 0.3$

In Chapter 5.1.3 we will plot the critical temperature with respect to the superconducting region's length, d_S, which will thus be varied rather than set to the constant value defined in Table 2. The same applies for the Rashba parameter in Chapter 5.1.4, where the critical temperature is plotted with respect to α_R.

5.1.1 Pair amplitudes

The singlet pair correlation, $f_0(x)$, for a SOC-layer in the junction of an N/S-structure, as a result of a self-consistent numerical calculation of the superconducting gap parameter, is depicted in Fig. 5.2. Compared to a clean N/S-structure, of which results are plotted in Fig. 4.4, it seems that including a layer of SOC in between the N- and S-region gives no significant difference in the singlet amplitude. By taking a closer look however, one may observe that the amplitude of f_0 drops inside the SOC-region compared to in the S-region, and this slightly suppressed amplitude continues into the N-region.

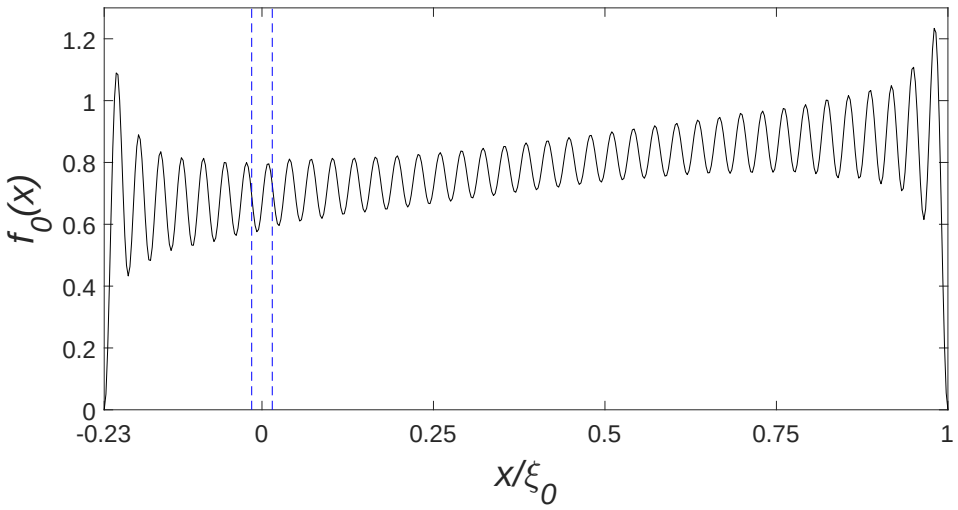

Figure 5.2: The singlet pair correlation $f_0(x)$ plotted for an N/S-structure with SOC at the junction. The system is defined properly in Table 2.

In Chapter 2.3, we compared SOC to magnetic fields, as SOC seems to induce a magnetic field from a particle's perspective. This induced magnetic field is dependent upon momentum, and particles with opposite momenta thus experience opposite pointing magnetic fields. In a singlet Cooper pair, which consist of, namely, opposite moving electrons, the two electrons experience antiparallel magnetic fields. However, as the spins of the two particles are opposite as well, their experience of the SOC is in fact equal. Hence, although interfacial SOC induces what may be interpreted as a magnetic field, an important difference from *real* magnetic fields is that it in fact does not cause a phase change to the singlet Cooper pairs. Put in other words, it does not give the Cooper pair a finite CoM. Therefore it does not break down superconductivity as violently as magnetic fields do.

The magnetic field induced by SOC may therefore rather be interpreted as either a potential barrier or a potential well for the Cooper pairs. We know from introductory quantum mechanics that such a potential barrier/well causes reflection, that is not all particles are being transmitted through the junction, but some are rather being reflected. In the limit of a very strong barrier, the classical limit will be realized, in which all particles are being reflected. If we make the SOC-region sufficiently thin, the barrier/well may be approximated as a δ-potential. An important result for the δ-potential is that the reflection coefficient does not depend on the sign of the potential, that is whether it is a δ-barrier or a δ-well. Thus if we were to make this approximation to our N/S-junction with SOC, both types of Cooper pairs, that is $\psi_{\mathbf{k},\uparrow}\psi_{-\mathbf{k},\downarrow}$ and $\psi_{\mathbf{k},\downarrow}\psi_{-\mathbf{k},\uparrow}$, would be reflected and transmitted equally in the SOC-region. Note that this reflection basically protects our Cooper pairs from entering the region in which they are suppressed, that is the N-region. In the limit of infinitely strong SOC, one would due to this argument expect all singlet Cooper pairs to be reflected, thus causing the superconductor to experience bulk conditions. We would also expect the results for SOC in such an N/S-structure to be fairly equal to what would be obtained if the SOC-region was exchanged with a potential barrier, that is a thin non-magnetic impurity.

The discussion above treats electrons inside the superconductor with well defined momentum. These kind of states are not eigenstates of the system, even inside a clean superconductor, and it makes the discussion rather a hand-waving argument. In order to fully understand what SOC does to the Cooper pairs, we choose to go to the quasiparticle basis, and expand the wave function in terms of momentum basis quasiparticle wave functions, $u_{\mathbf{k},\sigma}$ and $v_{\mathbf{k},\sigma}$. These quasiparticles are eigenstates inside a clean superconductor, and are therefore more suited for this discussion. We remember that a quasiparticle's dispersion relation in a clean superconductor is $E_{\mathbf{k}}^{\pm} = \pm\sqrt{\epsilon_{\mathbf{k}} + |\Delta_{\mathbf{k}}|}$, where the $\pm$-sign denotes either quasiparticles or quasiholes, and of which all notation is properly defined in Chapter 2.1.1. The quasiparticles are thus not allowed to live inside the energy gap $E_{\mathrm{F}} \pm \Delta$ in a clean superconductor. However, when the structure is no longer a clean S-structure, but either N- or F-regions are introduced, states appear inside the band gap, referred to as the proximity effect. These states are suppressed inside the S-region, and far inside the superconductor, none of these states are left, and the band gap resembles a fully developed state. On the other hand, if the proximity effect is made sufficiently strong, superconductivity breaks down.

From a mathematical point of view we know that the Schrödinger equation implies continuous wave functions. The reason why the quasiparticle states with energies inside the band gap appear in the F- and N-region is that they are allowed here, while being suppressed in the S-region. However, a continuous wavefunction implies that they must be present a certain length into the superconductor as well, if present in the N- or F-region. Under most conditions, the derivative of the wave function must also be continuous, putting limits to how fast the quasiparticle amplitudes may decay in the S-region. Introducing a δ-potential in the junction between such regions however, allows the derivative of the wave function to be discontinuous. With increasing strength of the δ-potential, the wave function amplitudes of these states may be fully present inside the N- or F-region, while suppressed increasingly fast inside the S-region. Following this argument, a δ-potential protects the superconductor against the

states that destroy superconductivity, thus effectively enhances superconductivity. We have therefore reached the same conclusion as was obtained from the electron point of view above, namely that SOC in an N/S- or F/S-interface should have a protective effect on superconductivity. Put in other words, SOC damps the proximity effect.

No s-wave triplet amplitudes appeared for this structure. As the Hamiltonian commutes with σ_z, it comes as no surprise that neither of the f_2- or f_3- amplitudes appeared. However, given that σ_z in fact appears in the Hamiltonian, one should perhaps expect a non-zero f_1. Quasiclassical calculations made in Refs. [68, 69] show that a two-dimensional N/S-structure with intrinsic SOC in the N-region results in non-zero triplet amplitudes. An important difference is however that the structure considered in this chapter does not have intrinsic SOC, but rather interfacial SOC. With intrinsic SOC in two-dimensional systems, the possible SOC-induced fields span a two-dimensional plane, whereas they can only be found along a one-dimensional line for interfacial SOC. Due to this, we can use the similarity to non-magnetic impurities to explain why no triplet amplitudes appear, namely that singlets do not gain finite CoM. Interfacial SOC is in fact qualitatively equal to intrinsic SOC in one dimension, in which the SOC-induced fields are also found along a line. For one-dimensional intrinsic SOC, the triplet amplitudes are indeed found to be zero by Ref. [68], and these quasiclassical results are thus not in contradiction with the results obtained here. As a matter of fact, the results are consistent.

5.1.2 LDOS

To test the reasoning above, the LDOS has been plotted at four positions inside the N/S-structure with SOC in the junction in Fig. 5.3. One position is just to the left of the SOC layer, one is in the center of the SOC-layer, one is just to the right of the SOC layer, and the last position is half a coherence length inside the superconductor. We use Fig. 4.5 as a reference, as this depicts the LDOS around a clean N/S-junction.

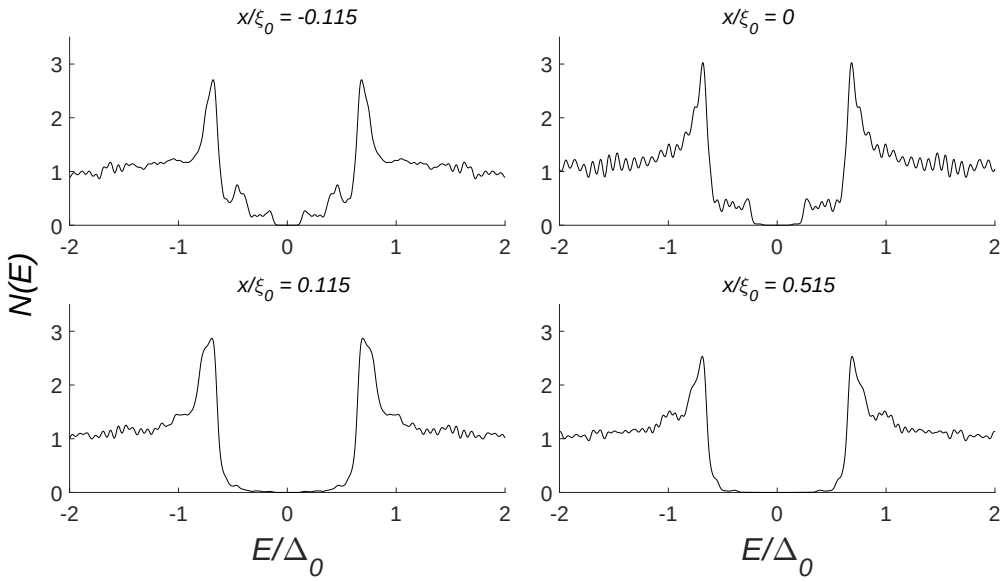

Figure 5.3: The LDOS plotted at four different positions inside the N/S-structure with SOC in the interface. The upper left position is inside the N-region, the upper right is in the middle of the SOC-region, while the lower plots are from two different positions inside the S-region. The results are obtained with $N_\perp = 2000$.

The plot in the upper left of Fig. 5.3 depicts the density of states inside the N-region, 0.1 coherence length from both the end of the system and the SOC-junction. This is the same position relative to the junction as depicted in the upper left plot in Fig. 4.5 for the clean N/S-structure. The results show that there are more states present within the gap inside the N-region when SOC is present. The states also seem to be more smeared out, and they are distributed much closer to the Fermi level than in the absence of SOC. That is, the minigap is narrower. Just inside the SOC-layer, depicted in the upper right plot, there are still many states present inside the gap, although being slightly attenuated compared to inside the N-region. Just $0.1\xi_0$ inside the superconductor, depicted in the lower left plot, there are almost no traces left of the states inside the gap. In contrast, for the clean N/S-junction, there are still many states present $0.1\xi_0$ into the superconductor, depicted in the upper right plot in Fig. 4.5.

These observations tell us that there are more states within the energy gap in the N-region, while in fact fewer such states inside the S-region, as compared to the clean N/S-structure. This is just in accordance with the discussion above, where it was reasoned that SOC allows more quasiparticle states to be present inside the N-region, as they are being reflected back and forth without entering the S-region. Equivalently and more mathematically, the SOC allows the derivative to change almost instantly at the junction (in the limit of a δ-potential, it may be discontinuous). This allows the wave functions of the quasiparticles to decay faster inside the S-region, without negatively affecting their amplitude inside the N-region. The observations in Fig. 5.3 imply that the wave functions behave in this manner, and the LDOS therefore supports

the reasoning made above.

Another observation is that the LDOS is symmetric about the Fermi level. As SOC is symmetric for an electron with spin σ and a hole with spin $-\sigma$, this comes as a natural consequence of summing over all $(\mathbf{k}, \sigma)$. Furthermore, the LDOS for spin-up and spin-down particles have been investigated separately, showing no difference between them. While a magnetic field creates a spin-dependent LDOS, SOC does not due to the momentum dependence. This may be understood from the fact that for every state $|\mathbf{k}, \uparrow\rangle$, there exists a state $|-\mathbf{k}, \downarrow\rangle$ which experiences just the same SOC-induced potential, and the same applies for $\uparrow \longleftrightarrow \downarrow$.

5.1.3 Critical temperature and the superconductor length

The critical temperature is plotted as a function of the length of the superconductor in Fig. 5.4, with the results for a SOC-layer in the junction to the left, and for a non-magnetic impurity to the right. The equivalent plot for the clean N/S-structure is given in Fig. 4.9. What is evident from the comparison with this figure, is that the qualitative difference in critical temperature with or without SOC present is rather small. Both systems gain the first non-zero critical temperature at $d_S \approx 0.1\xi_0$. T_c grows steadily with increasing length, and oscillates with a period of $\xi_0/32$. However, the oscillations are more prominent for the clean N/S-structure, hence a bit damped by the SOC-layer. The average critical temperature is more or less unaltered, but the minima and maxima are closer to the average for the SOC-system.

Hence, stating that a SOC-layer enhances superconductivity is a bit simplified and misleading. However, the results confirm that the proximity effect is damped. In the discussion of the oscillatory behaviour of $T_c(d_S)$ in Chapter 4.4.3, we concluded that this is a result of increasing the system width in half integers of the Fermi wavelength. Introducing SOC helps in decoupling the N- and S-region. The critical temperature of a clean superconductor above a certain length is more or less independent of its length. This implies that decoupling the regions should logically damp the oscillations, which is also what we observe. This damping helps protecting the superconductor by attenuating the minima, but also suppresses the symmetries in the wave functions which cause the maxima to appear.

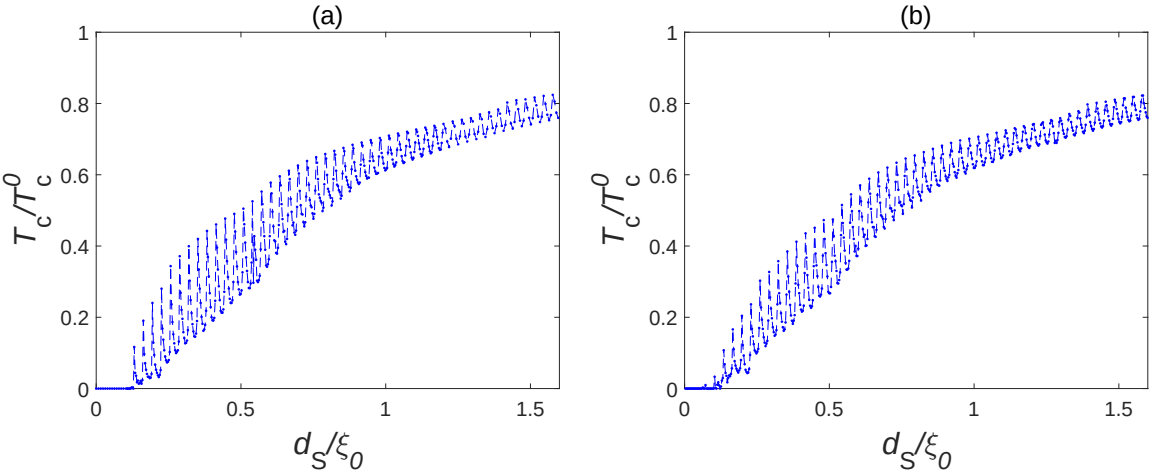

Figure 5.4: The critical temperature of an N/S-structure plotted with respect to the length of the superconductor, d_S. The length of the N-region is held at a constant $d_N/\xi_0 = 0.2$. Between the N- and S-regions, there is either a SOC-inducing layer (a), or a non-magnetic impurity (b), with a width of $4\sigma_{SO}/\xi_0 = 0.03$.

The results in Fig. 5.4 enable us to compare SOC (a) to non-magnetic impurities (b). It is evident that these curves show qualitatively the exact same behaviour. Although the exact numbers differ slightly, the overall behaviour more or less confirms our prediction, namely that SOC and non-magnetic impurities cause the same effect on an N/S-structure. Note that in this plot, we have plotted the critical temperature of the SOC-system with a defined $\alpha_R k_F$, that is the Rashba parameter times the Fermi wave vector, of which unit is energy. The Rashba parameter, of which unit is energy times length, does therefore not stand-alone specify the induced magnetic field strength experienced by electrons, but this field is momentum dependent. As the electrons forming Cooper pairs have approximately the Fermi energy however, and thus also $|\mathbf{k}| = k_F$, the SOC Hamiltonian returns a value of $\pm\alpha_R k_F$ for these electrons, given they are σ_z-eigenstates. A non-magnetic impurity on the other hand is simply a scalar potential field, returning a value of α_U for all spin-states. It should therefore come as no surprise, after realizing that SOC and non-magnetic impurities give almost the same effect on N/S-structures, that the critical temperature responds equally to equal α_U and $\alpha_R k_F$, that is the Rashba parameter scaled up with the Fermi wave vector.

5.1.4 Critical temperature and the Rashba coupling strength

Finally, we will look at how the critical temperature responds to an increasing Rashba parameter. The results above motivates us to compare the SOC-system with a non-magnetic impurity. In addition, we will compare these results to a magnetic impurity. These results are depicted below in Fig. 5.5.

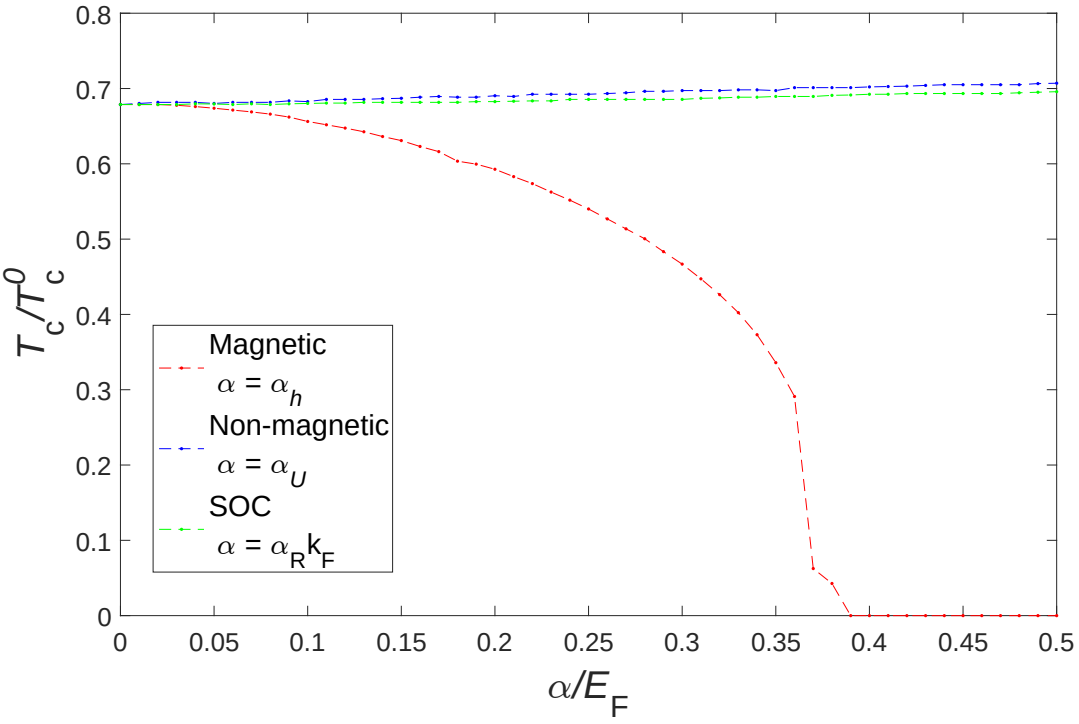

Figure 5.5: The critical temperature of an N/S-structure, with SOC (green), a non-magnetic impurity (blue) or a magnetic impurity (red) in the junction. The system has the same dimensions as the systems explored previously in this chapter.

This plot once more supports the hypothesis that a non-magnetic impurity and SOC gives the same effect to an N/S-structure. One may observe that the critical temperature is slowly increasing all the way from being a clean N/S-system, in which $\alpha = 0$, up to $\alpha/E_F = 0.5$. The critical temperature in the SOC-system increases by about $0.02T_c^0$ in this interval of α, while the non-magnetic impurity gives a rise in T_c by about $0.03T_c^0$. Hence these two systems behave rather equally, but the results are not exactly equal. This is probably due to the fact that the interactions are of very different nature, and we did a lot of approximations in arriving at the conclusion that SOC and a non-magnetic impurity affect an N/S-structure equally. Amongst these approximations, the most important one is probably the δ-potential approximation. While none of the potentials, neither the non-magnetic nor the SOC-induced one, behaves as a δ-function, the SOC-induced potential produces either a barrier or a well. When the potential is not a δ-function, the reflection coefficient is dependent upon being either a barrier or a well. Hence, since the non-magnetic impurity always acts as a potential barrier, there is a slight qualitative difference between these interactions.

Until now, we have focused on the equality between a non-magnetic impurity and a SOC-layer. As a mathematical equality to the magnetic Hamiltonian was discovered in the derivation of the SOC Hamiltonian in Chapter 2.3, we have included a magnetic impurity in Fig. 5.5 to show how this equality is not reflected in their impact on superconductivity. There is one important difference, namely that the SOC Hamiltonian is momentum-dependent, thus treating the Cooper pair forming electrons equally, as

discussed in the introduction to this chapter. The importance of this difference cannot be understated, as is evident in the plot. While the critical temperature rises slightly for increasing Rashba parameter, T_c shows a strictly decreasing behaviour as function of the magnetic impurity strength. At about $\alpha_h/E_F = 0.36$, it suddenly drops abruptly, before going to zero slightly thereafter. The magnetic impurity thus made superconductivity break down, as opposed to the SOC-layer, which stabilizes superconductivity by damping the proximity effect.

5.2 SOC at an F/S-interface

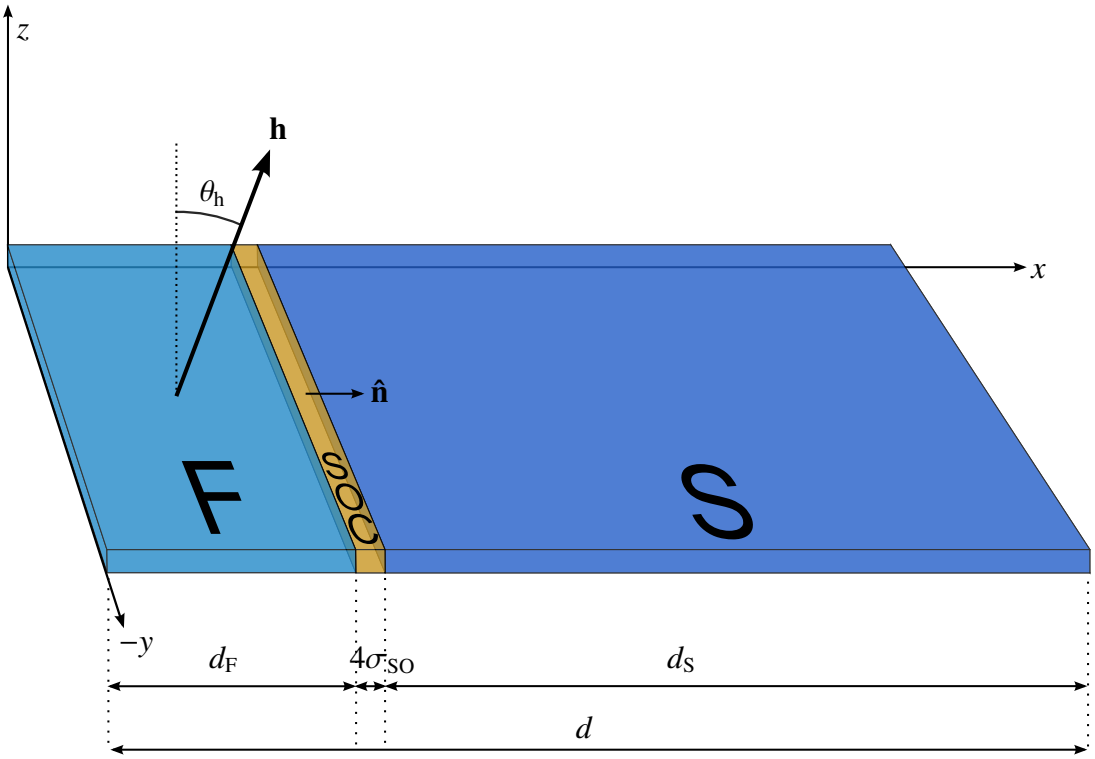

Figure 5.6: An illustration of the F/S-structure with SOC in the junction. The system considered is in reality not of restricted length along the y-axis, but is of infinite extent in this direction. Moreover, the structure is of zero height, that is of no extent in the z-direction.

The time has now come to switch on a magnetic field in the metal, thus looking at SOC in the interface between a ferromagnet and a superconductor. Experimentally, this may be realized by exchanging the normal metal with a ferromagnet. For weak ferromagnetism, good alternatives are for instance PdNi,[70] or Cu_xNi_{1-x} with $x \approx 0.5$.[71] In this chapter we will however apply rather strong magnetic fields, and clean ferromagnetic elements such as Fe, Co and Ni are relevant for this regime.[72] The system is illustrated in Fig. 5.6. The experience from the N/S-structure tells us that SOC protects the singlet Cooper pairs from the proximity effect, and we now want to check whether this effect remains in an F/S-junction. From the results in Chapter 4.4, we know that such a junction creates triplet Cooper pairs. Furthermore, introducing SOC

breaks spin-rotational invariance. We should therefore expect an effect from rotating the magnetic field. Without the presence of SOC, rotation of the magnetic field is equivalent to rotating the coordinate axes, which of course cannot impact physical quantities. Note that this only applies for the Hamiltonian used here, given in Eq. (3.1). For a full electrodynamic Hamiltonian, in which the coupling between the magnetic field and electric currents is included, this rotational invariance is broken already before introducing SOC.

The dimensions of the system explored in this chapter are the same as used in the last chapter, in which we had an N/S-junction with interfacial SOC. This system was defined in Table 2. The only difference is that we now introduce a magnetic field $\mathbf{h} = h_0(\sin(\theta_h)\,\hat{\mathbf{x}} + \cos(\theta_h)\,\hat{\mathbf{z}})$, where θ_h is magnetization angle relative to the z-axis. We could have been even more general, including magnetic field orientation along the y-axis. However, after introducing this type of SOC, the system remains spin-rotationally invariant around the axis which breaks full rotational invariance. As the SOC induces a magnetic field either in the $\pm\hat{z}$-direction, this means that a rotation in the xy-plane would not, and in fact could not, have any physical implications. In this chapter, the magnetic field strength is set to $h_0/E_\mathrm{F} = 0.3$, and the Rashba parameter is set to $\alpha_\mathrm{R}k_\mathrm{F}/E_\mathrm{F} = 0.5$.

5.2.1 Pair amplitudes

A numerical computation has been performed for five different magnetization angles, θ_h. As the SOC-induced magnetic fields may point either direction along the z-axis, the Hamiltonian is invariant under the transformation $\theta_h \to \pi - \theta_h$. The set of magnetization angles under consideration has therefore been set to $\{0,\ \pi/8,\ \pi/4,\ 3\pi/8,\ \pi/2\}$. The singlet pair correlations for all these angles are plotted in Fig. 5.7. This figure should be compared with Fig. 4.6, which depicts the results for a clean F/S-structure, that is without SOC.

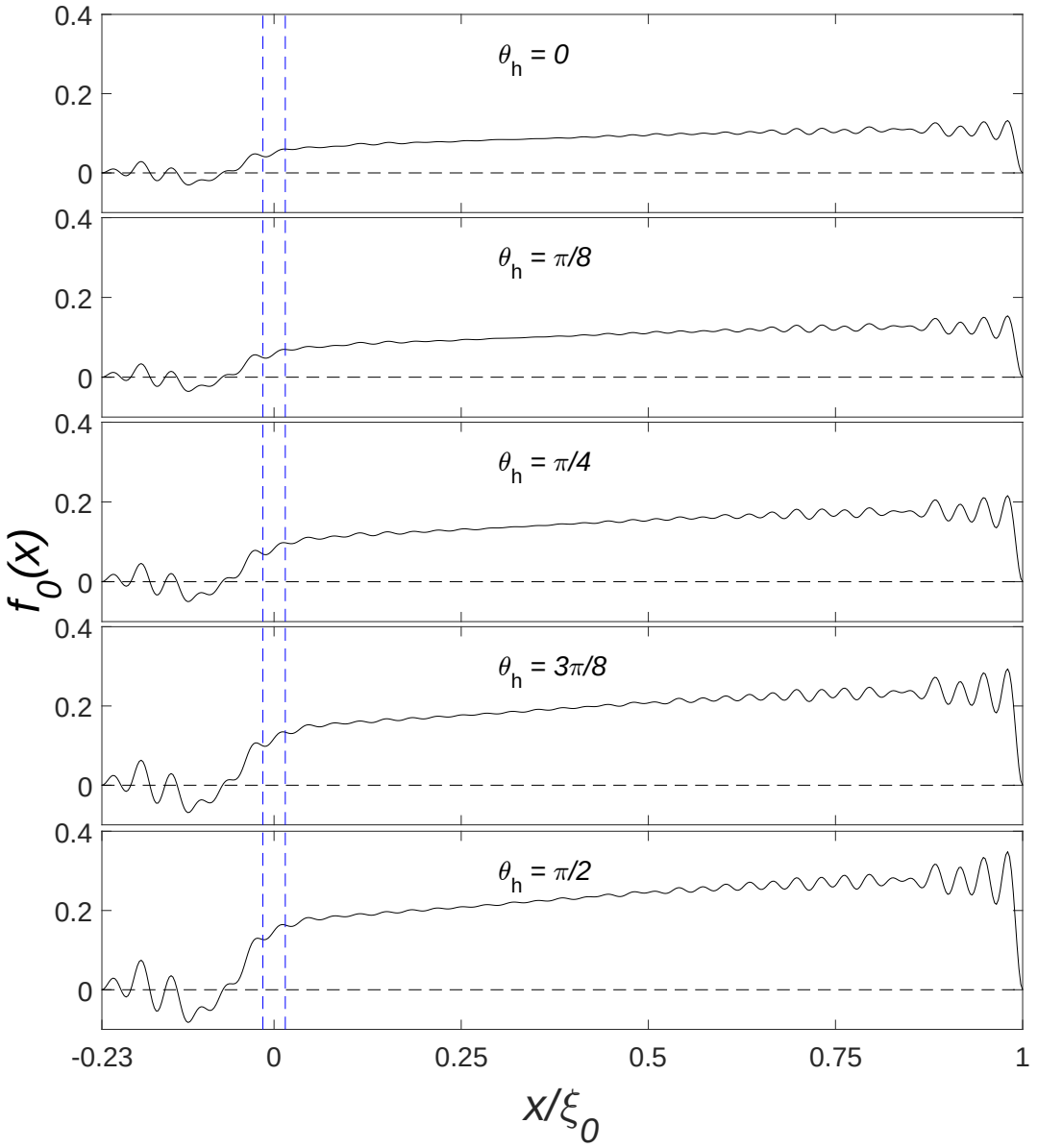

Figure 5.7: The singlet pair amplitude plotted for five different magnetization angles, θ_h, for an F/S-structure with SOC in a thin layer at the interface. The SOC-layer is Gaussian distributed inside the blue dotted lines (which cover a width of $4\sigma_{\mathrm{SO}}$).

The upper plot in Fig 5.7 shows the results for $\theta_h = 0$, and the magnetization angle is increased by $\pi/8$ for every plot downwards. It can be observed that the singlet correlation, and thus the superconducting pair potential, grows by increasing the magnetization angle. At $\theta_h = 0$, its maximum before the oscillations at the boundary is approximately 0.1. Growing steadily by increasing magnetization angle, this maximum doubles as θ_h approaches $\pi/2$. Hence, it seems as though a magnetization perpendicularly aligned to the SOC-induced magnetic fields results in best conditions for superconductivity to exist.

Before looking into theoretical explanations for this result, we study the *s*-wave triplet amplitudes as well. In the N/S-structure with interfacial SOC, no *s*-wave triplet

amplitudes appeared. We thus conclude that stand-alone SOC does not create triplets from singlets, that is, it does not cause phase shifts to $|\mathbf{k}, \sigma\rangle\,|-\mathbf{k}, -\sigma\rangle$-pairings. With the introduction of a magnetic field however, ($s_i = 0$)-triplet Cooper pairs, where i is the axis of magnetization, automatically appear. As long as there is no SOC present, the Hamiltonian commutes with the σ_i-operator, thus makes s_i a conserved quantity. Introducing SOC on top of this, we also add the σ_z operator to the Hamiltonian. If $i = z$, s_z is still a conserved quantum number, and we should therefore only observe ($s_z = 0$)-Cooper pairs. This is confirmed by the upper plot in Fig. 5.8, in which the triplet amplitudes for $\theta_h = 0$ are plotted. Only the ($s_z = 0$)-triplet amplitude appears, and s_z is thus conserved. However, by rotating the magnetic field such that $i \neq z$, s_z is no longer a conserved quantity. As is evident from the plots, with $\theta_h \neq 0$, f_2 is non-zero. This result is however not an exclusive effect of SOC, as rotating the magnetic field effectively rotates the Cooper pair amplitudes, as demonstrated in Chapter 2.4.1.

An interesting observation is that an f_3-amplitude appears as well for $\theta_h \notin \{0, \pi/2\}$. In the absence of SOC, the f_3-amplitude would not have appeared by rotating the magnetic field in the xz-plane, but would rather have required a non-zero y-component of the magnetic field. With SOC however, it clearly appears. Note however that its amplitude is about one order of magnitude lower than the f_1- and f_2-amplitudes. The appearance of the f_3-amplitude must be due to Cooper pair spin-mixing caused by SOC. In Chapter 2.4.3, a brief discussion of how SOC and an arbitrary magnetic field interacted was made, and it was concluded that it will generally result in spin-mixing for all magnetizations but for two special angles, namely 0 and $\pi/2$. This is just the effect observed here. At $\theta_h = 0$, s_z is a conserved quantum number, and no ($s_z = \pm 1$)-amplitudes may be produced. For increasing magnetization angles, the spin-mixing effect seem to grow. At $\theta_h = \pi/2$ however, only the singlet- and the f_3-amplitude are being mixed in pseudospin, as was derived in Chapter 2.4.2. At this angle, the Pauli principle forbids any mixing, and the f_3-amplitude must therefore be zero. Explicit tests have been performed, in which θ_h was set close to $\pi/2$. The analysis showed that the f_3-amplitude remained quite strong until θ_h was close to $\pi/2$, then dropping steadily to zero when θ_h passed a certain point. The non-monotonic behaviour of f_3 indicates that there are two competing forces in the production of this triplet amplitude. Increasing magnetization angle generally makes the effect of SOC stronger, increasing the f_3-amplitude. On the other hand, when the θ_h is close to $\pi/2$, the Pauli principle restricts the spin-mixing, eventually suppressing it completely. As the f_3-amplitude is always much lower than the remaining two triplet amplitudes, the spin-mixing effect must be weaker than the production of triplet Cooper pairs, mainly provided by the ferromagnet.

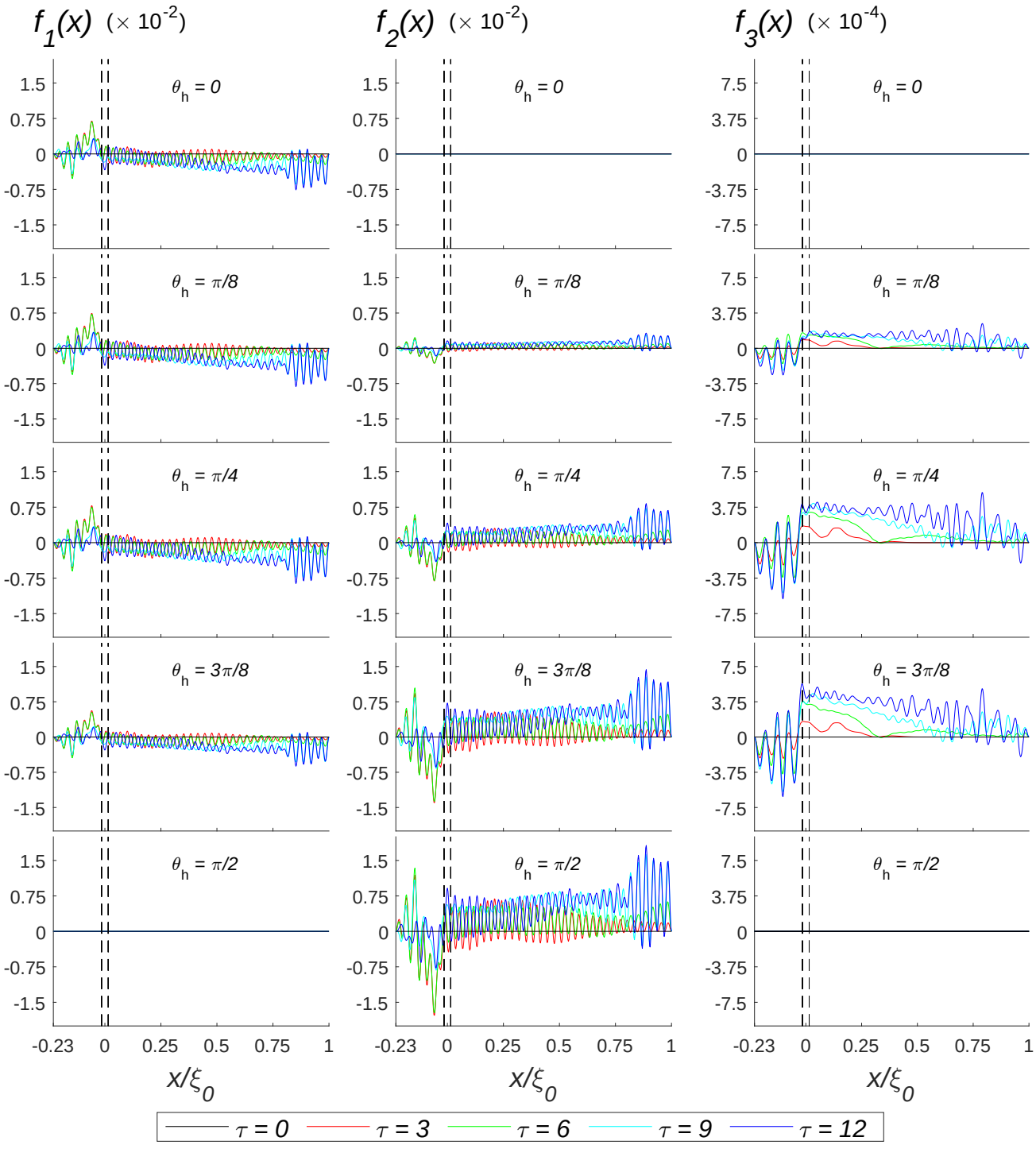

Figure 5.8: The triplet amplitudes for five different magnetization angles, θ_h, for the F/S-structure with a SOC-layer in the junction. Each plot contains triplet correlations for five different relative times, τ.

The downmost plots should be compared to the corresponding plots for the F/F/S-structure in Fig. 4.17, for magnetization angle $\theta_h = \pi/2$. We learned in this chapter that a magnetic field in the i-direction creates a ($s_i = 0$)-triplet amplitude. By introduc-

ing another magnetic field, which is not aligned to the first field, some of these triplet pairs are rotated into ($s_i = \pm 1$)-Cooper pairs. However, for the case of a SOC-induced magnetic field instead of a second magnetic field, still perpendicularly aligned to the first magnetic field, we observe in fact no rotation of one kind of triplet pairs into another kind of triplet pairs. Note that when $\theta_h = \pi/2$, the f_2 amplitude corresponds to triplet Cooper pairs with $\sigma_x = 0$, that is no spin-polarization in the x-direction. If the SOC-layer had been substituted by a magnetic field, an f_1-amplitude would have appeared, as it did for the F/F/S-structure.

We may now begin to search for an explanation of the strengthening of the superconducting energy gap with increasing magnetization angle. We know that such interfacial SOC in no situation induces triplet pairs without the help of a magnetic field, as experienced from Chapter 5.1. That is, it does not create triplets from singlets, as magnetic fields does. However, we have revealed that spin-mixing of the Cooper pairs generally occurs for all magnetization angles with exception of $\theta_h \in \{0,\ \pi/2\}$, which thus opens more triplet channels. In general, such opening of triplet channels is an argument for suppression of superconductivity, as we are used to from for instance the F/F/S- structure. What is observed is however just the opposite, namely that superconductivity is being enhanced. Note however that SOC does not cause any net increased triplet production from singlets. That is, there is no increased leakage of singlets into triplets. SOC simply redistributes the different kinds of triplets. Since singlet leakage is what causes superconductivity to be suppressed, SOC does therefore not cause this.

To grasp the physics of the system in the search for understanding, it helps to find the eigenstates. We once again refer to Chapter 2.4.2, where the eigenstates of such a system was derived, given in Eq. (2.68). For this derivation to apply directly here, we must redefine our coordinate system such that $x \longleftrightarrow z$. The main result of this chapter was that if the SOC-induced field is perpendicular to a magnetic field, a component of the singlet state becomes long-ranged. That is, if we project the singlet state onto the eigenbasis, it will in general be a linear combination of a pseudosinglet and a ($s' = \pm 1$)-pseudotriplet, the latter of which do not gain a relative phase throughout the system due to having zero CoM. As a consequence of this effect, the leakage of singlets is reduced, allowing for a larger singlet amplitude to sustain. This effect of SOC is θ_h-dependent, and will therefore increase as θ_h increases. The results obtained by numerical calculations seem to support this analysis. The singlet amplitude is about doubled by rotating the magnetic field from $\theta = 0$ to $\theta = \pi/2$.

If the reasoning above is correct, namely that there exist long-ranged singlet pairs, this should have measurable consequences. As the source of triplet pairs are singlet pairs, there must be an equilibrium between the amount of singlet and triplet pairs when the system as a whole is in in equilibrium. Hence, if we (fictitiously) increase the singlet pair amplitude without adjusting any other system parameter, we would in general expect the triplet amplitude to increase proportionally. However, if a fraction of the singlets are long-ranged, this fraction will by definition not be rotated into triplet pairs. We would thus expect the relative amounts of singlet and triplet pairs to be altered in favour of an increased singlet pair fraction. This has been analyzed closer for these results, and we have compared the two extrema, namely when $\theta = 0$ and $\theta = \pi/2$, where no spin-mixing occurs. Averaging both the singlet and the triplet amplitudes

gives that the average $f_0^{\theta_h=0}$ divided by the average $f_0^{\theta_h=\pi/2}$ evaluates to ≈ 0.3892, while the average $f_1^{\theta_h=0}$ divided by the average $f_2^{\theta_h=\pi/2}$ evaluates to ≈ -0.4051. The average triplet amplitude for $\theta_h = 0$ is therefore about 4% larger compared to the corresponding average singlet amplitude than it is for $\theta_h = \pi/2$, confirming this altered equilibrium.

5.2.2 LDOS

As a consequence of the analysis so far, we expect the band gap to be more developed for higher magnetization angles, θ_h. This is due to the creation of long-ranged singlets, which should imply fewer triplet states relative to singlet states, thus reducing the number of states within the band gap. When $\theta_h = 0$, this effect does not occur, and the plots should be qualitatively rather equal to the clean F/S-junction. However, as superconductivity in this system is very weak for $\theta_h = 0$, it is not directly comparable to the LDOS of the clean F/S-structure in Fig. 4.9, where the S-region is longer. For $\theta_h = \pi/2$, the effect should be at its maximum, creating the most prominent band gap. The LDOS at four different positions are plotted in Fig. 5.9, both inside the F- and S-region.

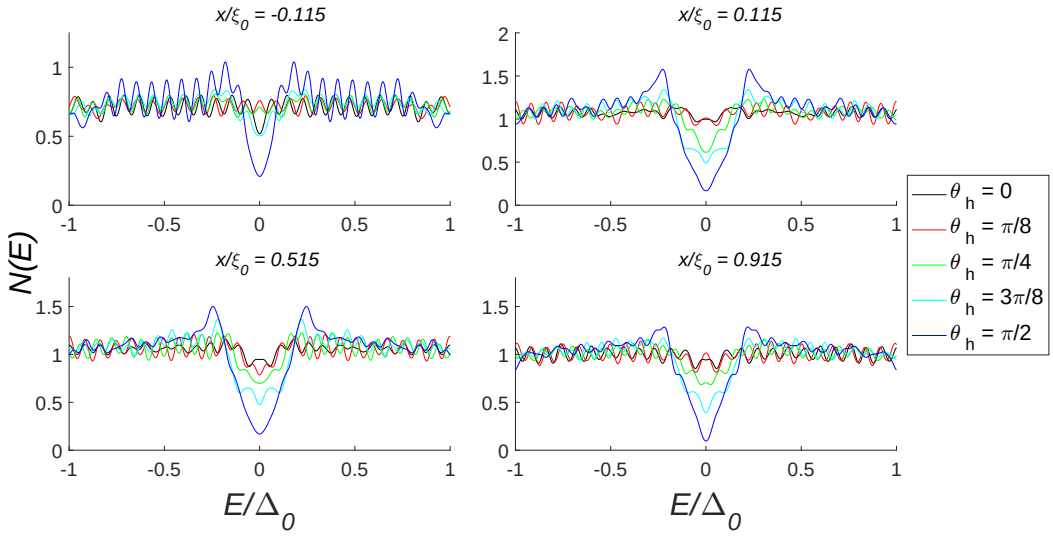

Figure 5.9: The LDOS for the F/S-structure with SOC in the interface plotted at four different positions, as indicated above each plot. At each position, the LDOS is plotted for five different magnetization angles, θ_h. The results are obtained with $N_\perp = 2000$.

The plots show very clearly that the superconducting gap becomes much more prominent for higher magnetization angles. For $\theta_h = 0$, one can in fact almost not spot any gap at all. As we rotate θ_h further towards $\pi/2$, this gap grows, and it is almost a complete gap for $\theta_h = \pi/2$. This applies to all positions in the system, both inside the F-region and inside the S-region. As the energy gap grows with θ_h, this indicates that the fraction of singlet states grows, and that superconductivity is thus being strengthened.

5.2.3 *Critical temperature*

It was evident from Fig. 5.7 that as θ_h was set closer to $\pi/2$, superconductivity was strengthened. To see how this affects the sustainability of the superconducting state, the critical temperature as function of the magnetization angle is plotted for three different Rashba parameters in Fig. 5.10.

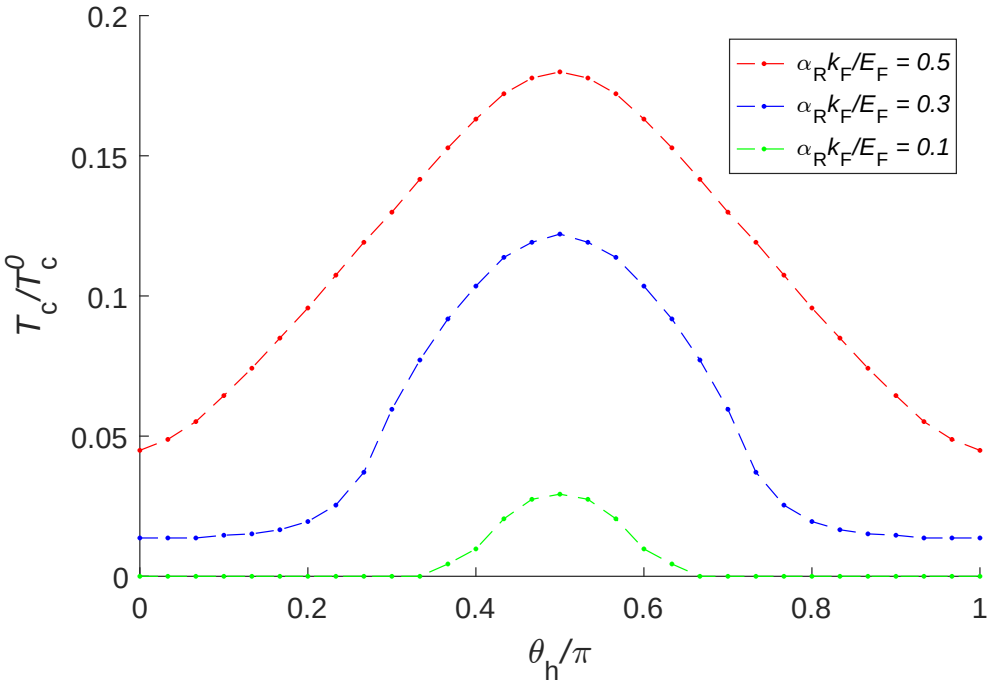

Figure 5.10: The critical temperature of an F/S-structure with SOC in the interface plotted for three different Rashba parameters, as function of the magnetization angle, θ_h.

Firstly, these results confirm that the Hamiltonian is invariant under the transformation $\theta_h \to \pi - \theta_h$, as the plot is symmetric about $\pi/2$. Furthermore, the results clearly indicate that the closer the magnetization angle is to $\pi/2$, the more robust is the superconducting state. This is an interesting result, as we are able to control the critical temperature by adjusting a macroscopic parameter. Although not directly comparable, these results show similar behaviour as obtained by a quasiclassical approach in the diffusive limit in Ref. [73]. In this paper, intrinsic Rashba-Dresselhaus SOC is explored for a three-dimensional S/F/S-trilayer structure. The results show that for equal weights of Rashba and Dresselhaus SOC, rotating the magnetic field over an interval of $\pi/2$ causes the critical temperature to go from minimum to maximum. This is just what we found for the F/S-structure with interfacial SOC studied here. For the purpose of simply controlling T_c, this system can thus serve as a substitute for the F/S/F- and F/F/S-structures, in which we observed the same behaviour of T_c. These results are plotted in Figs. 4.15 and 4.18 respectively. The results for SOC are most similar to the F/S/F-results, as the critical temperature grows monotonically for $\theta_h \in [0, \pi/2]$. However, the system considered in this chapter is only $1.23\xi_0$, and can thus be much shorter

than the length needed for a superconducting state to arise in an F/S/F-structure. As the SOC-layer generally weakens the proximity effect, this system configuration may also be shorter than needed for the F/F/S-structure.

In order for the rotation of θ_h to have a prominent effect on the critical temperature of the system, it is obvious that the system cannot be too long. If the system is of sufficient length, the superconducting state will be stable even though there is a ferromagnet at the end, and the effect of increasing the magnetization angle would eventually be negligible. For technological purposes, it is however interesting to obtain the largest possible variation in T_c by adjusting a macroscopic parameter. In order to find this point for a system with a F-region of length $d_F/\xi_0 = 0.2$, with magnetic field strength $h_0/E_F = 0.3$, and a Rashba parameter of $\alpha_R k_F/E_F = 0.5$, the critical temperature is plotted as function of the superconductor length d_S in Fig. 5.11.

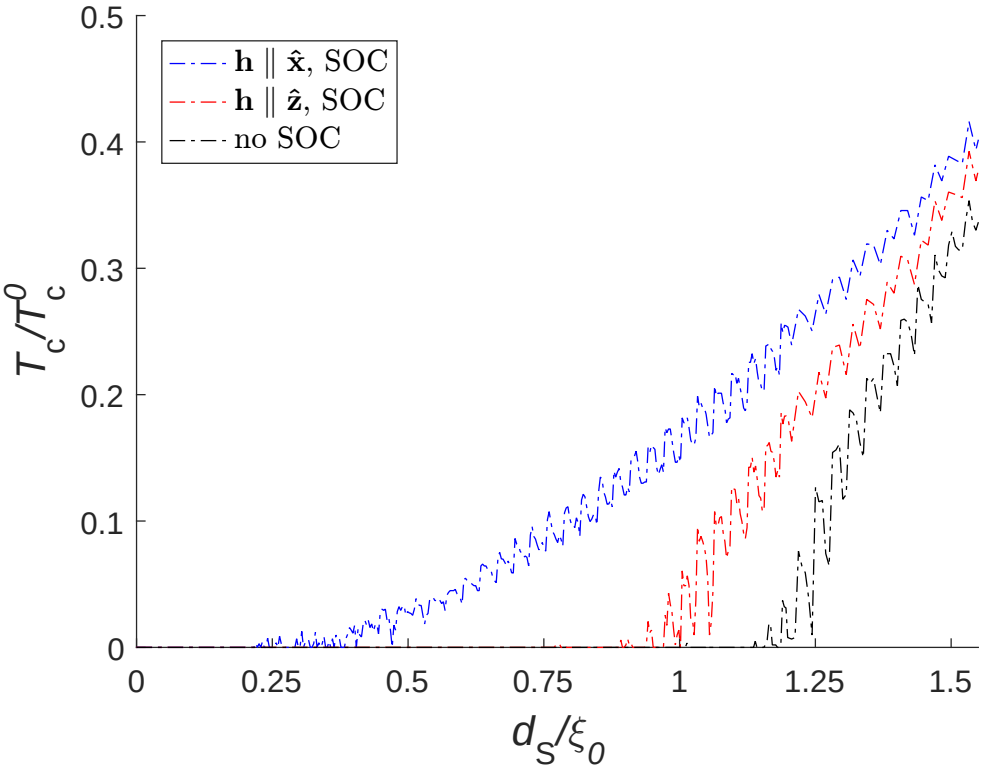

Figure 5.11: The critical temperature of the F/S-structure with SOC in the interface plotted with respect to the length of the superconductor, d_S. The red line depicts the results for $\theta_h = 0$, the blue line for $\theta_h = \pi/2$, whereas the black line depicts the results when SOC is switched off.

The results reveal that we in fact nearly did the analysis above for the d_S which would give the largest effect in T_c-variation. The plot shows that the maximum difference between the two magnetization angles is about $0.15T_c^0$. Additionally, the T_c-curve for the system with SOC switched off is also plotted in the same figure. This curve is

included to show explicitly that the SOC-layer indeed strengthens the superconducting state for all θ_h.

5.3 In-plane SOC in an S/F/S-structure

In this chapter, we will explore how in-plane SOC affects superconductivity. With *in-plane*, we mean (the equivalent of) setting up an electric field perpendicular to the plane in which we have defined our two-dimensional system, causing SOC-induced fields parallel to the plane of the physical system. We define our system to span the xz-plane. The SOC Hamiltonian for such a system is given in Eq. (2.53). This Hamiltonian has a lot in common with the Hamiltonian for SOC in an interface, and the last chapter may therefore serve as guide to what effects we expect. By studying this Hamiltonian, it can be observed that there is no longer an SOC-induced magnetic field along one axis. The induced fields now rather span a plane, namely the xz-plane. These magnetic fields are proportional to the momentum in each other directions, that is terms as $\sigma_x k_z$ and $\sigma_z k_x$ appear. In addition to these SOC-induced magnetic fields, there also appear effective magnetic point-impurities wherever the SOC-layer starts or stops. They appear as a result of the symmetrization procedure presented in Chapter 2.3.4, which was performed due to the requirement of the hermiticity of the Hamiltonian. These effective magnetic impurities do not depend upon momentum, and must therefore be interpreted as proper magnetic fields.

The results from the last section, and from the derivation of the eigenstates in mixed SOC- and ferromagnetic regions in chapter 2.4.2 has told us that SOC-induced magnetic fields combined with proper magnetic fields causes the singlet state to project onto the eigenbasis (where pseudospins are good quantum numbers) as a linear combination of a short-ranged pseudosinglet and a long-ranged pseudotriplet. This effect will in general be most prominent when the SOC-region and the ferromagnet are close, or even better, in the same region. We will therefore merely look at one structure in this chapter, namely an S/F/S-structure in which SOC is present in the entire F-region. We have here chosen a trilayer- rather than a bilayer-structure in order to study how the singlet amplitude sustains through the F-region, connecting the two S-regions. As SOC is restricted to a limited domain along one axis, there are induced two effective magnetic impurities, one at each boundary of the SOC-region. By putting an S-region on each side of the SOC-region, we will see the full effect of these effective magnetic fields. The structure is illustrated below in Fig. 5.12. Al and Nb once again serve as good candidates for the choice of superconductor. For the F-region with in-plane SOC, GaAs is a good choice, as it provides controllable SOC.[74] GaAs is however not ferromagnetic by itself. This may be solved by doping it with for instance Mn,[75] resulting in a structure with both intrinsic ferromagnetism and in-plane SOC. Ferromagnetism could also be proximity-induced by growing a thin ferromagnetic material on top of GaAs, such as an yttrium iron garnet (YIG).[76] These types of ferromagnetism are however not controllable. If such control is required, an external magnetic field can be applied.

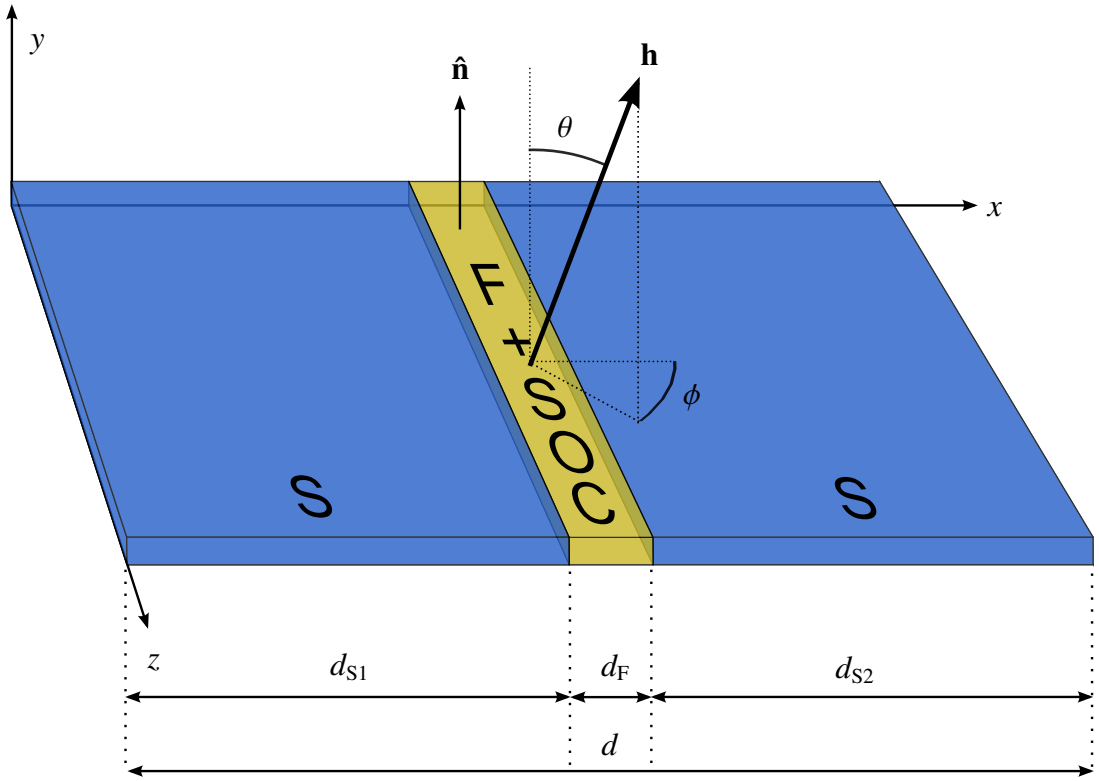

Figure 5.12: An illustration of the S/F/S-structure with in-plane SOC in the F-region. The system considered is in reality not of restricted length along the z-axis, but is of infinite extent in this direction. Moreover, the structure is of zero height, that is of no extent in the y-direction.

We define the S/F/S-structure according to Table 3. As SOC in general is expected to protect a fraction of the singlets, we need not define a very long system for superconductivity to sustain. Therefore, the full system length is only defined to be $1.1\xi_0$.

Table 3: Definition of system parameters for the S/F/S-structure with in-plane SOC inside the F-region.

System parameter	Definition
System length	$d/\xi_0 = 1.1$
Length of left S-region	$d_{S1}/\xi_0 = 0.5$
Length of right S-region	$d_{S2}/\xi_0 = 0.5$
Length of F-region	$d_F/\xi_0 = 0.1$
Magnetic field strength	$h_0/E_F = 0.1$

The Rashba parameter, $\alpha_R k_F$, will be varied between 0 and $0.5E_F$ for the various analyses, and will be specified in the coming sections. As in-plane SOC fully breaks spin-rotational invariance, we will keep the direction of the magnetic field completely general, thus expressing it as

$$\mathbf{h} = h_0\Big(\cos(\phi)\sin(\theta)\hat{\mathbf{x}} + \sin(\phi)\sin(\theta)\hat{\mathbf{z}} + \cos(\theta)\hat{\mathbf{y}}\Big), \tag{5.4}$$

where ϕ is the azimuthal angle and θ is the polar angle of slightly modified spherical coordinates, that is with y and z having changed roles.[e] With the definitions in Table 3, the SOC Hamiltonian becomes

$$H_{\mathrm{SO}} = \alpha_{\mathrm{R}}\Big[k_x\sigma_z - k_z\sigma_x\Big] + \frac{\alpha_R\sigma_z}{2i}\Big[\delta(x - x_{\mathrm{L}}) - \delta(x - x_{\mathrm{R}})\Big], \tag{5.5}$$

where x_{L} and x_{R} are the x-coordinates of the left and right boundaries of the SOC-region respectively, and where the position dependence of the Rashba parameter has been suppressed in the notation.

5.3.1 Pair amplitudes

We start the analysis by plotting the pair amplitudes for different magnetization directions. Due to the spin-mixing effect of SOC at most magnetization setups, as encountered in the last chapter, we need to include all pair amplitudes, f_0, f_1, f_2 and f_3. Fig. 5.13 depicts the results for the singlet pair amplitude for magnetization along the x-, y- and z-axis. The Rashba parameter has been set to $\alpha_{\mathrm{R}}k_{\mathrm{F}}/E_{\mathrm{F}} = 0.4$ for this analysis.

[e] This choice was only made as it provides the simplest formalism.

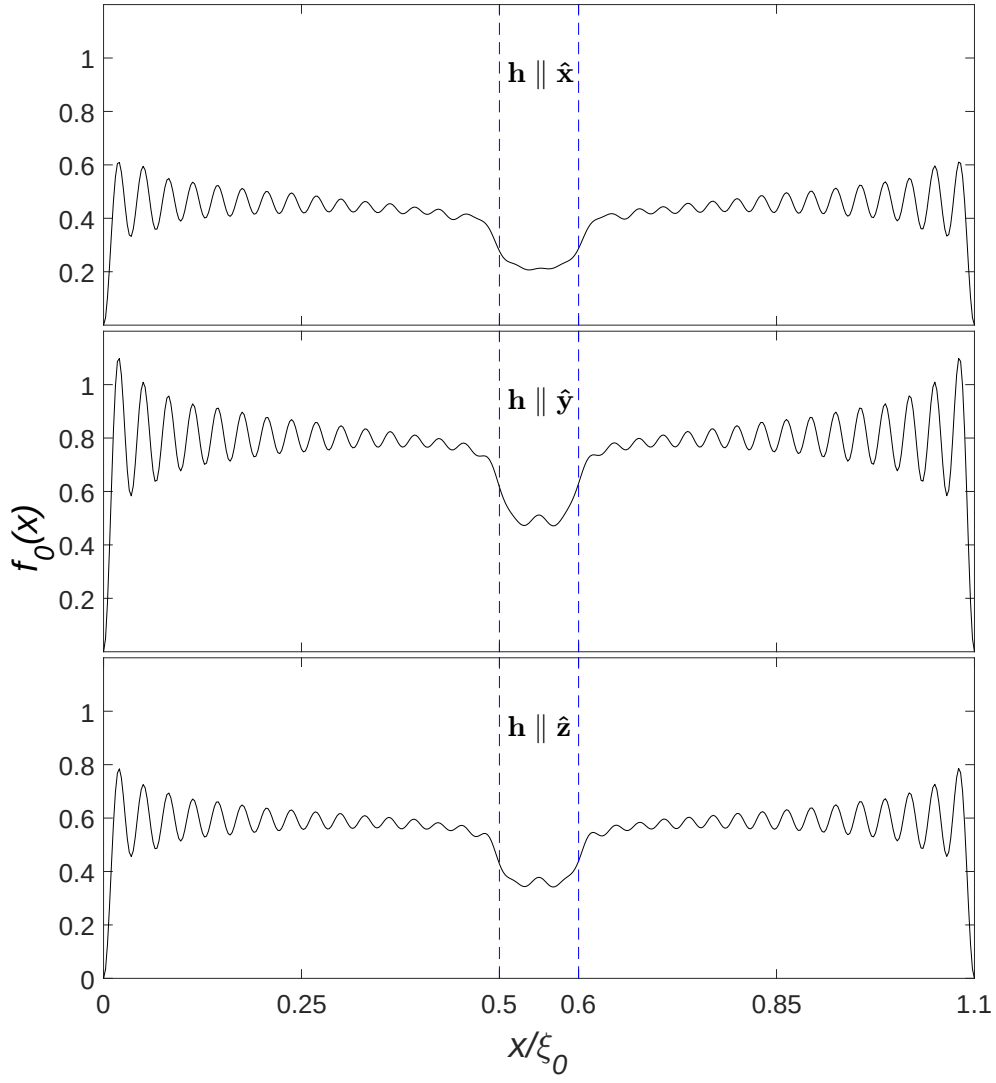

Figure 5.13: The singlet amplitude plotted for the S/F/S-structure with in-plane SOC in the F-region, for magnetization along the x-, y- and z-axis. The dotted blue lines indicate the junctions between the F- and S-regions. The Rashba parameter has been set to $\alpha_R k_F / E_F = 0.4$.

The qualitative behaviour for the singlet amplitudes of these magnetization setups are all approximately the same. The singlet amplitude stabilizes at some level inside the S-regions. The amplitudes then drop abruptly, about $0.025\xi_0$ from the junction, and stabilize at a lower level about $0.025\xi_0$ inside the F-region. This same behaviour applies for both F/S-junctions. However, none of the plots are symmetric about the center of the system. At first sight, they seem symmetric, and they are indeed *almost* symmetric. The symmetries are however not exact, and the amplitudes are in general a bit higher on the right side of the structures compared to the left side. It might seem weird that this seemingly symmetric system configuration produces non-symmetric results, which in general would not be allowed. However, considering SOC, parity invariance is broken already at the Hamiltonian level. More explicitly, since the Hamiltonian is

linear in $\mathbf{k}$, or equivalently in x, it will not be invariant under a mirror transformation $x \to -x$. A physical consequence of this parity-invariance is for instance the induced magnetic impurities, of which magnetic fields are oppositely aligned, showing clearly that the system is in fact not symmetric. If the electric field which causes the SOC is reversed, that is $\alpha_{\mathrm{R}} \to -\alpha_R$, the results become the mirror image of these results, about the center.

By comparing the different magnetization directions, a significant quantitative difference between them is evident. With the magnetic field aligned parallel to the y-axis, the singlet amplitude stabilizes at about 0.8 inside the S-regions. With the magnetic field parallel to either the x- or z-axis however, this level drops to about 0.45 and 0.6, respectively. This indicates that the superconducting state prefers the y-alignment of the magnetic field, and is most suppressed by an x-aligned field. However, if SOC was switched off, the singlet amplitudes would drop to zero no matter the magnetization direction, implying that SOC once again shows an enhancing effect on superconductivity. Furthermore, if SOC was switched off, the system would be spin-rotationally invariant, implying a singlet amplitude independent upon the magnetization angle. Hence, as in the last chapter with interfacial SOC, SOC introduces a prominent dependence upon the direction of the magnetic field.

The triplet amplitudes for the same magnetization setups are plotted in Fig. 5.14. Note that the axes are scaled differently, and the graphical amplitudes are thus not directly comparable between the different plots.

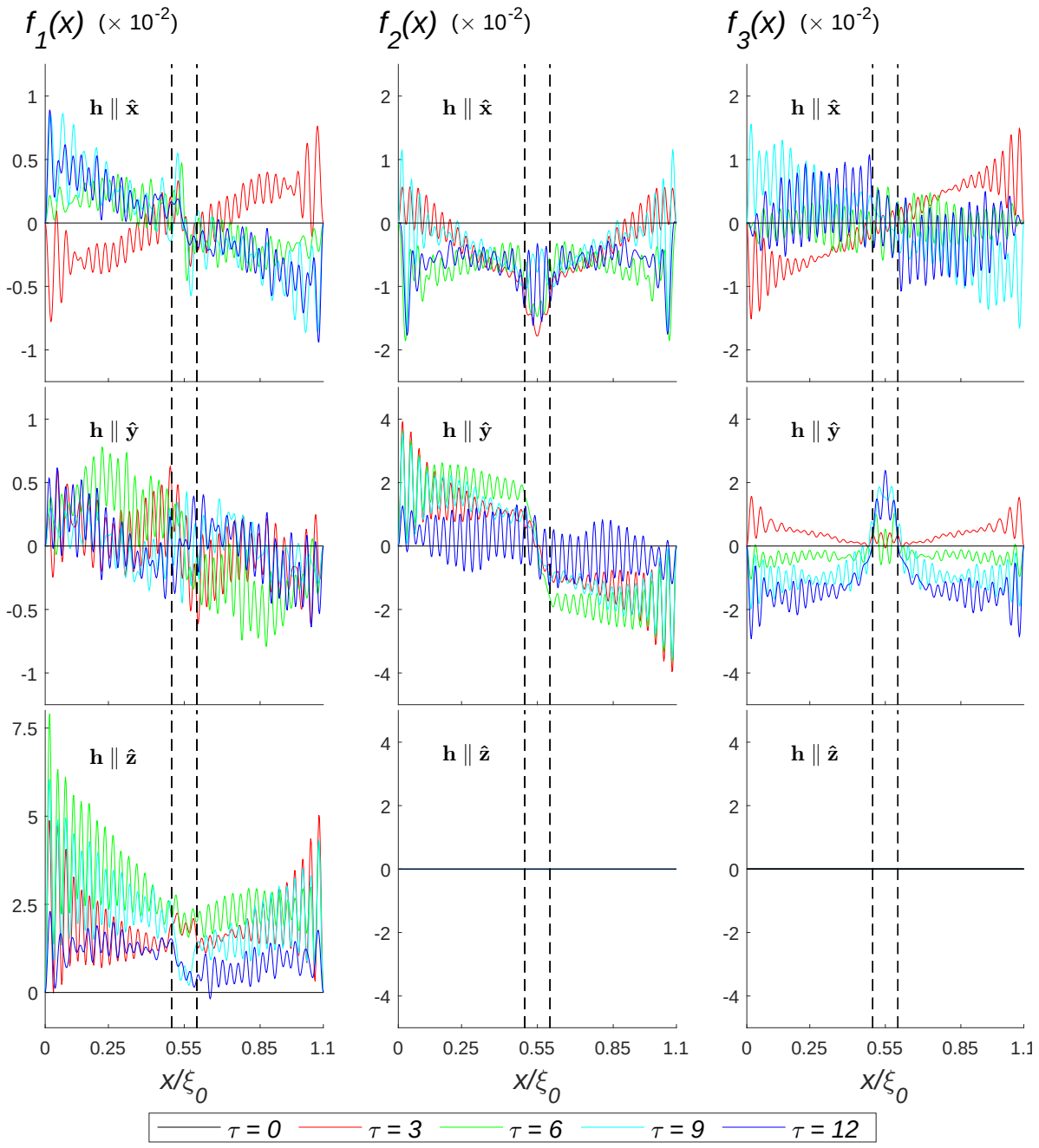

Figure 5.14: The triplet amplitudes for the S/F/S-structure with in-plane SOC in the F-region for magnetization along the x-, y- and z-axis. The results are plotted for five different relative time τ, as indicated by the legend. The black dotted lines indicate the junctions between the different regions. Note that the axes are scaled differently, and the graphical amplitudes are thus not directly comparable.

If SOC was switched off, the rotation of the magnetic field would only cause the triplet amplitudes to rotate between each other, as derived in Chapter 2.4.1. In this case, x-aligned magnetization would have given an f_2-amplitude, y-aligned magnetization would have given an f_3-amplitude, and z-aligned magnetization would have given an

f_1-amplitude. For each magnetization, all other than the mentioned triplet amplitude would have been identically zero. With SOC switched on however, all triplet amplitudes appear for the x- and y-aligned fields, while only the f_1-amplitude remains non-zero for the z-aligned field.

There are two reasons to the appearance of other triplet amplitudes. Firstly, as mentioned in the introduction of this chapter, SOC induces magnetic impurities in the junction between the S- and F-regions. These magnetic fields always point in the $\pm z$-direction. Thus, for magnetization in the x- and y-directions, the magnetization configuration is inhomogeneous. This induces an f_1-amplitude, explaining the appearance of this amplitude for these magnetization setups. For magnetization along the z-axis, all magnetic fields are either parallel or antiparallel, and only the f_1-amplitude appears. Secondly, SOC introduces spin-mixing at intermediate angles, that is when the magnetic field is not either orthogonal or parallel to the SOC-induced field. The x-aligned magnetic field does obviously not satisfy any of these exceptions, causing spin-mixing to occur, resulting in a non-zero f_3-amplitude. For the y-aligned field, the magnetic field intrinsic in the F-region is orthogonal to the SOC-induced fields, but the magnetic impurities are not, causing an f_2-amplitude to appear. However, for the z-aligned field, in which situation spin-mixing should occur, the ($s_z = \pm 1$)-amplitudes are both zero. This is not obvious from the Hamiltonian level, as $[H, \sigma_z] \neq 0$. However, the results show that both the f_2- and f_3-amplitudes are exactly zero, indicating that some symmetry cancels the spin-mixing contributions. The exact reason for this cancellation needs however a more detailed analysis.

5.3.2 LDOS

As magnetization in either the x-, y- or z-directions clearly give different pair amplitudes, both for the singlet- and triplet-amplitudes, it makes an interesting analysis to take a closer look at the configuration of states around the Fermi energy for each case. The LDOS at four different positions have therefore been plotted in Fig. 5.15. The upper two plots show the density of states at two different positions inside the left S-region, while the two lower plots do the same for inside the F-region.

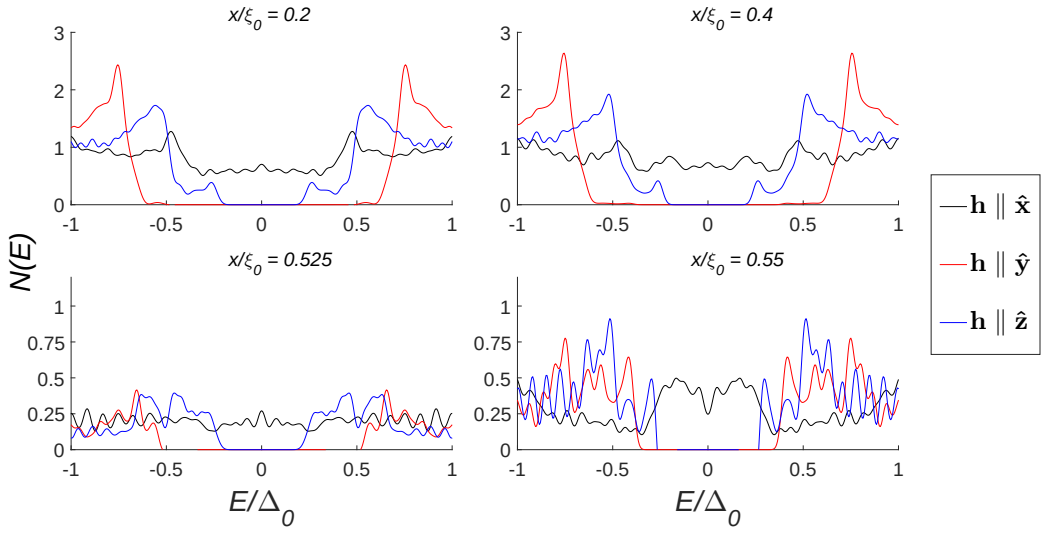

Figure 5.15: The LDOS at four different positions inside the S/F/S-structure with in-plane SOC in the F-region. The positions are indicated in the plots, and the colour coding is indicated by the legend. The results are obtained with $N_\perp = 2000$.

Inside the S-region, there is a fully developed energy gap for magnetization in the y- and z-directions, with $\mathbf{h} \parallel \hat{\mathbf{y}}$ giving the largest gap. The gap is much less developed for the x-aligned magnetic field. Inside the F-region, the amplitudes are being suppressed for all system setups, with an average at about 0.25 outside the band gap region. This is both an effect of the magnetic field, which suppresses certain spin-configurations, as well as due to SOC suppressing states dependent upon both their momentum and spin. The remarkably strong oscillations for $x/\xi_0 = 0.55$ are probably not to be interpreted as physical results, but rather as a result of the discretization of energy levels. What is a physical effect however, is that the band gap is in fact fully developed at both positions inside the F-region for both the y- and z-aligned fields. Once again, the gap is widest for the y-aligned field. These results are consistent to the results obtained for the singlet amplitudes. In general, the band gap seems to be wider and more prominent for $\mathbf{h} \parallel \hat{\mathbf{y}}$, and weakens for $\mathbf{h} \parallel \hat{\mathbf{z}}$ and $\mathbf{h} \parallel \hat{\mathbf{x}}$, in that order.

5.3.3 Critical temperature and the Rashba parameter

The analysis in the previous section was done for a Rashba parameter of $\alpha_R k_F / E_F = 0.4$. We follow up this analysis by investigating how varying the Rashba parameter affects the physics of the system. This analysis is once again performed for the magnetic field pointing in both the x-, y- and z-directions. The results are plotted in Fig. 5.16.

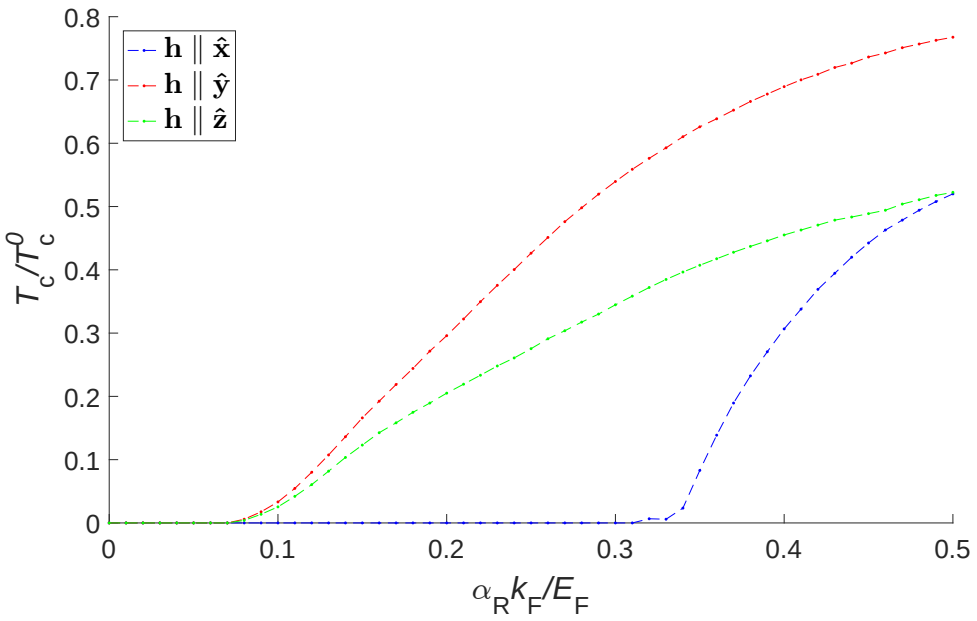

Figure 5.16: The critical temperature plotted with respect to the Rashba parameter for the S/F/S-structure with in-plane SOC in the F-region. The magnetic field strength is set to $h_0/E_F = 0.1$. Each line represents a magnetic field orientation along an axis, orthogonal to the others, as indicated by the legend.

The critical temperature increases with increasing α_R for all magnetic field configurations, (ϕ, θ). The degree to which the temperature rises differ between all configurations, as we should expect after the analysis in the previous section. The critical temperature is generally higher for a magnetic field pointing in the y-direction. For magnetic field configurations in the xz-plane, that is in the plane which is spanned by the physical system, the critical temperature is different for small Rashba parameters. The critical temperature is in general higher when the magnetic field is pointing in the z-direction, but this difference reduces as $\alpha_R k_F$ approaches $0.5E_F$. These results are consistent with what observed for the singlet amplitude and for the LDOS. However, this analysis also brings some new and interesting observations, which can help us understand the physics better.

We will now try to come to an explanation for all these phenomena. We start by looking into the easily visible difference between magnetization along the y-direction, and magnetization in the xz-plane. It is obvious from Fig. 5.16 that superconductivity is most resistant to thermal effects with a magnetic field along the y-axis. This result is rather straightforward to understand, and we will use the observations in the Chapter 5.2 to help us explain this. Firstly, we learned that an increasing Rashba-parameter in general causes an increased critical temperature, as illustrated by for instance Fig. 5.10. Secondly, the superconductivity-enhancing effect caused by SOC was observed to be most prominent at $\theta_h = \pi/2$. For the S/F/S-system considered here, the SOC-induced magnetic fields are always parallel to the xz-plane, perpendicular to the y-axis. Thus, for magnetization in the y-direction, the requirement for maximal effect of SOC

is always satisfied. Furthermore, the SOC-induced fields in the x- and z-directions can be added together, and the effect will thus in general be stronger than observed in the last chapter for the same Rashba parameter. This is more or less equivalent to defining a net larger Rashba parameter, which will also cause the effect of SOC to increase. Both of these effects are maximal when $\theta = 0$, and this is what causes the critical temperature to be maximal for this magnetic field configuration.

The difference between the x- and z-aligned magnetic fields is a bit more intricate to explain. If the effective magnetic impurities at the boundaries of the SOC-region were not present in the Hamiltonian, the Hamiltonian would have remained spin-rotationally invariant in the ϕ-coordinate. This would forbid any ϕ-dependence of the critical temperature. Hence, this ϕ-dependence must be due to these effective magnetic impurities. As given by the Hamiltonian in Eq. (5.5), the two magnetic impurities are oppositely aligned. Furthermore, the magnetic fields in the impurities are always aligned with the z-axis. Hence, the magnetic field configuration of the system is not invariant under a change of (ϕ, θ). From the F/F/S-structure in Chapter 4.5, it was clear that a perpendicular relative orientation of neighbouring magnetic field regions caused the lowest critical temperature. This was due to the long-range triplet production, which effectively caused another channel of triplet leakage to occur. We can use this result to explain the ϕ-dependence of T_c. When $\phi = \pi/2$, all magnetic fields in the system are either parallel or antiparallel. Hence, in this configuration, only the short-range triplet channel is open, as is showed explicitly by Fig. 5.14. When ϕ is decreased however, the production of long-range triplet pairs is increased. This effect reaches its maximum at $\phi = 0$, and is symmetric about this angle. Another channel of leakage is thus opened by the magnetic field configuration when $0 \leq \phi < \pi/2$, which implies lower critical temperature for an x-aligned magnetic field than for a z-aligned field.

When the Rashba parameter becomes large, that is when $\alpha_R k_F / E_F \approx 0.5$, it is evident that the critical temperature is almost the same for an x- and z-aligned magnetic field. We can understand this from the fact that the source of long-range triplet pairs are short-ranged triplet pairs, which are being "rotated" into long-ranged ones. However, when the effect of SOC is sufficiently strong, the amount of short-ranged triplet pairs in the system is low. This further implies that the production of long-ranged triplet pairs must be reduced. When $\alpha_R k_F / E_F \approx 0.5$, the difference in T_c between the two magnetic field directions is of order $0.01 T_c^0$, and roughly defines the point where the T_c-reducing effect of the long-ranged triplets becomes negligible.

Having used the induced magnetic impurities to explain the difference between the x- and z-directions, this raises another question. When $\mathbf{h} \parallel \hat{\mathbf{y}}$, the magnetic field configuration is such that the requirement for maximal long-ranged triplet production is fulfilled. We must therefore try to explain why the critical temperature is not more suppressed for this case, especially for small α_R. That is, why T_c is always higher for $\mathbf{h} \parallel \hat{\mathbf{y}}$ than for $\mathbf{h} \parallel \hat{\mathbf{z}}$, in which case in fact no long-ranged triplets are produced. There is one argument implying high T_c, namely that the magnetic field is always perpendicular to the SOC-induced field. Another argument implies low T_c, namely the triplet production caused by the magnetic impurities. These are two competing forces, of which magnitudes are not easy to assess analytically. Although not being

able to predict the exact behaviour of the graphs, the results are no less interesting. For small Rashba-parameters, it seems as though the response of a y-aligned magnetic field is equal to that of a z-aligned field. For large Rashba parameters, the y-aligned magnetic field clearly gives the highest T_c, while the magnetization in the xz-plane almost becomes ϕ-invariant.

5.3.4 Critical temperature and the magnetization angles

We have already made a thorough analysis on the critical temperature at the extrema of the magnetization angles, that is with magnetization along either the x-, y- or z-axis. To make the analysis complete, and in order to reveal the exact angular dependence, the critical temperature as function of the magnetization angles (ϕ, θ) is plotted in Fig. 5.17. The plot contains three graphs, each of which corresponds to rotation in either the xy-, yz- or zx-plane. The Rashba parameter has been set to $\alpha_R k_F / E_F = 0.4$ for this analysis.

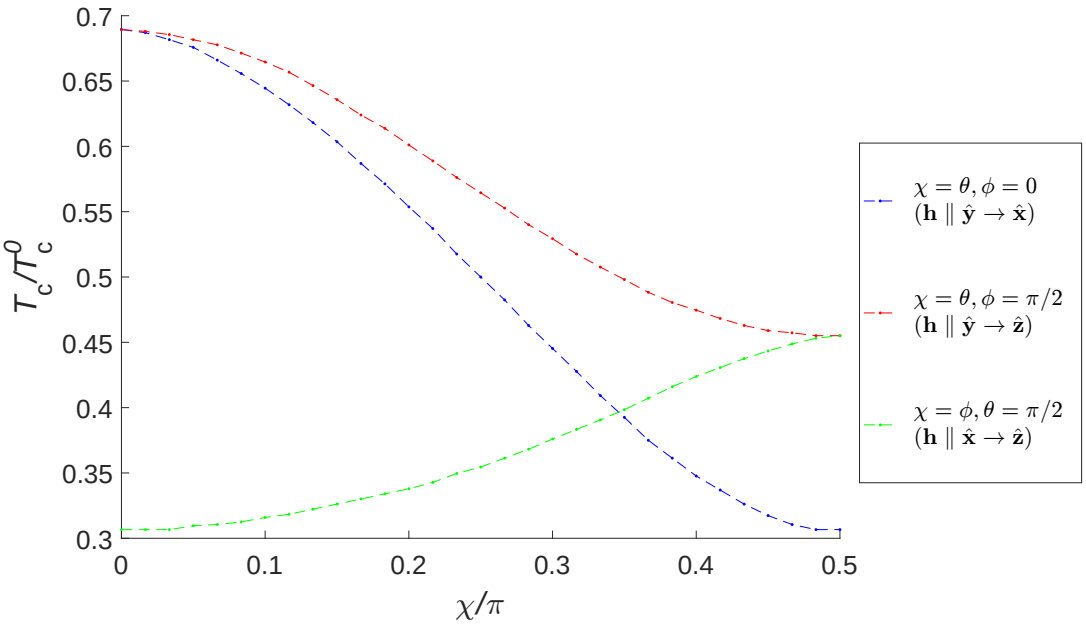

Figure 5.17: The critical temperature plotted with respect to different magnetization angles, with $\alpha_R k_F / E_F = 0.4$. θ and ϕ have been rotated between 0 and $\pi/2$ in the xy-plane (blue), zy-plane (red) and zx-plane (green). The angle χ represents either ϕ or θ, and is specified by the legend for each individual line.

The results are consistent with the analysis made in the discussion of magnetization in the x-, y- or z-direction, and we will therefore not go through the whole analysis of this once more. However, we observe that the graphs are all strictly increasing or decreasing, and contain thus no local minima or maxima. The transition between the different extrema, namely magnetization along the coordinate axes, happens smoothly.

There are no intermediate angles at which effects other than those discussed up until now occur.

The figure above shows that the largest change in T_c by rotating the magnetic field happens for rotation in the xy-plane. The difference between $\theta = 0$ and $\theta = \pi/2$ is almost $0.4T_c^0$. This structure thus has a great potential in controlling T_c by adjusting both the SOC-strength and the magnetization angles. It also serves a candidate for controlling the triplet production, as magnetization along the x-, y- and z-axis all give different properties for the triplet amplitudes. Additionally, these effects are obtainable for a structure of only $1.1\xi_0$, which is generally shorter than required for clean ferromagnet-superconductor-structures.

6 Summary and outlooks

In this thesis, we have explored the effects of spin-orbit coupling in two-dimensional structures comprised of superconductors, normal metals and ferromagnets. Results for various structures without the presence of spin-orbit coupling have also been produced, and these have served as reference to the results obtained with the inclusion of spin-orbit coupling.

We have demonstrated that interfacial spin-orbit coupling in an N/S-structure affects superconductivity in a similar manner as non-magnetic impurities, effectively decoupling regions in the structure. When switching on a homogeneous magnetic field inside the metallic region however, superconductivity gain dependency upon the magnetization angle relative to the orientation of the spin-orbit coupling region. The results showed that aligning the magnetic field perpendicular to the effective magnetic fields induced by spin-orbit interaction was favoured by the superconducting state, resulting in a significantly higher critical temperature as compared to a parallel alignment. This effect was also easily visible in the density of states, where higher magnetization angles were shown to give a much more prominent superconducting energy gap.

A setup where in-plane spin-orbit coupling was present in the ferromagnetic region of an S/F/S-structure was also explored. The results were quite similar to the ones obtained from interfacial spin-orbit coupling, but the effect was even stronger in this case. The superconducting order in this structure was dependent upon both angles determining the direction of the magnetic field, showing thus in general different behaviour for all magnetization directions inside a hemisphere. With this structure, both the singlet and triplet amplitudes, as well as the critical temperature, can be thoroughly controlled by adjusting the magnetization direction and the strength of the spin-orbit interaction. However, spin-orbit interaction always seem to increase the critical temperature, no matter the parameter configuration.

These results have been partly explained by analytically finding the eigenstates of systems including both magnetic fields and spin-orbit coupling, that is pseudospin states. By expressing the singlet amplitude in terms of these states, it became evident that the singlet state projected onto the eigenbasis has a non-zero long-ranged pseudotriplet component. This long-ranged component allows some of the singlets to proceed through the ferromagnetic region without being ripped apart, effectively enhancing superconductivity. A qualitative analysis also predicted spin-mixing between triplets to occur at most magnetization configurations, as was confirmed by explicit calculations in both structures.

In summary, the inclusion of spin-orbit coupling in F/S-structures allows for both the critical temperature and pair amplitudes to be controlled by macroscopic parame-

ters such as Rashba coupling strength and magnetization angle. These structures may thus serve as alternatives to inhomogeneously magnetized structures of which purpose is such control. An obvious advantage of these structures is that spin-orbit coupling in general enhances superconductivity, in great contrast to the effect of ferromagnets. This opens up the possibility of making the structures smaller, or alternatively operating at higher temperatures.

This thesis has shown qualitatively what effects may be obtained by two different configurations of spin-orbit coupling in combination with superconductors and ferromagnets. The results show that these structures have interesting properties which might be useful in future technological applications. There are still many possible configurations that are yet unexplored, and hopefully this thesis provides sufficient motivation for such structures to be object to thorough analyses in the future.

Bibliography

[1] G. Miao. *Superconductors - New Developments*. InTech, 2015.

[2] M. Eschrig. Spin-polarized supercurrents for spintronics. *Physics Today*, 64(1):43–49, 2011.

[3] Y. V. Fominov, A. F. Volkov, and K. B. Efetov. Josephson effect due to the long-range odd-frequency triplet superconductivity in SFS junctions with Néel domain walls. *Physical Review B*, 75(10), 2007.

[4] J. Linder and K. Halterman. Superconducting spintronics with magnetic domain walls. *Physical Review B*, 90(10), 2014.

[5] F. S. Bergeret, A. F. Volkov, and K. B. Efetov. Odd triplet superconductivity in superconductor-ferromagnet hybrid structures. *Comptes Rendus Physique*, 7(1):128–135, 2006.

[6] M. Houzet and A. I. Buzdin. Long range triplet Josephson effect through a ferromagnetic trilayer. *Physical Review B*, 76(6), 2007.

[7] J. Linder and J. W. A. Robinson. Superconducting spintronics. *Nature Physics*, 11(4):307–315, 2015.

[8] F. S. Bergeret and I. V. Tokatly. Singlet-triplet conversion and the long-range proximity effect in superconductor-ferromagnet structures with generic spin dependent fields. *Physical Review Letters*, 110(11), 2013.

[9] I. Zutic, J. Fabian, and S. D. Sarma. Spintronics: Fundamentals and applications. *Reviews of Modern Physics*, 76(2):323–410, 2004.

[10] N. Banerjee, C. B. Smiet, R. G. J. Smits, A. Ozaeta, F. S. Bergeret, M. G. Blamire, and J. W. A. Robinson. Evidence for spin selectivity of triplet pairs in superconducting spin valves. *Nature Communications*, 5(3048):1–6, 2014.

[11] P. V. Leksin, N. N. Garif'Yanov, I. A. Garifullin, Ya V. Fominov, J. Schumann, Y. Krupskaya, V. Kataev, O. G. Schmidt, and B. Büchner. Evidence for triplet superconductivity in a superconductor-ferromagnet spin valve. *Physical Review Letters*, 109(5), 2012.

[12] F. S. Bergeret, A. F. Volkov, and K. B. Efetov. Long-range proximity effects in superconductor-ferromagnet structures. *Physical Review Letters*, 86(18):4096–4099, 2001.

[13] R. S. Keizer, S. T. B. Goennenwein, T. M. Klapwijk, G. Miao, G. Xiao, and A. Gupta. A spin triplet supercurrent through the half-metallic ferromagnet CrO2. *Nature*, 439(7078):825–827, 2006.

[14] F. S. Bergeret and I. V. Tokatly. Spin-orbit coupling as a source of long-range triplet proximity effect in superconductor-ferromagnet hybrid structures. *Physical Review B*, 89(13), 2014.

[15] F. Setiawan, W. S. Cole, J. D. Sau, and S. D. Sarma. Transport in superconductor–normal metal–superconductor tunneling structures: spinful p-wave and spin-orbit-coupled topological wires. *Physical Review B*, 95(17), 2017.

[16] S. Tewari, T. D. Stanescu, J.D. Sau, and S. D. Sarma. Topologically non-trivial superconductivity in spin-orbit-coupled systems: Bulk phases and quantum phase transitions. *New Journal of Physics*, 13, 2011.

[17] M. Sato and Y. Ando. Topological superconductors: a review. *Rep. Prog. Phys.*, 80(07), 2017.

[18] V. Mourik, K. Zuo, S. M. Frolov, S. R. Plissard, E. P. A. M. Bakkers, and L. P. Kouwenhoven. Signatures of Majorana Fermions in. *Science*, 336(6084):1003–1007, 2012.

[19] M. Leijnse and K. Flensberg. Introduction to topological superconductivity and Majorana fermions. *Semicond. Sci. Technol.*, 27(12), 2012.

[20] S. Nadj-Perge, I. K. Drozdov, B. A. Bernevig, and A. Yazdani. Proposal for realizing Majorana fermions in chains of magnetic atoms on a superconductor. *Physical Review B*, 88(2), 2013.

[21] S. Nadj-Perge, I. K. Drozdov, J. Li, H. Chen, S. Jeon, J. Seo, A. H. MacDonald, B. A. Bernevig, and A. Yazdani. Observation of Majorana fermions in ferromagnetic atomic chains on a superconductor. *Science*, 346(6209):602–607, 2014.

[22] J. Bardeen, L. N. Cooper, and J. R. Schrieffer. Theory of superconductivity. *Physical Review*, 108(5):1175–1204, 1957.

[23] N. B. Kopnin. *Theory of Superconductivity*. Lecture notes, Helsinki University of Technology, 2006.

[24] K. Fossheim and A. Sudbø. *Superconductivity Physics and Applications*. John Wiley & Sons Ltd., 2004.

[25] M.-w. Xiao. Theory of transformation for the diagonalization of quadratic Hamiltonians. 2009.

[26] B. J. Powell. *On the Interplay of Superconductivity and Magnetism*. PhD thesis, University of Bristol, 2002.

[27] J. O. Fjærestad. *Second quantization (the occupation-number representation)*. Lecture notes, Norwegian University of Science and Technology, 2013.

[28] K. Ishida, H. Mukuda, Y. Kitaoka, K. Asayama, Z. Q. Mao, Y. Mori, and Y. Maeno. Spin-triplet superconductivity in Sr2RuO4 identified by 17O Knight Shift. *Nature*, 396(6712):658–660, 1998.

[29] A. P. Mackenzie and Y. Maeno. The superconductivity of Sr2RuO4 and the physics of spin-triplet pairing. *Reviews of Modern Physics*, 75(2):657–712, 2003.

[30] Y. Maeno, S. Kittaka, T. Nomura, S. Yonezawa, and K. Ishida. Evaluation of spin-triplet superconductivity in Sr2RuO4. *Journal of the Physical Society of Japan*, 81(1), 2012.

[31] M. S. Anwar, S. R. Lee, R. Ishiguro, Y. Sugimoto, Y. Tano, S. J. Kang, Y. J. Shin, S. Yonezawa, D. Manske, H. Takayanagi, T. W. Noh, and Y. Maeno. Direct penetration of spin-triplet superconductivity into a ferromagnet in Au/SrRuO3/Sr2RuO4 junctions. *Nature Communications*, 7:13220, 2016.

[32] F. S. Bergeret, A. F. Volkov, and K. B. Efetov. Odd triplet superconductivity and related phenomena in superconductor-ferromagnet structures. *Reviews of Modern Physics*, 77(4):1321–1373, 2005.

[33] K. Halterman, O. T. Valls, and C.-T. Wu. Charge and spin currents in ferromagnetic Josephson junctions. *Physical Review B*, 92(17), 2015.

[34] O. Krupin. *Dichroism and Rashba effect at magnetic crystal surfaces of rare-earth metals*. PhD thesis, Freie Universität Berlin, 2014.

[35] A. Manchon and S. Zhang. Theory of spin torque due to spin-orbit coupling. *Physical Review B*, 79(9):094422, 2009.

[36] Y. A. Bychkov and E. I. Rashba. Oscillatory effects and the magnetic susceptibility of carriers in inversion layers. *Journal of Physics C: Solid State Physics*, 17(33):6039–6045, 1984.

[37] M. Heide and G. Bihlmayer. Spin–orbit Driven Physics at Surfaces. *Newsletter of the Psi-K Community*, 2006.

[38] S. E. Barnes, J. Ieda, and S. Maekawa. Rashba Spin-Orbit Anisotropy and the Electric Field Control of Magnetism. *Scientific Reports*, 4(1):4105, 2015.

[39] A. Manchon, H. C. Koo, J. Nitta, S. M. Frolov, and R. A. Duine. New perspectives for Rashba spin–orbit coupling. *Nature Materials*, 14(9):871–882, 2015.

[40] K. V. Samokhin. Symmetry and topology of noncentrosymmetric superconductors. *Annals of Physics*, 359:385–404, 2015.

[41] S. V. Borisenko, D. V. Evtushinsky, Z.-H. Liu, I. Morozov, R. Kappenberger, S. Wurmehl, B. Buchner, A. N. Yaresko, T. K. Kim, M. Hoesch, T. Wolf, and N. D. Zhigadlo. Direct observation of spin-orbit coupling in iron-based superconductors. *Nature Physics*, 12(4):311–318, 2015.

[42] K. Halterman and O. T. Valls. Proximity effects and characteristic lengths in ferromagnet-superconductor structures. *Physical Review B*, 66(22), 2002.

[43] K. Halterman, O. T. Valls, and M. Alidoust. Characteristic energies, transition temperatures, and switching effects in clean S|N|S graphene nanostructures. *Physical Review B*, 84(6), 2011.

[44] K. Halterman and O. T. Valls. Proximity effects at ferromagnet-superconductor interfaces. *Physical Review B*, 65(1), 2001.

[45] P. H. Barsic, O. T. Valls, and K. Halterman. Thermodynamics and phase diagrams of layered superconductor/ferromagnet nanostructures. *Physical Review B*, 75(10), 2007.

[46] B. H. Bransden and C. J. Joachain. *Quantum Mechanics*. Pearson Education Ltd., 2nd edition, 2000.

[47] K. Halterman, P. H. Barsic, and O. T. Valls. Odd triplet pairing in clean superconductor/ferromagnet heterostructures. *Physical Review Letters*, 99(12), 2007.

[48] K. Halterman and O. T. Valls. Stability of pi-junction configurations in ferromagnet-superconductor heterostructures. *Physical Review B*, 70(10), 2004.

[49] I. Kosztin, S. Kos, M. Stone, and A. J. Leggett. Free energy of an inhomogeneous superconductor : A wave-function approach. *Physical Review B*, 58(14):9365–9384, 1998.

[50] P. G. de Gennes. Boundary Effects in Superconductors. *Reviews of Modern Physics*, 36(1):225–237, 1964.

[51] P. C. Hemmer. *Kvantemekanikk*. Tapir Akademisk Forlag, 5th edition, 2005.

[52] H. Bruus and K. Flensberg. *Many-Body Quantum Theory in Condensed Matter Physics - An Introduction*. Oxford University Press, 2004.

[53] A. I. Buzdin. Proximity effects in superconductor-ferromagnet heterostructures. *Reviews of Modern Physics*, 77(3):935–976, 2005.

[54] D. Ivanov, R. von Roten, and G. Blatter. Minigap in a long disordered SNS junction: Analytical results. *Physical Review B*, 66(05), 2002.

[55] D. A. Ivanov and Y. V. Fominov. Minigap in superconductor-ferromagnet junctions with inhomogeneous magnetization. *Physical Review B*, 73(21), 2006.

[56] Y. Nagato, K. Nagai, and J. Hara. Theory of the Andreev reflection and the density of states in proximity contact normal-superconducting infinite double-layer. *Journal of Low Temperature Physics*, 93(1-2):33–56, 1993.

[57] E. Blonder, M. Tinkham, and T. M. K. Lapwijk. Transition from metallic to tunneling regimes in superconducting microconstrictions: Excess current, charge imbalance, and supercurrent conversion. *Physical Review B*, 25(7), 1981.

[58] J. A. Ouassou, A. Pal, M. Blamire, M. Eschrig, and J. Linder. Triplet Cooper pairs induced in diffusive s-wave superconductors interfaced with strongly spin-polarized magnetic insulators or half-metallic ferromagnets. *Scientific Reports*, 7(May 2017), 2016.

[59] R. Fazio and C. Lucheroni. Local density of states in superconductor-ferromagnetic hybrid systems. *EPL (Europhysics Letters)*, 45(6):707, 1999.

[60] K. Halterman, O. T. Valls, and P. H. Barsic. Induced triplet pairing in clean s - wave superconductor/ferromagnet layered structures. *Physical Review B*, 77(17), 2008.

[61] C.-T. Wu, O. T. Valls, and K. Halterman. Proximity effects and triplet correlations in Ferromagnet/Ferromagnet/Superconductor nanostructures. *Physical Review B*, 86(01), 2012.

[62] A. I. Buzdin and A. V. Vedyayev. Spin-orientation-dependent superconductivity in F / S / F structures. *EPL (Europhysics Letters)*, 48(6):686–691, 1999.

[63] W. Zhang, W. Han, X. Jiang, S.H. Yang, and S. S. P. Parkin. Role of transparency of platinum–ferromagnet interfaces in determining the intrinsic magnitude of the spin Hall effect. *Nature Physics*, 11(6):496–502, 2015.

[64] T. E. Golikova, F. Hübler, D. Beckmann, I. E. Batov, T. Y. Karminskaya, M. Y. Kupriyanov, A. A. Golubov, and V. V. Ryazanov. Double proximity effect in hybrid planar superconductor-(normal metal/ferromagnet)-superconductor structures. *Physical Review B*, 86(6):1–10, 2012.

[65] Y. Zhu, A. Pal, M. G. Blamire, and Z. H. Barber. Superconducting exchange coupling between ferromagnets. *Nature Materials*, 16(2):195–199, 2016.

[66] D. Persson, O. Shevtsov, T. Löfwander, and M. Fogelström. Spectral properties of superconductors with ferromagnetically ordered magnetic impurities. *Physical Review B*, 92(24), 2015.

[67] R. Moradian and H. Mousavi. Validity of Anderson's theorem for s-wave superconductors. 2005.

[68] C. R. Reeg and D. L. Maslov. Proximity-induced triplet superconductivity in Rashba materials. *Physical Review B*, 92(13), 2015.

[69] I. V. Bobkova and A. M. Bobkov. Quasiclassical theory of magnetoelectric effects in superconducting heterostructures in the presence of the spin-orbit coupling. *Physical Review B*, 95(18), 2016.

[70] T. S. Khaire, W. P. Pratt, and N. O. Birge. Critical current behavior in Josephson junctions with the weak ferromagnet PdNi. *Physical Review B*, 79(9), 2009.

[71] V. V. Ryazanov, V. A. Oboznov, A. Y. Rusanov, A. V. Veretennikov, A. A. Golubov, and J. Aarts. Coupling of two superconductors through a ferromagnet: Evidence for a π junction. *Physical Review Letters*, 86(11):2427–2430, 2001.

[72] J. Xia, V. Shelukhin, M. Karpovski, A. Kapitulnik, and A. Palevski. Inverse proximity effect in superconductor-ferromagnet bilayer structures. *Physical Review Letters*, 102(8), 2009.

[73] S. H. Jacobsen, J. A. Ouassou, and J. Linder. Critical temperature and tunneling spectroscopy of superconductor-ferromagnet hybrids with intrinsic Rashba-Dresselhaus spin-orbit coupling. *Physical Review B*, 92(2), 2015.

[74] J. B. Miller, D. M. Zumbühl, C. M. Marcus, Y. B. Lyanda-Geller, D. Goldhaber-Gordon, K. Campman, and A. C. Gossard. Gate-Controlled Spin-Orbit Quantum Interference Effects in Lateral Transport. *Physical Review Letters*, 90(07), 2003.

[75] J Kanski, L Ilver, K Karlsson, I Ulfat, M Leandersson, J Sadowski, and I Di Marco. Electronic structure of (Ga,Mn)As revisited. *New Journal of Physics*, 19(02), 2017.

[76] Z. Wang, C. Tang, R. Sachs, Y. Barlas, and J. Shi. Proximity-induced ferromagnetism in graphene revealed by the anomalous hall effect. *Physical Review Letters*, 114(1), 2015.